Alma Mater Studiorum – Università di Bologna

DOTTORATO DI RICERCA IN

INGEGNERIA ENERGETICA, NUCLEARE E DEL CONTROLLO AMBIENTALE

Ciclo XVIII

Settore Concorsuale di afferenza: 09/C2

Settore Scientifico disciplinare: ING-IND/18

FUNDAMENTAL AND APPLIED ASPECTS OF X-RAY SPECTROMETRY: DETECTOR INFLUENCE AND PHOTOELECTRIC EFFECT CROSS-SECTIONS

Presentata da: **Lorenzo Sabbatucci**

Coordinatore Dottorato **Relatore**

Prof. Vincenzo Parenti Castelli **Prof. Jorge Eduardo Fernandez**

Correlatore

Prof. Francesc Salvat

Esame finale anno 2016

Contents

1 Theory and calculation of the atomic photoeffect 1

- 1.1 Theory . . . 3
  - 1.1.1 The Dirac Equation for an electron in a central potential field . . 3
  - 1.1.2 Matrix elements of Racah tensors and the spin operator 7
  - 1.1.3 The DHFS potential . . . 9
  - 1.1.4 Photon polarization . . . 10
  - 1.1.5 Derivation of the cross sections . . . 13
  - 1.1.6 One-electron transition-matrix elements . . . 18
  - 1.1.7 Cross sections of closed subshells . . . 21
  - 1.1.8 The dipole approximation . . . 23
  - 1.1.9 Near-edge excitation cross section . . . 24
  - 1.1.10 Ionization cross sections at high energies . . . 26
  - 1.1.11 Finite level widths and experimental ionization energies 28
  - 1.1.12 Normalization screening approximation . . . 30
- 1.2 Angular distribution of photoelectrons . . . 31
  - 1.2.1 Partially polarized photons . . . 36
- 1.3 Numerical calculation of cross sections . . . 38

2 Inverse problems in radiation spectrometry 45

- 2.1 Pulse pile-up . . . 48
  - 2.1.1 Peak PPU Balance equation . . . 52
  - 2.1.2 Pulse pile-up probability . . . 53
  - 2.1.3 PPU balance equation for rectangular pulses . . . 54
  - 2.1.4 Iterative method for solving order two PPU balance equation . . . 57

2.1.5 Si detector application 60
2.1.6 Monte Carlo method for pulse pile-up 60
2.1.7 The code MCPPU 64
2.1.8 Si application of MCPPU 66
2.2 Detector Response function 68
2.2.1 Theoretical model 69
2.2.2 The tool RESOLUTION 73
2.2.3 Examples of RESOLUTION applications with SSD 76
2.3 Detector unfolding 80
2.3.1 MAXED algoritm 82
2.3.2 UMESTRAT 83
2.3.3 Energy resolution improvement in radiation measurements 85
References 98

Preface

Radiation physics and engineering have reached a central importance role for several different areas of application. For example scattered radiation can be used for a non destructive analysis of materials composition and properties. Radiation emitted by a star can be measured for understanding its composition, cosmological events like the supernovae can be studied using their emitted radiation. Central importance of radiation physics and engineering can not be discarded also in biomedical applications like X-ray radiography and the treatment of cancer diseases.

A detailed description of the mechanism into which the radiation interacts with a media is of fundamental importance for properly understand a radiation measure. Moreover Radiation measures need to be corrected from the measuring system effects which can lead to a loss of information.

In this thesis it is reported the most important results collected during this PhD course in the field of radiation physics and engineering.

The thesis is organized in two chapters. The first one reports the work done during the Marco Polo project under the supervision of Prof. Francesc Salvat of the University of Barcelona. This chapter presents the theory and the calculation of the atomic photoeffect differential and total cross sections done for improving the already existing libraries.

The second chapter reports the work done under the supervision of Prof. J.E. Fernandez at the University of Bologna regarding the unfolding of radiation measurements from the measuring system effects.

Both the chapters begin with a detailed introduction of the specific topic and are organized in subsections. The results reported in this thesis were also published in the following papers:

1)"Theory and calculation of the atomic photoeffect" [1]

2)"First principles Pulse Pile-Up balance equation and fast deterministic solution" [2].

3)"Multi-shape pulse pile-up correction, the code MCPPU"[3],

4)"A modelling tool for energy resolution and incomplete charge collection" [4],

5)"Improvement of the detector resolution in X-ray spectrometry by using the maximum entropy method" [5],

Chapter 1

Theory and calculation of the atomic photoeffect

In the photoelectric effect, or photoeffect, a photon is absorbed by a target atom and, as a result, an atomic electron is emitted or promoted to a bound open orbital thus leaving the residual ion or atom in an excited state. The latter subsequently decays to its ground state through a cascade of radiative and non-radiative transitions with emission of characteristic x rays and Auger electrons. For photons with intermediate and low energies, the photoeffect dominates the transfer of energy from the photon field to charged particles. The so-called elementary theory of the process has been described by Pratt *et al.* [6] and by Scofield [7]. In their formulation the states of the atom are approximated by a model of independent electrons in a common central potential, and the interaction between the target atom and the electromagnetic field is treated as a perturbation to first order. This approach neglects electron correlations, *i.e.*, the collective character of the response of atomic electrons to the external field. Correlation effects have been studied by many authors using a variety of theoretical methods such as the random-phase approximation [8], many-body perturbation theory [9], R-matrix perturbation theory [10], and the time-dependent local-density approximation [11, 12, 13]. Calculations with these methods are quite involved, and numerical results have been published only for specific atoms and limited energy ranges.

Quantitative information on the photoeffect is required for practical applications (*e.g.*, x-ray fluorescence, x-ray photoelectron spectroscopy), as well as for Monte Carlo simulation of photon transport. Numerical tables of subshell cross sections (for ionization and for excitation to bound levels) and atomic cross sections are included in the Evaluated Photon Data Library (EPDL) [14]. The XCOM program [15] gives atomic cross sections for photoionization essentially equivalent to those in the EPDL. Both the EPDL and XCOM databases are based on calculations performed by Scofield [7] using the independent-electron model with the self-consistent Dirac-Hartree-Fock-Slater (DHFS) potential. They are considered to be the most reliable source of general information available to date; indeed, practically all modern Monte Carlo codes for photon transport utilize the EPDL. A systematic comparison of Scofield's cross sections with experimental data has been made by Saloman *et al.* [16]. It is worth mentioning that the theory, as well as the numerical tables calculated from it, apply to free atoms. Differences are to be expected for molecules and solids, particularly near absorption edges, partly because of aggregation effects on the atomic potential and also because of the EXAFS effect (extended x-ray absorption fine structure) [17].

Calculations based on approximate independent-electron models, such as the DHFS model, are affected by possible inaccuracies of the adopted central potential. A simple strategy to account for inaccuracies in the atomic potential is provided by the normalization screening approximation of Pratt and co-workers [18, 19, 20, 6]. According to this approximation, the subshell cross sections calculated from the DHFS potential and from a more elaborate atomic model (*e.g.*., the multi-configuration Dirac-Fock self-consistent model implemented in the program of Desclaux [21, 22]) differ essentially by a constant factor, which is equal to the ratio of electron densities near the nucleus. That is, in principle, one can improve the DHFS cross sections by multiplying them by an energy-independent factor, which is readily obtained from atomic-structure calculations that are more elaborate than the DHFS ones.

The angular distribution of photoelectrons is needed in x-ray photoelectron spectroscopy, using either x rays or synchrotron radiation [23, 24, 25], as well as in radiation transport calculations [26, 27]. Surprisingly, information on the angular distribution of photoelectrons, consistent with the subshell cross sections, is quite limited, or unavailable (see, *e.g.*, Ref. [28] and references therein). As a matter of fact, most Monte Carlo photon transport codes still rely on the Sauter formula [29], which gives the differential cross section for the ground state of hydrogenic ions obtained from the plane-wave Born approximation. The most elaborate tables of angular distributions available for all subshells of the elements are those given by Trzhaskovskaya *et al.* [30, 31, 28], which were calculated within the quadrupole approximation and parameterized using the formulas proposed by Cooper [32, 33]. These tables apply to unpolarised and linearly polarized photons and cover the energy range from 100 eV to 5 keV. Theoretical studies of angular distributions for soft-x-ray absorption by Derevianko *et al.* [34] and Amusia *et al.* [35] revealed the importance of higher-multipole corrections.

In the present chapter it will be described the elementary theory of the photoeffect in a concise but complete form, organized so as to allow systematic evaluations of cross sections for both ionization and excitation to bound levels. Following Scofield and others, it will be considered a model of independent electrons in the DHFS self-consistent potential. Although Scofield's numerical results are known to be fairly accurate, the size of his database is moderate and, in some energy ranges, the grid energies are too widely spaced to ensure that interpolation errors are less than the numerical accuracy of the tabulated data. Nowadays, instead of interpolating from a limited database, subshell ionization cross sections can be calculated interactively, even on modest personal computers, using numerical algorithms that are highly accurate. Thanks to the Marco Polo program, which allowed the author of this work to have an important collaboration with Prof. F. Salvat of the University of Barcelona, it was written a robust, flexible Fortran program, named PHOTACS [1]. PHOTACS calculates subshell cross sections for arbitrary atomic potentials. The calculations converge for excitation to levels with principal quantum number up to about 20 and for ionization by photons with energies up to about 2 MeV. Results from the program do confirm the accuracy of Scofield's data, but also reveal near-threshold features that are invisible in Scofield's database because of the large spacing of its energy grid. PHOTACS [1] includes tables of theoretical and empirical atomic level widths and allows the calculated subshell cross section (excitation plus ionization) to be transformed into a continuous function of the photon energy, through a convolution with a Lorentzian line profile. Once the photoemission cross section for a given photon energy is calculated, the angular distribution of photoelectrons can be obtained with little additional effort because radial integrals, which take most of the numerical work, were already computed to obtain the cross section. The code PHOTACS optionally calculates the angular distribution of photoelectrons emitted as a result of the absorption of partially polarized photons in a given subshell. Arbitrary photon polarization is described by means of the density matrix expressed in terms of the Stokes parameters.

The chapter is organized as follows. Section 1.1 presents an overview of the theory of the photoeffect. It is described a systematic extrapolation scheme to account for excitations to bound levels near the ionization threshold, as well as an analytical formula for extrapolating the photoionization cross section to arbitrarily high energies. Finally, the effect of the finite width of atomic energy levels and the normalization screening correction are considered. Photon polarization is described by means of the density matrix and the associated Stokes parameters. In Section 1.2 it is derived general formulas for the angular distribution of photoelectrons released by photons with arbitrary polarizations. The practical calculation of cross sections and photoelectron angular distributions is considered in Section 1.3, which contains a brief presentation of the program PHOTACS and results from several illustrative calculations.

1.1 Theory

1.1.1 The Dirac Equation for an electron in a central potential field

The one-electron Dirac Hamiltonian for a central potential $V(r)$ [36] can be expressed as:

$$\mathcal{H} = c\,\widetilde{\boldsymbol{\alpha}} \cdot \mathbf{p} + \widetilde{\beta}\mathrm{m_e}c^2 + V(r), \tag{1.1.1}$$

where c is the speed of light, m_e the mass of the electron, $\mathbf{p} = -\mathrm{i}\hbar\nabla$ the momentum operator, and $\widetilde{\boldsymbol{\alpha}}$, $\widetilde{\beta}$ are the Dirac 4×4 matrices in the spinor representation,

$$\widetilde{\boldsymbol{\alpha}} = \begin{pmatrix} 0 & \boldsymbol{\sigma} \\ \boldsymbol{\sigma} & 0 \end{pmatrix}, \qquad \widetilde{\beta} = \begin{pmatrix} I_2 & 0 \\ 0 & -I_2 \end{pmatrix}. \tag{1.1.2}$$

The 2×2 matrices $\boldsymbol{\sigma} = (\sigma_1, \sigma_2, \sigma_3)$ are the Pauli matrices,

$$\sigma_1 = \begin{pmatrix} 0 & 1 \\ 1 & 0 \end{pmatrix}, \qquad \sigma_2 = \begin{pmatrix} 0 & -\mathrm{i} \\ \mathrm{i} & 0 \end{pmatrix}, \qquad \sigma_3 = \begin{pmatrix} 1 & 0 \\ 0 & -1 \end{pmatrix}. \tag{1.1.3}$$

and I_2 is the identity matrix of rank two. The Dirac equation takes the form of:

$$\mathrm{i}\hbar \frac{\partial}{\partial t} \Psi(\mathbf{r}, t) = \mathcal{H} \Psi(\mathbf{r}, t), \tag{1.1.4}$$

were the solution $\Psi(\mathbf{r}, t)$ is the so called Dirac spinor, i.e. a wave function with four components:

$$\Psi(\mathbf{r}, t) = \begin{pmatrix} \Psi_1(\mathbf{r}, t) \\ \Psi_2(\mathbf{r}, t) \\ \Psi_3(\mathbf{r}, t) \\ \Psi_4(\mathbf{r}, t) \end{pmatrix}. \tag{1.1.5}$$

It is convenient to represent this vector as a bi-spinor:

$$\Psi(\mathbf{r}, t) \equiv \begin{pmatrix} \Psi_u(\mathbf{r}, t) \\ \Psi_l(\mathbf{r}, t) \end{pmatrix}, \tag{1.1.6}$$

which is a matrix of two lines and one row where the components are two spinors:

$$\Psi_u(\mathbf{r}, t) \equiv \begin{pmatrix} \Psi_1(\mathbf{r}, t) \\ \Psi_2(\mathbf{r}, t) \end{pmatrix}, \qquad \Psi_l(\mathbf{r}, t) \equiv \begin{pmatrix} \Psi_3(\mathbf{r}, t) \\ \Psi_4(\mathbf{r}, t) \end{pmatrix}, \tag{1.1.7}$$

called respectively the upper and lower component. In this representation the Dirac equation takes the form:

$$\mathrm{i}\hbar \frac{\partial}{\partial t} \begin{pmatrix} \Psi_u(\mathbf{r}, t) \\ \Psi_l(\mathbf{r}, t) \end{pmatrix} = \begin{pmatrix} \mathrm{m_e} c^2 & c\boldsymbol{\sigma} \cdot \mathbf{p} \\ c\boldsymbol{\sigma} \cdot \mathbf{p} & -\mathrm{m_e} c^2 \end{pmatrix} \begin{pmatrix} \Psi_u(\mathbf{r}, t) \\ \Psi_l(\mathbf{r}, t) \end{pmatrix} + V(r) \begin{pmatrix} \Psi_u(\mathbf{r}, t) \\ \Psi_l(\mathbf{r}, t) \end{pmatrix}. \tag{1.1.8}$$

Assuming the possibility to express the bi-spinor as $\Psi(\mathbf{r}, t) = \psi(\mathbf{r})\phi(t)$ (hypothesis of separation of variables)the solution of the Dirac equation takes the form:

$$\Psi(\mathbf{r}, t) = \psi(\mathbf{r}) \mathrm{exp} \left[-\frac{\mathrm{i}\,(\epsilon + \mathrm{m_e} c^2)\, t}{\hbar} \right] = \begin{pmatrix} \psi_u(\mathbf{r}) \\ \psi_l(\mathbf{r}) \end{pmatrix} \mathrm{exp} \left[-\frac{\mathrm{i}\,(\epsilon + \mathrm{m_e} c^2)\, t}{\hbar} \right], \tag{1.1.9}$$

where ϵ is the electron energy, exclusive of its rest energy. The time independent Dirac equation can be obtained by considering the eigenvalues problem of the Dirac Hamiltonian operator:

$$\mathcal{H} \psi(\mathbf{r}) = (\epsilon + m_e c^2) \psi(\mathbf{r}) \tag{1.1.10}$$

Using Eq. (1.1.1) we have:

$$\left[c\,\widetilde{\boldsymbol{\alpha}}\cdot\mathbf{p}+\left(\widetilde{\beta}-1\right)\mathrm{m_e}c^2+V(r)\right]\psi(\mathbf{r})=\epsilon\psi(\mathbf{r}), \tag{1.1.11}$$

The solution of this equation are the spherical orbitals relative to a particle in a central field, which are simultaneous eigenfunctions of the Dirac Hamiltonian and the total angular momentum operator $\mathbf{J}=\mathbf{L}+\mathbf{S}$, where $\mathbf{L}=-\mathrm{i}\mathbf{r}\times\nabla$ is the orbital angular momentum and $\mathbf{S}$ is the spin angular momentum (all angular momenta in units of $\hbar$). These eigenfunctions are the so-called spherical waves, and have the form [36, 37]

$$\psi_{\epsilon\kappa m}(\mathbf{r})=\frac{1}{r}\begin{pmatrix}P_{\epsilon\kappa}(r)\,\Omega_{\kappa,m}(\hat{\mathbf{r}})\\ \mathrm{i}Q_{\epsilon\kappa}(r)\,\Omega_{-\kappa,m}(\hat{\mathbf{r}})\end{pmatrix}, \tag{1.1.12}$$

where $\Omega_{\kappa,m}(\hat{\mathbf{r}})$ are spherical spinors, and $P_{\epsilon\kappa}(r)$ and $Q_{\epsilon\kappa}(r)$ are the large- and small-component radial functions, which satisfy the coupled differential equations

$$\begin{aligned}\frac{\mathrm{d}P_{\epsilon\kappa}}{\mathrm{d}r}&=-\frac{\kappa}{r}P_{\epsilon\kappa}+\frac{\epsilon-V+2\mathrm{m_e}c^2}{c\hbar}Q_{\epsilon\kappa}\,,\\ \frac{\mathrm{d}Q_{\epsilon\kappa}}{\mathrm{d}r}&=-\frac{\epsilon-V}{c\hbar}P_{\epsilon\kappa}+\frac{\kappa}{r}Q_{\epsilon\kappa}\,.\end{aligned} \tag{1.1.13}$$

The spherical spinors are eigenfunctions of the total angular momentum of Pauli's theory, *i.e.*, simultaneous eigenfunctions of the operators L^2, S_P^2, J_P^2 and $J_{\mathrm{P}z}$ with eigenvalues $\ell(\ell+1)$, $3/4$, $j(j+1)$ and m, respectively. Here $\mathbf{S}_\mathrm{P}=\frac{1}{2}\boldsymbol{\sigma}$ denotes the two-dimensional Pauli spin operator and $\mathbf{J}_\mathrm{P}=\mathbf{L}+\mathbf{S}_\mathrm{P}$. $\Omega_{\kappa,m}(\hat{\mathbf{r}})$ can be expressed as [38, 39]:

$$\Omega_{\kappa,m}(\hat{\mathbf{r}})\equiv\Omega^{\ell}_{j,m}(\hat{\mathbf{r}})=\sum_{\mu=\pm1/2}\langle\ell,\tfrac{1}{2},m-\mu,\mu|j,m\rangle\,Y_{\ell,m-\mu}(\hat{\mathbf{r}})\,\chi_\mu\,. \tag{1.1.14}$$

The quantities $\langle j_1j_2m_1m_2|j,m\rangle$ are Clebsch-Gordan coefficients, $Y_{\ell m}(\hat{\mathbf{r}})$ are spherical harmonics, and χ_μ are the Pauli unit spinors, *i.e.*, the eigenstates of S_P^2 and $S_{\mathrm{P}3}$ with eigenvalues $3/4$ and $\mu=\pm\frac{1}{2}$, respectively. More explicitly:

$$\chi_{+1/2}=\left|\tfrac{1}{2},\,+\tfrac{1}{2}\right\rangle=\begin{pmatrix}1\\0\end{pmatrix}\quad\text{and}\quad\chi_{-1/2}=\left|\tfrac{1}{2},\,-\tfrac{1}{2}\right\rangle=\begin{pmatrix}0\\1\end{pmatrix}, \tag{1.1.15}$$

Introducing the pauli spinors and writing the coefficients as reported in [39] Eq. (1.1.14) can be rewritten as:

$$\Omega^{\ell}_{\ell\pm1/2,m}(\hat{\mathbf{r}})=\frac{1}{\sqrt{2\ell+1}}\begin{pmatrix}\pm\sqrt{\ell\pm m+\frac{1}{2}}\,Y_{\ell,m-1/2}(\hat{\mathbf{r}})\\ \sqrt{\ell\mp m+\frac{1}{2}}\,Y_{\ell,m+1/2}(\hat{\mathbf{r}})\end{pmatrix}. \tag{1.1.16}$$

To simplify notation, it is customary to use the relativistic angular momentum quantum number

$$\kappa=(\ell-j)(2j+1)\,, \tag{1.1.17}$$

which specifies both the total angular momentum, j, and the parity, $(-1)^\ell$ of the Dirac spherical wave,

$$j = |\kappa| - \tfrac{1}{2}, \qquad \ell = j + \frac{\kappa}{2|\kappa|} = \left\{ \begin{array}{ll} \kappa & \text{if } \kappa > 0 \\ -\kappa - 1 & \text{if } \kappa < 0 \end{array} \right\} . \tag{1.1.18}$$

It is also convenient to consider the quantum number

$$\bar{\ell} \equiv \left\{ \begin{array}{ll} -\kappa & \text{if } \kappa < 0 \\ \kappa - 1 & \text{if } \kappa > 0 \end{array} \right\} = \ell - \frac{\kappa}{|\kappa|} , \tag{1.1.19}$$

which is the value of ℓ corresponding to $-\kappa$.

In the case of bound orbitals ($\epsilon < 0$), each discrete energy level is characterized by the principal quantum number n and the relativistic quantum number κ. Bound orbitals are normalized to unity and, consequently, satisfy the orthonormality relation

$$\int \psi^\dagger_{n'\kappa'm'}(\mathbf{r}) \psi_{n\kappa m}(\mathbf{r}) \, \mathrm{d}\mathbf{r} = \delta_{n'n} \, \delta_{\kappa'\kappa} \, \delta_{m'm} \, . \tag{1.1.20}$$

Free spherical waves (with $\epsilon > 0$) are normalized in such a way that the large-component radial function asymptotically oscillates with unit amplitude,

$$P_{\epsilon\kappa}(r) \underset{r\to\infty}{\sim} \sin\left(kr - \ell\frac{\pi}{2} - \eta \ln 2kr + \delta_\kappa\right) , \tag{1.1.21}$$

where

$$k = (c\hbar)^{-1} \sqrt{\epsilon(\epsilon + 2\mathrm{m_e}c^2)} \tag{1.1.22}$$

is the wave number, $\eta = [\lim_{r\to\infty} rV(r)]\mathrm{m_e}/(\hbar^2 k)$ is the Sommerfeld parameter, and δ_κ is the phase shift. Free spherical waves normalized in the form (1.1.21) satisfy the orthogonality relation

$$\int \psi^\dagger_{\epsilon'\kappa'm'}(\mathbf{r}) \psi_{\epsilon\kappa m}(\mathbf{r}) \, \mathrm{d}\mathbf{r} = \frac{\epsilon}{k} \, \pi \, \delta(\epsilon' - \epsilon) \, \delta_{\kappa'\kappa} \, \delta_{m'm} \, . \tag{1.1.23}$$

The state of a free electron with definite spin projection can be represented as a distorted plane wave (DPW), *i.e.*, a solution of the Dirac equation that asymptotically behaves as a plane wave plus an outgoing (+) or incoming (−) spherical wave. A DPW is characterized by the wave vector $\mathbf{k}$ of the asymptotic plane wave and the spin projection μ; it can be expanded in the basis of spherical waves as (see, *e.g.*, Refs. [36, 6, 40])

$$\psi^{(\pm)}_{\mathbf{k}\mu}(\mathbf{r}) = \frac{1}{k} \sqrt{\frac{\epsilon + 2\mathrm{m_e}c^2}{\pi(\epsilon + \mathrm{m_e}c^2)}} \sum_{\kappa,m} \mathrm{i}^\ell \, \exp\left(\pm \mathrm{i}\delta_\kappa\right) \, \left\{ \left[\Omega_{\kappa m}(\hat{\mathbf{k}})\right]^\dagger \chi_\mu \right\} \psi_{\epsilon\kappa m}(\mathbf{r}) \, , \tag{1.1.24}$$

where

$$\epsilon = \sqrt{(c\hbar k)^2 + (\mathrm{m_e}c^2)^2} - \mathrm{m_e}c^2 \tag{1.1.25}$$

is the kinetic energy of the particle. The expansion (1.1.24) is known as the partial-wave series. It can be easily verified that, with the adopted normalization for free spherical waves, DPWs satisfy the orthogonality relation

$$\int \left[\psi^{(\pm)}_{\mathbf{k}'\mu'}(\mathbf{r})\right]^{\dagger} \psi^{(\pm)}_{\mathbf{k}\mu}(\mathbf{r})\,\mathrm{d}\mathbf{r} = \delta(\mathbf{k}'-\mathbf{k})\,\delta_{\mu'\mu}\,. \tag{1.1.26}$$

1.1.2 Matrix elements of Racah tensors and the spin operator

The calculation of cross sections, presented in this work, requires the calculation of the matrix elements of the Racah Tensor defined by the following functions:

$$C_{LM}(\hat{\mathbf{r}}) \equiv \sqrt{\frac{4\pi}{2L+1}}\,Y_{LM}(\hat{\mathbf{r}})\,, \tag{1.1.27}$$

It is important to note that the $2L+1$ functions $C_{LM}(\hat{\mathbf{r}})$ constitute an irreducible tensor of rank L, $\mathbf{C}^{(L)}$. By virtue of the Wigner-Eckart theorem (see, *e.g.*, Ref. [41]), the matrix elements of Racah tensors for eigenstates $\Omega_{\kappa m}$ of the total angular momentum $\mathbf{J} = \mathbf{L}+\mathbf{S}_{\mathrm{P}}$ of a spin $\frac{1}{2}$ particle are

$$\begin{aligned}\langle \Omega_{\kappa_1 m_1}|C_{LM}|\Omega_{\kappa_2 m_2}\rangle &\equiv \int \left[\Omega_{\kappa_1 m_1}(\hat{\mathbf{r}})\right]^{\dagger} C_{LM}(\hat{\mathbf{r}})\,\Omega_{\kappa_2 m_2}(\hat{\mathbf{r}})\,\mathrm{d}\hat{\mathbf{r}} \\ &= \frac{1}{\sqrt{2j_1+1}}\,\langle j_2 L m_2 M|j_1 m_1\rangle\,\left\langle \ell_1 \tfrac{1}{2} j_1 \left\|\mathbf{C}^{(L)}\right\| \ell_2 \tfrac{1}{2} j_2 \right\rangle\,. \end{aligned} \tag{1.1.28}$$

The reduced matrix element $\left\langle \ell_1 \tfrac{1}{2} j_1 \left\|\mathbf{C}^{(L)}\right\| \ell_2 \tfrac{1}{2} j_2 \right\rangle$ is given by the expression (see, *e.g.*, Ref. [42])

$$\left\langle \ell_1 \tfrac{1}{2} j_1 \left\|\mathbf{C}^{(L)}\right\| \ell_2 \tfrac{1}{2} j_2 \right\rangle = \upsilon(L,\ell_1,\ell_2)\,\sqrt{2j_2+1}\,\langle L j_2 0 \tfrac{1}{2}|j_1 \tfrac{1}{2}\rangle\,, \tag{1.1.29}$$

where the factor

$$\upsilon(L,\ell_1,\ell_2) \equiv \begin{cases} 1 \text{ if } L+\ell_1+\ell_2 \text{ is even,} \\ 0 \text{ otherwise,} \end{cases} \tag{1.1.30}$$

accounts for the parity selection rule.

Matrix elements of spin operators can be evaluated by using the identity,

$$\begin{aligned}\Omega^{\dagger}_{\kappa_1 m_1}(\hat{\mathbf{r}})\,\boldsymbol{\sigma}\,\Omega_{\kappa_2 m_2}(\hat{\mathbf{r}}) = \sum_{J,M}(-1)^M \\ \times\Bigg\{\sqrt{\frac{J}{4\pi}}\left(\frac{\kappa_1+\kappa_2}{J}-1\right)\langle\Omega_{\kappa_1,m_1}|C_{JM}|\Omega_{-\kappa_2,m_2}\rangle\,\mathbf{Y}^{J-1}_{J,-M}(\hat{\mathbf{r}}) \\ +\sqrt{\frac{2J+1}{4\pi\,J(J+1)}}\,(\kappa_1-\kappa_2)\,\langle\Omega_{\kappa_1,m_1}|C_{JM}|\Omega_{\kappa_2,m_2}\rangle\,\mathbf{Y}^{J}_{J,-M}(\hat{\mathbf{r}}) \\ +\sqrt{\frac{J+1}{4\pi}}\left(\frac{\kappa_1+\kappa_2}{J+1}+1\right)\langle\Omega_{\kappa_1,m_1}|C_{JM}|\Omega_{-\kappa_2,m_2}\rangle\,\mathbf{Y}^{J+1}_{J,-M}(\hat{\mathbf{r}})\Bigg\}\,,\end{aligned} \tag{1.1.31}$$

where the functions $\mathbf{Y}^{L}_{JM}(\hat{\mathbf{r}})$ are the vector spherical harmonics, defined by (see, *e.g.*, Refs. [39, 40])

$$\mathbf{Y}^{L}_{JM}(\hat{\mathbf{r}}) = \sum_{\nu=-1}^{1}\langle L,1,M+\nu,-\nu|JM\rangle\,Y_{L,M+\nu}(\hat{\mathbf{r}})\,\boldsymbol{\xi}_{-\nu}\,, \tag{1.1.32}$$

where $\boldsymbol{\xi}_{\nu}$ are the spherical unit vectors,

$$\boldsymbol{\xi}_{+1} = \frac{1}{\sqrt{2}}\begin{pmatrix}-1\\ -\mathrm{i}\\ 0\end{pmatrix}, \qquad \boldsymbol{\xi}_{0} = \begin{pmatrix}0\\ 0\\ 1\end{pmatrix}, \qquad \boldsymbol{\xi}_{-1} = \frac{1}{\sqrt{2}}\begin{pmatrix}1\\ -\mathrm{i}\\ 0\end{pmatrix}. \tag{1.1.33}$$

It is important to underline that the vectors $\boldsymbol{\xi}_{\nu}$ represents an useful spherical base for expressing any vector $\mathbf{G}$ which can greatly simplify the calculations:

$$\mathbf{G} = \sum_{\nu}(-1)^{\nu}G_{\nu}\boldsymbol{\xi}_{-\nu}\,, \tag{1.1.34}$$

where

$$G_{\nu} = \boldsymbol{\xi}_{\nu}\cdot\mathbf{G} \tag{1.1.35}$$

are the spherical components, which constitute an irreducible tensor operator [38, 41]. The dot product of two vectors, $\boldsymbol{\zeta}$ and $\mathbf{G}$, is given by

$$\boldsymbol{\zeta}\cdot\mathbf{G} = \sum\zeta_i G_i = \sum_{\nu}(-1)^{\nu}\zeta_{\nu}G_{-\nu}\,, \tag{1.1.36}$$

where ζ_i, G_i and ζ_{ν}, G_{ν} are, respectively, the Cartesian and spherical components of the vectors.

1.1.3 The DHFS potential

The Dirac Hartree Fock Slater potential (i.e. DHFS potential) of an atom or ion of atomic number Z with N bound electrons is determined by the ground-state electron density, $\rho(r)$, which is obtained self-consistently (see, *e.g.*, [43, 44]). It is given by

$$V_{\mathrm{DHFS}}(r) = V_{\mathrm{nuc}}(r) + V_{\mathrm{el}}(r) + V_{\mathrm{ex}}(r)\,. \tag{1.1.37}$$

The term $V_{\mathrm{nuc}}(r)$ is the nuclear potential (*i.e.*, the electrostatic interaction energy of an electron at r with the nucleus, which is assumed to be spherical). For a point nucleus,

$$V_{\mathrm{nuc}}(r) = -Ze^2/r. \tag{1.1.38}$$

The effect of the finite size of the nucleus can be accounted for by using simple models for the nuclear charge distribution. A convenient parameterisation of the proton density is provided by the Fermi distribution [45],

$$\rho_{\mathrm{p}}(r) = \frac{\rho_0}{\exp\left[(r-R_{\mathrm{n}})/z\right]+1}\,, \tag{1.1.39}$$

with

$$R_{\mathrm{n}} = 1.07\,A^{1/3}\,\mathrm{fm}, \qquad \text{and} \qquad z = 0.546\,\mathrm{fm}\,, \tag{1.1.40}$$

where A is the mass number, which is usually replaced by the atomic weight (mean relative atomic mass) of the element. The constant ρ_0, which equals twice the proton density at $r = R_{\mathrm{n}}$, is to be determined by normalization. The nuclear potential for the Fermi distribution has to be calculated numerically,

$$\begin{aligned} V_{\mathrm{nuc}}(r) &= -e^2 \int \frac{\rho_{\mathrm{p}}(r')}{|\mathbf{r}-\mathbf{r}'|}\,\mathrm{d}\mathbf{r}' \\ &= -\frac{e^2}{r}\int_0^r \rho_{\mathrm{p}}(r')\,4\pi r'^2\,\mathrm{d}r' - e^2\int_r^\infty \rho_{\mathrm{p}}(r')\,4\pi r'\,\mathrm{d}r'\,. \end{aligned} \tag{1.1.41}$$

The second term in expression (1.1.37) is the electronic potential (*i.e.*, the interaction energy of an electron at r with the atomic electron cloud),

$$V_{\mathrm{el}}(r) = \frac{e^2}{r}\int_0^r \rho(r')\,4\pi r'^2\,\mathrm{d}r' + e^2\int_r^\infty \rho(r')\,4\pi r'\,\mathrm{d}r'\,, \tag{1.1.42}$$

and the last term is the local approximation to the exchange potential. Exchange interaction is a quantum mechanical effect (without any classical analogy) that only occurs between identical particles. It is not a true force (lack of force carriers like photons in electromagnetism interaction) and is due to the wave function of indistinguishable particles being subject to exchange symmetry, that is, either remaining unchanged (symmetric) or changing its sign (antisymmetric) when two particles are exchanged. Both bosons and fermions can experience the exchange interaction. For fermions, it is sometimes called Pauli repulsion and related to the Pauli exclusion principle. For bosons, the exchange interaction takes the form of an effective attraction that causes identical particles to be found closer together, as in BoseEinstein condensation. We use the Slater-Latter potential given by

$$V_{\rm ex}(r) = \begin{cases} V_{\rm ex}^{\rm Slater}(r) & \text{if } r < r_{\rm Latter}, \\ \\ -(Z-N+1)\dfrac{e^2}{r} - V_{\rm nuc}(r) - V_{\rm el}(r) & \text{if } r \geq r_{\rm Latter}, \end{cases} \tag{1.1.43}$$

where

$$V_{\rm ex}^{\rm Slater}(r) = -\frac{3}{2}e^2(3/\pi)^{1/3}[\rho(\mathbf{r})]^{1/3}. \tag{1.1.44}$$

is the exchange potential derived by Slater [46], and the cut-off radius $r_{\rm Latter}$ is the outer root of the equation

$$r\left[V_{\rm nuc}(r) + V_{\rm el}(r) + \alpha V_{\rm ex}^{\rm Slater}(r)\right] = -(Z-N+1)e^2. \tag{1.1.45}$$

The modification (1.1.43) of Slater's potential for $r > r_{\rm Latter}$, which ensures the correct behaviour of $V(r)$ at large radii, is known as Latter's tail correction [47].

1.1.4 Photon polarization

The polarization of photon beams that propagate in the direction of the z axis can be described in terms of the basis $\{|\hat{\boldsymbol{\epsilon}}_1\rangle, |\hat{\boldsymbol{\epsilon}}_2\rangle\}$ of linear polarisation states along the x and y axes. Pure polarisation states can be expressed in the form

$$|\boldsymbol{\zeta}\rangle = \cos(\alpha/2)|\hat{\boldsymbol{\epsilon}}_1\rangle + \sin(\alpha/2)\exp(\mathrm{i}\beta)|\hat{\boldsymbol{\epsilon}}_2\rangle = \begin{pmatrix} \cos(\alpha/2) \\ \sin(\alpha/2)\exp(\mathrm{i}\beta) \\ 0 \end{pmatrix} \tag{1.1.46}$$

with $\alpha \in [0,\pi]$ and $\beta \in (-\pi,\pi]$. There is a one-to-one correspondence between polarisation states $|\boldsymbol{\zeta}\rangle$ and polarisation vectors of electromagnetic waves, $\boldsymbol{\zeta} = \zeta_1\hat{\boldsymbol{\epsilon}}_1 + \zeta_2\hat{\boldsymbol{\epsilon}}_2$. The electric field $\boldsymbol{\mathcal{E}}$ of the polarized wave is given by

$$\boldsymbol{\mathcal{E}}(\mathbf{r},t) = \mathrm{Re}\Big\{ [\cos(\alpha/2)\,\hat{\boldsymbol{\epsilon}}_1 + \sin(\alpha/2)\,\exp(\mathrm{i}\beta)\,\hat{\boldsymbol{\epsilon}}_2]\,\exp[\mathrm{i}(\mathbf{k}\cdot\mathbf{r} - \omega t + \chi)] \Big\} \tag{1.1.47}$$

In the following, we simplify the notation by writing $\boldsymbol{\zeta}$ and $\hat{\boldsymbol{\epsilon}}_i$ instead of $|\boldsymbol{\zeta}\rangle$ and $|\hat{\boldsymbol{\epsilon}}_i\rangle$, *i.e.*, we use the same symbol to designate the quantum polarisation states and the unit polarisation vectors. States with $\beta = 0$ correspond to linear polarisation in a direction that makes an angle $\alpha/2$ with $\hat{\boldsymbol{\epsilon}}_1$. If $\beta = \pm\pi/2$ and $\alpha = \pi/2$, we have right-handed (r) and left-handed (l) circularly polarised photons[1],

$$\begin{aligned} \boldsymbol{\epsilon}^{(\mathrm{r})} &= \frac{1}{\sqrt{2}}(\hat{\boldsymbol{\epsilon}}_1 + \mathrm{i}\hat{\boldsymbol{\epsilon}}_2) = -\hat{\boldsymbol{\xi}}_{+1}, \\ \boldsymbol{\epsilon}^{(\mathrm{l})} &= \frac{1}{\sqrt{2}}(\hat{\boldsymbol{\epsilon}}_1 - \mathrm{i}\hat{\boldsymbol{\epsilon}}_2) = \boldsymbol{\xi}_{-1}, \end{aligned} \tag{1.1.48a}$$

---

[1] We consider "natural" right-handed polarization, which is opposite to the convention adopted in optics [48].

where $\boldsymbol{\xi}_{+1}$ and $\boldsymbol{\xi}_{-1}$ are the vectors of the spherical basis, Eq. (1.1.35).

Usually, real beams are partially polarized, that is, their photons are in various states $|\boldsymbol{\zeta}_n\rangle$ of pure polarisation with corresponding probabilities p_n. The states $|\boldsymbol{\zeta}_n\rangle$ are only assumed to be normalised to unity, their number and nature are arbitrary. The probabilities p_n are positive and add to unity. Polarization features of real beams can be described by using the density matrix formalism [49, 50, 51, 52]. The density operator for such a radiation beam is

$$\rho \equiv \sum_n |\boldsymbol{\zeta}_n\rangle\, p_n \langle\boldsymbol{\zeta}_n|. \tag{1.1.49}$$

The matrix of this operator in the basis of states of linear polarisation $\{\hat{\boldsymbol{\epsilon}}_1, \hat{\boldsymbol{\epsilon}}_2\}$ is Hermitian and has unit trace. It can be expressed as a linear combination of the Pauli matrices $\boldsymbol{\sigma}$, Eq. (1.1.3), and the 2×2 identity matrix, I_2, with real coefficients,

$$\rho = \frac{1}{2}\left(I_2 + P_1\sigma_1 + P_2\sigma_2 + P_3\sigma_3\right) = \frac{1}{2}\begin{pmatrix} 1+P_3 & P_1 - \mathrm{i}P_2 \\ P_1 + \mathrm{i}P_2 & 1-P_3 \end{pmatrix}. \tag{1.1.50}$$

The coefficients P_i are the *Stokes parameters*; they provide a complete description of the polarisation of a beam and can be measured experimentally [50]. We have $P_i = \mathrm{Tr}\rho\sigma_i$ or, more explicitly,

$$P_1 = \rho_{12} + \rho_{21}, \qquad P_2 = \mathrm{i}(\rho_{12} - \rho_{21}), \qquad P_3 = \rho_{11} - \rho_{22}. \tag{1.1.51}$$

It is worth mentioning that in optics the Pauli matrices, as well as the Stokes parameters, are usually considered in a different order, namely, $\{\sigma_3, \sigma_1, \sigma_2\}$. We prefer the ordering (1.1.3) employed in quantum mechanics because the formalism is thus parallel to that of polarisation of spin-$\frac{1}{2}$ particles.

The Stokes parameters can be regarded as the components of a vector, $\mathbf{P} \equiv (P_1, P_2, P_3)$, the Poincaré vector, which is analogous to the direction of spin of a spin-$\frac{1}{2}$ particle, although it transforms differently under rotations (see [51, 50]). For a pure state of the type (1.1.46) the density matrix takes the form

$$\rho = \begin{pmatrix} \cos^2(\alpha/2) & \cos(\alpha/2)\sin(\alpha/2)\exp(-\mathrm{i}\beta) \\ \cos(\alpha/2)\sin(\alpha/2)\exp(\mathrm{i}\beta) & \sin^2(\alpha/2) \end{pmatrix}, \tag{1.1.52}$$

and the associated Stokes parameters are

$$P_1 = \sin\alpha\,\cos\beta, \qquad P_2 = \sin\alpha\,\sin\beta, \qquad P_3 = \cos\alpha. \tag{1.1.53}$$

Note that α and β are the polar and azimuthal angles of the Poincaré vector $\mathbf{P}$, and that $P = 1$. In the opposite situation, when the Stokes parameters vanish, $P = 0$, the density matrix takes the form $\rho = \frac{1}{2}I_2$, which represents unpolarized photons. The magnitude P of the Poincaré vector measures the degree of polarization; it can take values from 0 (unpolarised photons) to 1 (pure polarisation states).

In the case of pure states ($P = 1$), inverting the relations (1.1.53), we obtain the state angles (α, β) from the Stokes parameters,

$$\alpha = \arccos P_3, \qquad \exp(\mathrm{i}\beta) = \frac{P_1 + \mathrm{i}P_2}{\sqrt{1 - P_3^2}}\,. \tag{1.1.54}$$

The pure states corresponding to the Poincaré vectors $\mathbf{P}$ and $-\mathbf{P}$, with respective directions (α, β) and $(\pi - \alpha, \beta + \pi)$, are

$$\boldsymbol{\zeta}(\mathbf{P}) = \begin{pmatrix} \cos(\alpha/2) \\ \sin(\alpha/2)\exp(\mathrm{i}\beta) \\ 0 \end{pmatrix} \qquad \text{and} \qquad \boldsymbol{\zeta}(-\mathbf{P}) = \begin{pmatrix} \sin(\alpha/2) \\ -\cos(\alpha/2)\exp(\mathrm{i}\beta) \\ 0 \end{pmatrix}. \tag{1.1.55}$$

Note that these states are orthogonal,

$$\langle \boldsymbol{\zeta}(\mathbf{P}) | \, \boldsymbol{\zeta}(-\mathbf{P}) \rangle = 0. \tag{1.1.56}$$

Hence, by reversing the signs of the Stokes parameters of a pure state, we obtain its orthogonal state (except for, possibly, an irrelevant phase factor). Thus, the state angles (α, β), the Poincaré vectors and the density matrices of the states $\{\hat{\boldsymbol{\epsilon}}_1, \hat{\boldsymbol{\epsilon}}_2\}$ of the linear-polarisation basis are

$$\hat{\boldsymbol{\epsilon}}_1 = \hat{\mathbf{x}} = \begin{pmatrix} 1 \\ 0 \\ 0 \end{pmatrix} \; : \; \begin{matrix} \alpha = 0 \\ \beta = 0 \end{matrix}, \quad \mathbf{P} = \begin{pmatrix} 0 \\ 0 \\ 1 \end{pmatrix}, \quad \rho = \frac{1}{2}\begin{pmatrix} 2 & 0 \\ 0 & 0 \end{pmatrix}, \tag{1.1.57a}$$

$$\hat{\boldsymbol{\epsilon}}_2 = \hat{\mathbf{y}} = \begin{pmatrix} 0 \\ 1 \\ 0 \end{pmatrix} \; : \; \begin{matrix} \alpha = \pi \\ \beta = \pi \end{matrix}, \quad \mathbf{P} = \begin{pmatrix} 0 \\ 0 \\ -1 \end{pmatrix}, \quad \rho = \frac{1}{2}\begin{pmatrix} 0 & 0 \\ 0 & 2 \end{pmatrix}. \tag{1.1.57b}$$

Similarly, for the states of the basis of circular polarisation, we have

$$\hat{\boldsymbol{\epsilon}}^{(\mathrm{r})} = -\boldsymbol{\xi}_{+1} = \frac{1}{\sqrt{2}}\begin{pmatrix} 1 \\ \mathrm{i} \\ 0 \end{pmatrix} \; : \; \begin{matrix} \alpha = \pi/2 \\ \beta = \pi/2 \end{matrix}, \quad \mathbf{P} = \begin{pmatrix} 0 \\ 1 \\ 0 \end{pmatrix}, \quad \rho = \frac{1}{2}\begin{pmatrix} 1 & -\mathrm{i} \\ \mathrm{i} & 1 \end{pmatrix}, \tag{1.1.58a}$$

$$\hat{\boldsymbol{\epsilon}}^{(\mathrm{l})} = \boldsymbol{\xi}_{-1} = \frac{1}{\sqrt{2}}\begin{pmatrix} 1 \\ -\mathrm{i} \\ 0 \end{pmatrix} \; : \; \begin{matrix} \alpha = \pi/2 \\ \beta = -\pi/2 \end{matrix}, \quad \mathbf{P} = \begin{pmatrix} 0 \\ -1 \\ 0 \end{pmatrix}, \quad \rho = \frac{1}{2}\begin{pmatrix} 1 & \mathrm{i} \\ -\mathrm{i} & 1 \end{pmatrix}. \tag{1.1.58b}$$

The *intensity* of a photon beam is defined as the number of photons that cross a unit surface perpendicular to the direction of the beam per unit time. Let us consider two photon beams with intensities I_1 and I_2 and respective density matrices ρ_1 and ρ_2.

The incoherent admixture of these two beams gives a beam with intensity $I = I_1 + I_2$ and density matrix

$$\rho = \frac{I_1}{I}\,\rho_1 + \frac{I_2}{I}\,\rho_2. \tag{1.1.59a}$$

The corresponding Stokes parameters are

$$\mathbf{P} = \frac{I_1}{I}\,\mathbf{P}_1 + \frac{I_2}{I}\,\mathbf{P}_2, \tag{1.1.59b}$$

where $\mathbf{P}_1$ and $\mathbf{P}_2$ are the Poincaré vectors of the initial beams. Notice that an unpolarized beam can be considered as the admixture of two completely polarised beams with equal intensities and "opposite" polarisations, $\mathbf{P}$ and $-\mathbf{P}$, whatever the direction of $\mathbf{P}$.

A partially polarised beam with Stokes parameters $\mathbf{P}$ $(P < 1)$ can be regarded as an incoherent admixture of an unpolarised beam and a completely polarised beam. To characterise these beams, we define the reduced Stokes parameters $P_i' \equiv P_i/P$. The matrix density of the partially polarised beam $\mathbf{P}$ can then be expressed as

$$\begin{aligned}\rho &= \frac{1}{2}\begin{pmatrix} 1+P_3 & P_1-\mathrm{i}P_2 \\ P_1+\mathrm{i}P_2 & 1-P_3 \end{pmatrix} \\ &= (1-P)\frac{1}{2}\begin{pmatrix} 1 & 0 \\ 0 & 1 \end{pmatrix} + P\frac{1}{2}\begin{pmatrix} 1+P_3' & P_1'-\mathrm{i}P_2' \\ P_1'+\mathrm{i}P_2' & 1-P_3' \end{pmatrix}. \end{aligned} \tag{1.1.60}$$

Hence, the original beam is equivalent to the mixture of an unpolarised beam and a completely polarised beam (with Poincaré vector $\mathbf{P}' = \mathbf{P}/P$, $P' = 1$), having relative intensities $(1-P)$ and P, respectively.

1.1.5 Derivation of the cross sections

In this section it will be summarized the derivation of the cross section of a beam of photons with energy $W = \hbar\omega$ and wave vector $\mathbf{k}$ $(k = \omega/c)$, polarized in a direction $\boldsymbol{\zeta}$ perpendicular to $\mathbf{k}$, incident on a target atom at the origin of coordinates. The absorption of a photon causes the transition of the active electron from the initial orbital ψ_a with energy $\epsilon_a < 0$, and ionization energy $E_a \equiv |\epsilon_a|$, to an excited orbital with energy $\epsilon_b = \epsilon_a + W$, which may be either bound (when $W < E_a$, excitation) or free (if $W > E_a$, ionization). To simplify calculations, it is considered that photons propagate along the direction of the z axis. This implies that the spherical components of the polarization vector [$\zeta_\nu = \boldsymbol{\xi}_\nu \cdot \boldsymbol{\zeta}$, see Eq. (1.1.34)] are such that $\zeta_0 = 0$ and $|\zeta_{-1}|^2 + |\zeta_{+1}|^2 = 1$. The Hamiltonian of the target atom in a radiation field can be expressed as:

$$\begin{aligned}\mathcal{H} &= \sum_{i=1}^{N}\left[c\,\widetilde{\boldsymbol{\alpha}}_i\cdot\mathbf{p}_i + e\,\widetilde{\boldsymbol{\alpha}}_i\cdot\mathbf{A}_i(\mathbf{r}_i,t) + \left(\widetilde{\beta}-1\right)\mathrm{m_e}c^2\right] \\ &\quad + \sum_{i=1}^{N} V_{nuc}(r_i) + \sum_{i<j=1}^{N}\frac{e^2}{|\mathbf{r}_i-\mathbf{r}_j|}\,, \end{aligned} \tag{1.1.61}$$

where, for the i-th atomic electron, $V_{nuc}(r_i)$ is the interaction energy of that electron with the nucleus (assumed spherical), and the last double summation is the Coulomb interaction between electrons. The summations run over the N electrons in the atom ($N < Z$ in the case of positive ions). Note that the nucleus is assumed to be fixed at the origin of the reference frame and is represented simply through its electrostatic potential $V_{nuc}(ri) = -e\varphi_{nuc}(r)$. This is equivalent to assuming that the nucleus has infinite mass, an assumption that is not appropriate for photons with energies that are comparable to the rest energy of the atom. We can rewrite Eq. as $\mathcal{H} = \mathcal{H}_0 + \mathcal{H}'(t)$ where $\mathcal{H}_0$ is the Hamiltonian of the target atom:

$$\mathcal{H}_0 = \sum_{i=1}^{N} \left[c\,\widetilde{\boldsymbol{\alpha}}_i \cdot \mathbf{p}_i + \left(\widetilde{\beta} - 1\right) \mathrm{m_e} c^2 \right] + \sum_{i=1}^{N} V_{nuc}(r_i) + \sum_{i<j=1}^{N} \frac{e^2}{|\mathbf{r}_i - \mathbf{r}_j|}\,, \tag{1.1.62}$$

and $\mathcal{H}'(t)$ is the Hamiltonian of the interaction between the atom and the radiation:

$$\mathcal{H}'(t) = e \sum_{i=1}^{N} \widetilde{\boldsymbol{\alpha}}_i \cdot \mathbf{A}_i(\mathbf{r}_i, t). \tag{1.1.63}$$

In Quantum electrodynamics (QED), electromagnetic radiation fields are treated using the formalism of second quantification. The electromagnetic field in vacuum is represented by the vector potential operator [53]:

$$\mathbf{A}(\mathbf{r}, t) = \sum_{\mathbf{k},\alpha} \sqrt{\frac{2\pi\hbar c^2}{L^3\omega}} \left\{ a_{\mathbf{k}\alpha} \hat{\boldsymbol{\epsilon}}_\alpha \exp[\mathrm{i}(\mathbf{k}\cdot\mathbf{r} - \omega t)] + a^\dagger_{\mathbf{k}\alpha} \hat{\boldsymbol{\epsilon}}^*_\alpha \exp[-\mathrm{i}(\mathbf{k}\cdot\mathbf{r} - \omega t)] \right\}. \tag{1.1.64}$$

where $a_{\mathbf{k}\alpha}(0)$ and $a^\dagger_{\mathbf{k}\alpha}(0)$ are creation and annihilation operators and the sum is over wave numbers k and over the two polarization states $\hat{\boldsymbol{\epsilon}}_\alpha$. Here r is not regarded as a quantum dynamical variable, but simply as a parameter that modulates the operator (it has nothing to do with the position coordinates of a photon). The frequency ω of each mode k is given by $\omega = ck$. The constant under the square root corresponds to the monochromatic plane waves obeying periodic boundary conditions on a cubic box with edges of length L. To simplify the formulas, we introduce the (dimensionless) operators:

$$M_{\mathbf{k}\alpha} = \hat{\boldsymbol{\epsilon}}_\alpha \cdot \sum_{i=1}^{N} \widetilde{\boldsymbol{\alpha}}_i \exp(\mathrm{i}\mathbf{k} \cdot \mathbf{r}_i)\,, \tag{1.1.65}$$

The Hamiltonian of interaction can be rewritten as:

$$\mathcal{H}'(t) = \sum_{\mathbf{k},\alpha} \sqrt{\frac{2\pi\hbar c^2 e^2}{L^3\omega}} \left[a_{\mathbf{k}\alpha} M_{\mathbf{k}\alpha} \exp(-\mathrm{i}\omega t) + a^\dagger_{\mathbf{k}\alpha} M^\dagger_{\mathbf{k}\alpha} \exp(\mathrm{i}\omega t) \right]. \tag{1.1.66}$$

In most practical cases, the interaction between the atom and the radiation field is weak and $\mathcal{H}'(t)$ can be treated as a perturbation. It can be assumed that, sometime in the past, the atom was prepared in a bound state ψ_A with energy E_A satisfying the Dirac Equation:

$$\mathcal{H}_0 \Psi_A = E_A \Psi_A. \tag{1.1.67}$$

The interaction with the radiation field may cause transitions of the atom from the initial state Ψ_A to other states Ψ_B, by absorption or emission of photons. If the initial radiation field contains photons with large enough energy $\hbar\omega$, absorption of these photons may cause the ionization of the atom, i.e., the transition to a final state in which one of the atomic electrons is in a free orbital with positive energy. The interaction also modifes the state of the field. In emission and absorption processes, the number of photons in the active mode $\mathbf{k}\alpha$ is reduced or increased in one unit (at least). Photons can also be scattered by the target atom. In a scattering event, the incident photon is absorbed and a new photon is emitted, so that the number of photons in the field remains constant. The target atom may either remain in the initial energy level (Rayleigh scattering), change to another bound level (Raman scattering) or be ionized (Compton scattering). Here it is assumed that the radiation field is weak enough (i.e., the number of photons in each mode $\mathbf{k}\alpha$ is sufficiently small) for the interaction $\mathcal{H}'(t)$ to be considered as a perturbation and it will be considered the process of absorption of photons.

It is important to underline that the operator $\mathcal{H}'(t)$ acts on the space of states of the whole system (atom plus radiation field) which is the direct product of the state space of the atom and the Fock space of the radiation field. The base states of the system are of the form:

$$\Phi = \mid \Psi \,\rangle \otimes \mid n_{\mathbf{k}_1\alpha_1}, n_{\mathbf{k}_2\alpha_2}, \ldots \rangle \equiv \mid \Psi, n_{\mathbf{k}_1\alpha_1}, n_{\mathbf{k}_2\alpha_2}, \ldots \rangle \;, \tag{1.1.68}$$

where Ψ is an eigenstate of $\mathcal{H}_0$ with energy E and $\mid n_{\mathbf{k}_1\alpha_1}, n_{\mathbf{k}_2\alpha_2}, \ldots \rangle$ is a vector of the symmetrical basis of Fock's space representing a field with $n_{\mathbf{k}_i\alpha_i}$ photons in the mode $\mathbf{k}_i\alpha_i$ for $i = 1, 2, \ldots, \infty$. In order to compute the cross section for photoeffect it will be necessary to compute the matrix elements $\langle \Phi_B \left| \mathcal{H}'(t) \right| \Phi_A \rangle$ of the interaction Hamiltonian.

It can be showed [53] that the matrix elements of the operator $M_{\mathbf{k}\alpha}$, $\langle \Phi_B \left| M_{\mathbf{k}\alpha} \right| \Phi_A \rangle$, are different from zero only when the final and initial states differs in a single photon. The same holds for the Hamiltonian $\mathcal{H}'(t)$. Hence, to first order of perturbation theory, the interaction can only cause the emission or absorption of a single photon by the atom. To study processes that involve 2 (or more) photons, the interaction has to be treated using second (or higher) order perturbation theory. In particular, to describe scattering processes we need to use second-order perturbation theory. It is also assumed that radiation beams are incoherent, that is, that there are no correlations between the photons in the beam. This is true for photon beams from a hot gas, because photons are emitted at random by the individual atoms in the gas. When the beam is incoherent, the transition rate is obtained by simply adding the transition rates corresponding to each mode $\mathbf{k}\alpha$ (i.e., there is no interference between the various modes). Note that the two assumptions (weak and incoherent fields) may not hold for laser fields, because the light from these devices has a high degree of coherence and because high-power laser beams may be very intense. In intense low-energy laser beams, simultaneous absorption of several photons has been observed.

With this assumptions it is possible to calculate transition rates using the Fermi Golden Rule for free final state:

$$\mathrm{d}w_{BA,\mathbf{k}\alpha} = \frac{2\pi}{\hbar}\frac{\mathrm{d}\mathcal{N}}{\mathrm{d}\epsilon_B\,\mathrm{d}\hat{\mathbf{k}}_B}\left|\mathcal{H}'_{BA}\right|^2\delta(\epsilon_B-\epsilon_A-\hbar\omega)\,\mathrm{d}\epsilon_B\,\mathrm{d}\hat{\mathbf{k}}_B, \tag{1.1.69}$$

where $\mathrm{d}\mathcal{N}/\mathrm{d}\epsilon_B\,\mathrm{d}\hat{\mathbf{k}}_B$ is the density of the final states of the electron:

$$\frac{\mathrm{d}\mathcal{N}}{\mathrm{d}\epsilon_B\,\mathrm{d}\hat{\mathbf{k}}_B} = k_B\frac{\epsilon_B+m_ec^2}{(c\hbar)^2} \tag{1.1.70}$$

and $\mathcal{H}'_{BA}(t) = \langle\Phi_B\left|\mathcal{H}'(t)\right|\Phi_A\rangle$. In the case of of bounded final state the Fermi golden rule becomes:

$$w_{BA,\mathbf{k}\alpha} = \frac{2\pi}{\hbar}\left|\mathcal{H}'_{BA}\right|^2\delta(\epsilon_B-\epsilon_A-\hbar\omega)\,, \tag{1.1.71}$$

The matrix element of the interaction operator is:

$$\mathcal{H}'_{BA}(t) \;=\; \sum_{\mathbf{k},\alpha}\sqrt{\frac{2\pi\hbar c^2e^2}{L^3\omega}}\left\langle\Phi_B\left|a_{\mathbf{k}\alpha}M_{\mathbf{k}\alpha}\exp(-\mathrm{i}\omega t)+a^\dagger_{\mathbf{k}\alpha}M^\dagger_{\mathbf{k}\alpha}\exp(\mathrm{i}\omega t)\right|\Phi_A\right\rangle \tag{1.1.72}$$

which can be rewritten using the properties of the creation and annihilation operators (for the case of absorption) as:

$$\begin{aligned}\mathcal{H}'_{BA}(t) \;=\; &\sum_{\mathbf{k},\alpha}\sqrt{\frac{2\pi\hbar c^2e^2}{L^3\omega}}\,\{\,(M_{\mathbf{k}\alpha})_{BA}\,\langle n_{\mathbf{k}\alpha}-1\left|a_{\mathbf{k}\alpha}\right|n_{\mathbf{k}\alpha}\rangle\exp(-\mathrm{i}\omega t)\\ &+(M^\dagger_{\mathbf{k}\alpha})_{BA}\left\langle n_{\mathbf{k}\alpha}-1\left|a^\dagger_{\mathbf{k}\alpha}\right|n_{\mathbf{k}\alpha}\right\rangle\exp(\mathrm{i}\omega t)\,\}\;,\end{aligned} \tag{1.1.73}$$

where:

$$(M_{\mathbf{k}\alpha})_{BA} \;=\; \left\langle\Psi_B\left|\hat{\boldsymbol{\epsilon}}_\alpha\cdot\sum_{i=1}^{N}\widetilde{\boldsymbol{\alpha}}_i\exp\left(\mathrm{i}\mathbf{k}\cdot\mathbf{r}_i\right)\right|\Psi_A\right\rangle. \tag{1.1.74}$$

Considering the definition of the matrix element, the only term which gives a non zero contribution is:

$$\langle n_{\mathbf{k}\alpha}-1\left|a_{\mathbf{k}\alpha}\right|n_{\mathbf{k}\alpha}\rangle = \sqrt{n_{\mathbf{k}\alpha}}\,, \tag{1.1.75}$$

so the matrix element of the interaction operator becomes:

$$\mathcal{H}'_{BA}(t) \;=\; \sqrt{\frac{2\pi\hbar c^2e^2}{L^3\omega}}(M_{\mathbf{k}\alpha})_{BA}\sqrt{n_{\mathbf{k}\alpha}}\,, \tag{1.1.76}$$

In order to simplify the formulation of the theory, and also to facilitate numerical calculations, it will be assumed that the target atom can be described by using an independent-electron model(IEM). In the calculations it will be used the DHFS self-consistent potential $V_{DHFS}(r)$, which means that the atomic Hamiltonian in Eq. is approximated by the IEM Hamiltonian:

$$\mathcal{H}_0 \approx \sum_{i=1}^{N} \mathcal{H}_i \,, \tag{1.1.77}$$

with

$$\mathcal{H}_i = c\,\widetilde{\boldsymbol{\alpha}}_i \cdot \mathbf{p}_i + \widetilde{\beta}\mathrm{m_e}c^2 + V_{DHFS}(r). \tag{1.1.78}$$

The one-active-electron approximation consists of considering only the excitations of a single electron from a bound orbital to an unoccupied (bound or free) final one, whereas the other atomic electrons behave as mere spectators and their orbitals remain frozen in the course of the interaction. This approximation amounts to neglecting correlation effects. This loose term refers to approximations underlying the IEM model and to possible readjustments of the orbitals of inactive electrons during the interaction. This allows to simplify the function Ψ in the so called Slater determinants [53]:

$$\Psi = \frac{1}{\sqrt{N!}}\det(\Psi) = \frac{1}{\sqrt{N!}} \begin{vmatrix} \psi_1(\mathbf{r}_1) & \dots & \psi_1(\mathbf{r}_N) \\ \vdots & \ddots & \vdots \\ \psi_N(\mathbf{r}_1) & \dots & \psi_N(\mathbf{r}_N) \end{vmatrix} , \tag{1.1.79}$$

build with one-electron orbitals $\psi_i(\mathbf{r}_i)$ that are solutions of the Dirac equation for the DHFS self-consistent potential:

$$\left[c\,\widetilde{\boldsymbol{\alpha}} \cdot \mathbf{p} + \left(\widetilde{\beta} - 1\right)\mathrm{m_e}c^2 + V_{DHFS}(r)\right]\psi_\nu(\mathbf{r}) = \epsilon_\nu \psi_\nu(\mathbf{r}). \tag{1.1.80}$$

Following the Slater-Condon rule Eq.(1.1.74) is simplified giving:

$$(M_{\mathbf{k}\alpha})_{BA} = \langle \psi_B \left| \hat{\boldsymbol{\epsilon}}_\alpha \cdot \widetilde{\boldsymbol{\alpha}} \exp\left(\mathrm{i}\mathbf{k} \cdot \mathbf{r}\right) \right| \psi_A \rangle \tag{1.1.81}$$

For exitation we have:

$$w_{BA,\mathbf{k}\alpha} = \frac{(2\pi)^2 \hbar c^2 e^2}{W} \frac{n_{\mathbf{k}\alpha}}{L^3} \left| M_{\mathbf{k}\alpha} \right|^2 \delta(\epsilon_B - \epsilon_A - \hbar\omega) \,, \tag{1.1.82}$$

where the quantity $n_{\mathbf{k}\alpha} c/L^3$ represents the flux of photons in the incident beam. Dividing the transition rate for this quantity it can be obtained the cross section for excitation of the active electron to a bound orbital, $\psi_b = \psi_{n_b \kappa_b m_b}$:

$$\sigma^{\mathrm{exc},1}_{n_b\kappa_b m_b; n_a\kappa_a m_a}(W, \boldsymbol{\zeta}) = \frac{(2\pi)^2 e^2 c\hbar}{W} \left| M^{\mathrm{exc}}_{n_b\kappa_b m_b; n_a\kappa_a m_a}(W, \boldsymbol{\zeta}) \right|^2 \delta(\epsilon_b - \epsilon_a - W) \,, \tag{1.1.83}$$

with the transition matrix element which can be computed in spherical components as:

$$M^{\mathrm{exc}}_{n_b\kappa_b m_b; n_a\kappa_a m_a}(W, \boldsymbol{\zeta}) = \boldsymbol{\zeta} \cdot \mathbf{G}^{\mathrm{exc}}(\kappa_b m_b; \kappa_a m_a) \,, \tag{1.1.84}$$

where

$$\mathbf{G}^{\rm exc}(\kappa_b m_b;\kappa_a m_a) \equiv \langle \psi_{n_b\kappa_b m_b}|\,\widetilde{\boldsymbol{\alpha}}\exp(\mathrm{i}\mathbf{k}\cdot\mathbf{r})|\,\psi_{n_a\kappa_a m_a}\rangle\ . \tag{1.1.85}$$

The delta distribution in Eq. (1.1.83) indicates that absorption is possible only at resonance, *i.e.*, when the excitation energy $\epsilon_b - \epsilon_a$ coincides with the energy of the photon. A finite cross, which varies continuously with the photon energy, is obtained when the energy width of atomic levels is taken into account.

In the case of ionization, the final orbital belongs to the continuum spectrum ($\epsilon_b > 0$). The differential cross section (DCS) for absorption of a photon, with emission of the active electron with spin $m_{\mathrm{S}b}$, linear momentum $\hbar\mathbf{k}_b$, and direction of motion within the solid angle element $\mathrm{d}\hat{\mathbf{k}}_b$ about the direction $\hat{\mathbf{k}}_b$, is [6, 7]:

$$\mathrm{d}w_{BA,\mathbf{k}\alpha} = \frac{(2\pi)^2\hbar c^2 e^2}{W}\frac{n_{\mathbf{k}\alpha}}{L^3}\,k_B\frac{\epsilon_B + m_e c^2}{(c\hbar)^2}\,|M_{\mathbf{k}\alpha}|^2\,\delta(\epsilon_B - \epsilon_A - W)\,\mathrm{d}\epsilon_B\,\mathrm{d}\hat{\mathbf{k}}_B, \tag{1.1.86}$$

which becomes as done for the excitation case:

$$\mathrm{d}\sigma^{\rm ion,1}_{b;n_a\kappa_a m_a}(W,\boldsymbol{\zeta}) = \frac{(2\pi)^2 e^2}{W}\,\frac{k_b(\epsilon_b + \mathrm{m_e}c^2)}{c\hbar}\,\left|M^{\rm ion}_{b;n_a\kappa_a m_a}(W,\boldsymbol{\zeta})\right|^2\,\mathrm{d}\hat{\mathbf{k}}_b\,, \tag{1.1.87}$$

where the transition matrix element

$$M^{\rm ion}_{b;n_a\kappa_a m_a}(W,\boldsymbol{\zeta}) = \boldsymbol{\zeta}\cdot\left\langle \psi^{(-)}_{\mathbf{k}_b m_{\mathrm{S}b}}\right|\widetilde{\boldsymbol{\alpha}}\exp(\mathrm{i}\mathbf{k}\cdot\mathbf{r})\left|\,\psi_{n_a\kappa_a m_a}\right\rangle \tag{1.1.88}$$

is to be evaluated on the energy shell, *i.e.*, with $\epsilon_b = \epsilon_a + W$. Inserting the expansion (1.1.24) of the DPW, the matrix element becomes

$$\begin{aligned} M^{\rm ion}_{b;n_a\kappa_a m_a}(W,\boldsymbol{\zeta}) \ &= \ \frac{1}{k_b}\sqrt{\frac{\epsilon_b + 2\mathrm{m_e}c^2}{\pi(\epsilon_b + \mathrm{m_e}c^2)}}\,\sum_{\kappa_b,m_b}\mathrm{i}^{-\ell_b}\,\exp\left(\mathrm{i}\delta_{\kappa_b}\right)\boldsymbol{\zeta}\cdot\mathbf{G}^{\rm ion}(\kappa_b m_b;\kappa_a m_a) \\ &\qquad \times\left[\chi^\dagger_{m_{\mathrm{S}b}}\Omega_{\kappa_b m_b}(\hat{\mathbf{k}}_b)\right]\ , \end{aligned} \tag{1.1.89}$$

where

$$\mathbf{G}^{\rm ion}(\kappa_b m_b;\kappa_a m_a) = \langle \psi_{\epsilon_b\kappa_b m_b}|\,\widetilde{\boldsymbol{\alpha}}\exp(\mathrm{i}\mathbf{k}\cdot\mathbf{r})|\,\psi_{n_a\kappa_a m_a}\rangle\ , \tag{1.1.90}$$

are matrix elements of the operator $\widetilde{\boldsymbol{\alpha}}\exp(\mathrm{i}\mathbf{k}\mathbf{r})$ in the basis of spherical waves, analogous to those of excitation.

1.1.6 One-electron transition-matrix elements

The matrix elements (1.1.85) and (1.1.90) are of the type

$$M_{ba} = \boldsymbol{\zeta}\cdot\mathbf{G} \quad \text{with} \quad \mathbf{G} = \langle \psi_{\epsilon_b\kappa_b m_b}\,|\widetilde{\boldsymbol{\alpha}}\exp(\mathrm{i}\mathbf{k}\cdot\mathbf{r})|\,\psi_{\epsilon_a\kappa_a m_a}\rangle\ , \tag{1.1.91}$$

where, in general, the polarization vector $\boldsymbol{\zeta}$ may be complex. To calculate the spherical components of $\mathbf{G}$, Eq. (1.1.35), it is introduced the Rayleigh expansion of the plane wave,

$$\exp(\mathrm{i}\mathbf{k}\cdot\mathbf{r}) = \sum_{J=0}^{\infty}\sum_{M=-J}^{J} \mathrm{i}^J(2J+1)\, j_J(kr)\, C^*_{JM}(\hat{\mathbf{k}})\, C_{JM}(\hat{\mathbf{r}})\,, \tag{1.1.92}$$

where $j_J(kr)$ are spherical Bessel functions. The formulas become simpler if it is considered a reference frame with the z axis parallel to the direction $\hat{\mathbf{k}}$ of the photon. In such a frame, $C^*_{JM}(\hat{\mathbf{k}}) = \delta_{M0}$, and it is possible to write

$$\mathbf{G} = \sum_J \mathrm{i}^J(2J+1)\, \langle\psi_{\epsilon_b\kappa_b m_b}\,|\widetilde{\boldsymbol{\alpha}}\, j_J(kr)\, C_{J0}(\hat{\mathbf{r}})|\, \psi_{\epsilon_a\kappa_a m_a}\rangle\ . \tag{1.1.93}$$

The matrix elements in this expression can be evaluated on the basis of Eq. (1.1.31), by a method similar to the one adopted by Mann and Johnson [54] for a related problem. After a rather tedious calculation it is found the following expressions for the spherical components of $\mathbf{G}$,

$$\begin{aligned} G_{+1}(\kappa_b,m_b;\kappa_a,m_a) \;=\; & \sum_{J=1}^{\infty} \mathrm{i}^J\, \frac{2J+1}{\sqrt{2J(J+1)}}\, \Big\{ \langle\Omega_{\kappa_b,m_b}|C_{J,+1}|\Omega_{\kappa_a,m_a}\rangle\, {}^{\mathrm{e}}\mathcal{R}^J_{\epsilon_b\kappa_b;\epsilon_a\kappa_a} \\ & + \mathrm{i}\, \langle\Omega_{\kappa_b,m_b}|C_{J,+1}|\Omega_{-\kappa_a,m_a}\rangle\, {}^{\mathrm{m}}\mathcal{R}^J_{\epsilon_b\kappa_b;\epsilon_a\kappa_a} \Big\}\,, \end{aligned} \tag{1.1.94a}$$

$$\begin{aligned} G_{-1}(\kappa_b,m_b;\kappa_a,m_a) \;=\; & \sum_{J=1}^{\infty} \mathrm{i}^J\, \frac{2J+1}{\sqrt{2J(J+1)}}\, \Big\{ \langle\Omega_{\kappa_b,m_b}|C_{J,-1}|\Omega_{\kappa_a,m_a}\rangle\, {}^{\mathrm{e}}\mathcal{R}^J_{\epsilon_b\kappa_b;\epsilon_a\kappa_a} \\ & - \mathrm{i}\, \langle\Omega_{\kappa_b,m_b}|C_{J,-1}|\Omega_{-\kappa_a,m_a}\rangle\, {}^{\mathrm{m}}\mathcal{R}^J_{\epsilon_b\kappa_b;\epsilon_a\kappa_a} \Big\}, \end{aligned} \tag{1.1.94b}$$

and

$$G_0(\kappa_b,m_b;\kappa_a,m_a) \;=\; \sum_{J=0}^{\infty} \mathrm{i}^J\,(2J+1)\, \langle\Omega_{\kappa_b,m_b}|C_{J,0}|\Omega_{\kappa_a,m_a}\rangle\, {}^{\mathrm{l}}\mathcal{R}^J_{\epsilon_b\kappa_b;\epsilon_a\kappa_a}, \tag{1.1.94c}$$

with the radial integrals

$$\begin{aligned} {}^{\mathrm{l}}\mathcal{R}^J_{\epsilon_b\kappa_b;\epsilon_a\kappa_a} \;=\; & \frac{1}{2J+1}\Big[(\kappa_b-\kappa_a)\,(F^{J-1}_{\epsilon_b\kappa_b;\epsilon_a\kappa_a} + G^{J-1}_{\epsilon_b\kappa_b;\epsilon_a\kappa_a}) - J(F^{J-1}_{\epsilon_b\kappa_b;\epsilon_a\kappa_a} - G^{J-1}_{\epsilon_b\kappa_b;\epsilon_a\kappa_a}) \\ & + (\kappa_b-\kappa_a)\,(F^{J+1}_{\epsilon_b\kappa_b;\epsilon_a\kappa_a} + G^{J+1}_{\epsilon_b\kappa_b;\epsilon_a\kappa_a}) + (J+1)(F^{J+1}_{\epsilon_b\kappa_b;\epsilon_a\kappa_a} - G^{J+1}_{\epsilon_b\kappa_b;\epsilon_a\kappa_a})\Big]\,, \end{aligned} \tag{1.1.95a}$$

$$\begin{aligned} {}^{\mathrm{e}}\mathcal{R}^J_{\epsilon_b\kappa_b;\epsilon_a\kappa_a} \;=\; & \frac{J(J+1)}{2J+1}\Big[\frac{\kappa_b-\kappa_a}{J}\,(F^{J-1}_{\epsilon_b\kappa_b;\epsilon_a\kappa_a} + G^{J-1}_{\epsilon_b\kappa_b;\epsilon_a\kappa_a}) - (F^{J-1}_{\epsilon_b\kappa_b;\epsilon_a\kappa_a} - G^{J-1}_{\epsilon_b\kappa_b;\epsilon_a\kappa_a}) \\ & -\frac{\kappa_b-\kappa_a}{J+1}\,(F^{J+1}_{\epsilon_b\kappa_b;\epsilon_a\kappa_a} + G^{J+1}_{\epsilon_b\kappa_b;\epsilon_a\kappa_a}) - (F^{J+1}_{\epsilon_b\kappa_b;\epsilon_a\kappa_a} - G^{J+1}_{\epsilon_b\kappa_b;\epsilon_a\kappa_a})\Big]\,, \end{aligned} \tag{1.1.95b}$$

and

$$^{\mathrm{m}}\mathcal{R}^{J}_{\epsilon_b\kappa_b;\epsilon_a\kappa_a} = (\kappa_a+\kappa_b)\,(F^{J}_{\epsilon_b\kappa_b;\epsilon_a\kappa_a}+G^{J}_{\epsilon_b\kappa_b;\epsilon_a\kappa_a}), \tag{1.1.95c}$$

where

$$F^{J}_{\epsilon_b\kappa_b;\epsilon_a\kappa_a} \equiv \int_0^\infty P_{\epsilon_b\kappa_b}(r)\,Q_{\epsilon_a\kappa_a}(r)\,j_J(kr)\,\mathrm{d}r, \tag{1.1.96a}$$

$$G^{J}_{\epsilon_b\kappa_b;\epsilon_a\kappa_a} \equiv \int_0^\infty Q_{\epsilon_b\kappa_b}(r)\,P_{\epsilon_a\kappa_a}(r)\,j_J(kr)\,\mathrm{d}r. \tag{1.1.96b}$$

The superscripts "l", "e" and "m" in the integrals (1.1.95) stand for "longitudinal", "electric" and "magnetic", respectively, because these radial integrals also arise in an alternative treatment based on the multipole expansion of the radiation field (see, *e.g.*, [55, 56]).

We recall that the matrix elements $\langle\Omega_{\kappa_b,m_b}|C_{J,\nu}|\Omega_{\kappa_a,m_a}\rangle$ vanish unless $m_b = m_a+\nu$. Moreover, at least one of the elements $\langle\Omega_{\kappa_b,m_b}|C_{J,\nu}|\Omega_{\kappa_a,m_a}\rangle$ and $\langle\Omega_{\kappa_b,m_b}|C_{J,\nu}|\Omega_{-\kappa_a,m_a}\rangle$ vanishes because the values of ℓ_a for κ_a and $-\kappa_a$ differ by one unit and, therefore, the parity factor $\upsilon(J,\ell_b,\ell_a)$ is null for one of these matrix elements. Hence, the two terms in curly braces on the right-hand side of Eqs. (1.1.94a) and (1.1.94b) cannot be both different from zero.

More compact formulas are obtained by introducing the quantities

$$^{\mathrm{l}}\mathcal{Y}^{J}_{\epsilon_b\kappa_b;\epsilon_a\kappa_a} \equiv \sqrt{2J+1}\,\left\langle \ell_b\tfrac{1}{2}j_b\left\|\mathbf{C}^{(L)}\right\|\ell_a\tfrac{1}{2}j_a\right\rangle{}^{\mathrm{l}}\mathcal{R}^{J}_{\epsilon_b\kappa_b;\epsilon_a\kappa_a}, \tag{1.1.97a}$$

$$^{\mathrm{e}}\mathcal{Y}^{J}_{\epsilon_b\kappa_b;\epsilon_a\kappa_a} \equiv \sqrt{\frac{2J+1}{2J(J+1)}}\,\left\langle \ell_b\tfrac{1}{2}j_b\left\|\mathbf{C}^{(L)}\right\|\ell_a\tfrac{1}{2}j_a\right\rangle{}^{\mathrm{e}}\mathcal{R}^{J}_{\epsilon_b\kappa_b;\epsilon_a\kappa_a}, \tag{1.1.97b}$$

$$^{\mathrm{m}}\mathcal{Y}^{J}_{\epsilon_b\kappa_b;\epsilon_a\kappa_a} \equiv \sqrt{\frac{2J+1}{2J(J+1)}}\,\left\langle \ell_b\tfrac{1}{2}j_b\left\|\mathbf{C}^{(L)}\right\|\bar{\ell}_a\tfrac{1}{2}j_a\right\rangle{}^{\mathrm{m}}\mathcal{R}^{J}_{\epsilon_b\kappa_b;\epsilon_a\kappa_a}, \tag{1.1.97c}$$

where $\bar{\ell}_a$ is the orbital angular momentum quantum number corresponding to $-\kappa_a$. Considering the symmetry properties of Clebsch-Gordan coefficients it is possible to write

$$G_{\pm1} = (-1)^{j_a-m_a}\sum_{J=1}^{\infty}\mathrm{i}^J\,\langle j_a,j_b,m_a,-m_b|J,\mp1\rangle\left\{{}^{\mathrm{e}}\mathcal{Y}^{J}_{\epsilon_b\kappa_b;\epsilon_a\kappa_a}\pm\mathrm{i}\,{}^{\mathrm{m}}\mathcal{Y}^{J}_{\epsilon_b\kappa_b;\epsilon_a\kappa_a}\right\} \tag{1.1.98a}$$

and

$$G_0 = (-1)^{j_a-m_a}\sum_{J=0}^{\infty}\mathrm{i}^J\,\langle j_a,j_b,m_a,-m_b|J,0\rangle\,{}^{\mathrm{l}}\mathcal{Y}^{J}_{\epsilon_b\kappa_b;\epsilon_a\kappa_a}. \tag{1.1.98b}$$

The cross section for photoabsorption by the electrons in a closed subshell $(n_a\kappa_a)^{2|\kappa_a|}$ is proportional to the sum of squared transition-matrix elements over magnetic quantum numbers, Eqs. (1.1.103) and (1.1.110),

$$\mathcal{G}_{ba} \equiv \sum_{m_a,m_b} |M_{ba}|^2 = \sum_{\nu,\nu'} (-1)^{\nu+\nu'} \zeta_{-\nu} \zeta^*_{-\nu'} \sum_{m_a,m_b} G_\nu G^*_{\nu'} \,. \tag{1.1.99}$$

Since the photon polarization vector $\boldsymbol{\zeta}$ is perpendicular to the wave vector $\mathbf{k} = k\hat{\mathbf{z}}$ and normalized to unity, it is $\zeta_0 = 0$ and $|\zeta_{-1}|^2 + |\zeta_{+1}|^2 = 1$. We note that the only dependence on the quantum numbers m_a and m_b is through the Clebsch-Gordan coefficients $\langle j_a, j_b, m_a, -m_b | J, \nu \rangle$. The summation over these quantum numbers is performed easily by using the orthogonality property of these coefficients. We thus obtain,

$$\sum_{m_a,m_b} G_{\pm 1} G^*_{\mp 1} = 0, \tag{1.1.100a}$$

and

$$\sum_{m_a,m_b} G_{\pm 1} G^*_{\pm 1} = \sum_{J=1}^{\infty} \left\{ \left[{}^{\mathrm{e}}\mathcal{Y}^J_{\epsilon_b \kappa_b; \epsilon_a \kappa_a} \right]^2 + \left[{}^{\mathrm{m}}\mathcal{Y}^J_{\epsilon_b \kappa_b; \epsilon_a \kappa_a} \right]^2 \right\}, \tag{1.1.100b}$$

Therefore, the quantity (1.1.99) is given by

$$\mathcal{G}_{ba} = \sum_J \left\{ \left[{}^{\mathrm{e}}\mathcal{Y}^J_{\epsilon_b \kappa_b; \epsilon_a \kappa_a} \right]^2 + \left[{}^{\mathrm{m}}\mathcal{Y}^J_{\epsilon_b \kappa_b; \epsilon_a \kappa_a} \right]^2 \right\} . \tag{1.1.101}$$

1.1.7 Cross sections of closed subshells

In practice, target atoms are randomly oriented and the measurable quantity is the cross section for photoabsorption by the electrons of a subshell $(n_a \kappa_a)^{q_a}$ with q_a electrons. Calculations are easier in the case of closed subshells, with $q_a = 2|\kappa_a|$ electrons, because of various sum rules obeyed by the angular integrals in transition matrix elements. For open subshells, with $q_a < 2|\kappa_a|$, the average over atomic orientations is equivalent to assuming that the individual orbitals in the subshell have a fractional occupation number equal to $q_a/2|\kappa_a|$; the resulting partial cross section is then equal to that of the closed subshell times $q_a/2|\kappa_a|$.

In the case of excitation, the measured cross section includes transitions to any state of the final energy level ϵ_b. Generally, the final level is empty ($q_b = 0$), although occasionally it may correspond to an open subshell $(n_b \kappa_b)^{q_b}$ filled with q_b ($0 < q_b < 2|\kappa_b|$) electrons. Hence, the cross section for one-electron excitation from the subshell $(n_a \kappa_a)^{q_a}$ to a bound level ϵ_b by absorption of a photon of polarization $\boldsymbol{\zeta}$ is given by

$$\begin{aligned} \sigma^{\mathrm{exc}}_{ba}(W) &= \frac{q_a}{2|\kappa_a|} \, \frac{2|\kappa_b| - q_b}{2|\kappa_b|} \sum_{m_a} \sum_{m_b} \sigma^{\mathrm{exc,1}}_{n_b \kappa_b m_b; n_a \kappa_a m_a}(W, \boldsymbol{\zeta}) \\ &= \overline{\sigma}^{\mathrm{exc}}_{n_b \kappa_b; a}(W) \, \delta(\epsilon_b - \epsilon_a - W) \end{aligned} \tag{1.1.102}$$

where it is introduced the “reduced” cross section, $\overline{\sigma}_{ba}^{\rm exc}(W)$, defined by

$$\overline{\sigma}_{n_b\kappa_b;a}^{\rm exc}(W) = \frac{(2\pi)^2 e^2 c\hbar}{W}\,\frac{q_a}{2|\kappa_a|}\,\frac{2|\kappa_b| - q_b}{2|\kappa_b|}\,\mathcal{G}^{\rm exc}(\kappa_b,\kappa_a)\,, \tag{1.1.103}$$

where

$$\begin{aligned}\mathcal{G}^{\rm exc}(\kappa_b,\kappa_a) &= \sum_{m_a}\sum_{m_b}\left|M^{\rm exc}_{n_b\kappa_b m_b;n_a\kappa_a m_a}(W,\boldsymbol{\zeta})\right|^2\\ &= \sum_{m_a}\sum_{m_b}\left|\sum_{\nu=\pm1}(-1)^\nu\zeta_\nu G^{\rm exc}_{-\nu}(\kappa_b,m_b;\kappa_a,m_a)\right|^2\end{aligned} \tag{1.1.104}$$

is the sum of squared transition-matrix elements over orbitals of the initial and final energy levels, which is given by Eq. (1.1.101),

$$\mathcal{G}^{\rm exc}(\kappa_b,\kappa_a) = \sum_J\left\{\left[{}^{\rm e}\mathcal{Y}^J_{n_b\kappa_b;\epsilon_a\kappa_a}\right]^2 + \left[{}^{\rm m}\mathcal{Y}^J_{n_b\kappa_b;\epsilon_a\kappa_a}\right]^2\right\}\,. \tag{1.1.105}$$

The quantities ${}^{\rm e,m}\mathcal{Y}^J_{n_b\kappa_b;\epsilon_a\kappa_a}$ are defined by Eqs. (1.1.97) with radial integrals ${}^{\rm m}\mathcal{R}^J_{n_b\kappa_b;\epsilon_a\kappa_a}$ evaluated for the final bound orbital $\psi_{n_b\kappa_b m_b}$. Note that the reduced cross section (1.1.103) is independent of the polarization of the absorbed photon. Naturally, this result is a direct consequence of the spherical symmetry of closed subshells.

Let us now consider the observed DCS for ionization of a subshell $(n_a\kappa_a)^{q_a}$. In addition to the assumption that the target atom is randomly oriented, it is supposed that the final spin state of the emitted photoelectron is not measured. The observed DCS is thus obtained by summing over degenerate initial states and over final spin states, $m_{{\rm S}b}$.

$$\frac{{\rm d}\sigma_a^{\rm ion}(W,\boldsymbol{\zeta})}{{\rm d}\hat{\mathbf{k}}_b} = \frac{(2\pi)^2 e^2}{W}\,\frac{k_b(\epsilon_b + {\rm m_e}c^2)}{c\hbar}\,\frac{q_a}{2|\kappa_a|}\sum_{m_a}\sum_{m_{{\rm S}b}}\left|M^{\rm ion}_{b;n_a\kappa_a m_a}(W,\boldsymbol{\zeta})\right|^2\,. \tag{1.1.106}$$

Inserting the expansion (1.1.90):

$$\begin{aligned}\frac{{\rm d}\sigma_a^{\rm ion}(W,\boldsymbol{\zeta})}{{\rm d}\hat{\mathbf{k}}_b} &= \frac{(2\pi)^2 e^2 c\hbar}{W}\,\frac{k_b}{\pi\epsilon_b}\,\frac{q_a}{2|\kappa_a|}\sum_{m_a}\left\{\sum_{\kappa_b',m_b'}{\rm i}^{-\ell_b'}\,\exp\left({\rm i}\delta_{\kappa_b'}\right)\boldsymbol{\zeta}\cdot\mathbf{G}^{\rm ion}(\kappa_b',m_b';\kappa_a,m_a)\right\}^*\\ &\quad\times\left\{\sum_{\kappa_b,m_b}{\rm i}^{-\ell_b}\,\exp\left({\rm i}\delta_{\kappa_b}\right)\boldsymbol{\zeta}\cdot\mathbf{G}^{\rm ion}(\kappa_b,m_b;\kappa_a,m_a)\right\}\\ &\quad\times\Omega^\dagger_{\kappa_b'm_b'}(\hat{\mathbf{k}}_b)\left[\sum_{m_{{\rm S}b}}\chi_{m_{{\rm S}b}}\chi^\dagger_{m_{{\rm S}b}}\right]\Omega_{\kappa_b m_b}(\hat{\mathbf{k}}_b)\,,\end{aligned} \tag{1.1.107}$$

where the sum in square brackets is equal to the 2 × 2 unit matrix. The total cross section for ionization of the subshell $(n_a\kappa_a)^{q_a}$ is obtained by integrating the DCS over the directions of the emerging photoelectron,

$$\sigma_a^{\mathrm{ion}}(W) = \int \frac{\mathrm{d}\sigma_a^{\mathrm{ion}}(W,\boldsymbol{\zeta})}{\mathrm{d}\hat{\mathbf{k}}_b}\,\mathrm{d}\hat{\mathbf{k}}_b\,. \tag{1.1.108}$$

Using the orthogonality of the spherical spinors, $\Omega_{\kappa_b m_b}(\hat{\mathbf{k}}_b)$, it is obtained

$$\sigma_a^{\mathrm{ion}}(W) = \frac{(2\pi)^2 e^2 c\hbar}{W}\,\frac{k_b}{\pi\epsilon_b}\,\frac{q_a}{2|\kappa_a|}\sum_{\kappa_b}\mathcal{G}^{\mathrm{ion}}(\kappa_b,\kappa_a)\,, \tag{1.1.109}$$

where

$$\begin{aligned}
\mathcal{G}^{\mathrm{ion}}(\kappa_b,\kappa_a) &= \sum_{m_a}\sum_{m_b}\left|\boldsymbol{\zeta}\cdot\mathbf{G}^{\mathrm{ion}}(\kappa_b m_b;\kappa_a m_a)\right|^2 \\
&= \sum_{m_a,m_b}\left|\sum_{\nu=\pm1}(-1)^\nu\zeta_{-\nu}G_\nu^{\mathrm{ion}}(\kappa_b,m_b;\kappa_a,m_a)\right|^2
\end{aligned} \tag{1.1.110}$$

is the sum of squared transition-matrix elements over the orbitals of the active subshell and over the spherical waves with the final energy, which is given by Eq. (1.1.101),

$$\mathcal{G}^{\mathrm{ion}}(\kappa_b,\kappa_a) = \sum_J\left\{\left[{}^{\mathrm{e}}\mathcal{Y}^J_{\epsilon_b\kappa_b;\epsilon_a\kappa_a}\right]^2 + \left[{}^{\mathrm{m}}\mathcal{Y}^J_{\epsilon_b\kappa_b;\epsilon_a\kappa_a}\right]^2\right\}, \tag{1.1.111}$$

with the quantities ${}^{\mathrm{e,m}}\mathcal{Y}^J_{n_b\kappa_b;\epsilon_a\kappa_a}$ defined by Eqs. (1.1.97). We see that, as in the case of excitation, the total cross section is independent of the polarization of the absorbed photon.

1.1.8 The dipole approximation

The calculation of cross sections for both excitation and ionization by photons with low energies, such that the wavelength $\lambda = 2\pi/k$ is much larger than the average radial distance of the electrons in the active subshell, can be simplified by using the dipole approximation. In this approximation, the quantity $\mathbf{k}\cdot\mathbf{r}$ is assumed to be much less than unity, and the exponential in the matrix elements (1.1.85) and (1.1.90) is replaced by unity,

$$\mathbf{G}^{\mathrm{dip}}(\kappa_b,m_b;\kappa_a,m_a) \simeq \langle\psi_{\epsilon_b\kappa_b m_b}|\,\widetilde{\boldsymbol{\alpha}}\,|\psi_{n_a\kappa_a m_a}\rangle\,. \tag{1.1.112}$$

Using the commutation relation of the Dirac Hamiltonian, Eq. (1.1.80), with $\mathbf{r}$,

$$[\mathcal{H},\mathbf{r}] = -\mathrm{i}\,c\hbar\,\widetilde{\boldsymbol{\alpha}}\,, \tag{1.1.113}$$

we get the familiar "length" form of the matrix elements in the dipole approximation,

$$\mathbf{G}^{\mathrm{dip}}(\kappa_b,m_b;\kappa_a,m_a) = \frac{\mathrm{i}}{c\hbar}\,W\,\langle\psi_{\epsilon_b\kappa_b m_b}|\,\mathbf{r}\,|\psi_{n_a\kappa_a m_a}\rangle\,. \tag{1.1.114}$$

Recalling that the spherical components of the vector $\mathbf{r}$ are $r_\nu = rC_{1,\nu}(\hat{\mathbf{r}})$, the angular integrals of these matrix elements reduce to matrix elements of the Racah tensors. We have

$$G_\nu^{\rm dip}(\kappa_b, m_b; \kappa_a, m_a) = \frac{\rm i}{c\hbar}\, W\, \langle \Omega_{\kappa_b,m_b} | C_{1,\nu} | \Omega_{\kappa_a,m_a} \rangle\, \mathcal{D}_{\epsilon_b\kappa_b;\epsilon_a\kappa_a} \tag{1.1.115}$$

with the radial integrals

$$\mathcal{D}_{\epsilon_b\kappa_b;\epsilon_a\kappa_a} = \int_0^\infty [P_{\epsilon_b\kappa_b}(r)\, P_{\epsilon_a\kappa_a}(r) + Q_{\epsilon_b\kappa_b}(r)\, Q_{\epsilon_a\kappa_a}(r)]\, r\, {\rm d}r. \tag{1.1.116}$$

Within the dipole approximation, the quantities (1.1.105) and (1.1.111) reduce to

$$\begin{aligned} \mathcal{G}^{\rm dip}(\kappa_b, \kappa_a) &= \sum_{m_a}\sum_{m_b} \left| \sum_{\nu=\pm1} (-1)^\nu \zeta_\nu\, G_{-\nu}^{\rm dip}(\kappa_b, m_b; \kappa_a, m_a) \right|^2 \\ &= \frac{W^2}{3(c\hbar)^2} \left\langle \ell_b \tfrac{1}{2} j_b \left\| \mathbf{C}^{(1)} \right\| \ell_a \tfrac{1}{2} j_a \right\rangle^2 [\mathcal{D}_{\epsilon_b,\kappa_b;\epsilon_a,\kappa_a}]^2 \,. \end{aligned} \tag{1.1.117}$$

Although the dipole approximation yields realistic values of the total cross section for long-wavelength photons (see Section 1.3), the DCS (*i.e.*, the angular distribution of photoelectrons) obtained from this approximation is qualitatively correct only for photon energies near the ionization threshold (see Fig. 1.5).

1.1.9 Near-edge excitation cross section

Because of memory and time constraints, our computer program PHOTACS calculates reduced excitation cross sections, $\overline{\sigma}^{\rm exc}_{n_b\kappa_b;a}(W)$, for bound levels with principal quantum number n_b up to $n_{\rm cut} = 18$. The numerical value of the quantity $\mathcal{G}^{\rm dip}(\kappa_b, \kappa_a)$, Eq. (1.1.117), qualifies the levels $\epsilon_{n_b\kappa_b}$. Cross sections of dipole-forbidden levels [with $\mathcal{G}^{\rm dip}(\kappa_b, \kappa_a) = 0$] have values that are typically several orders of magnitude smaller than those of dipole-allowed levels [with $\mathcal{G}^{\rm dip}(\kappa_b, \kappa_a) \neq 0$]. To reduce the size of the tables, and to simplify further calculations, PHOTACS delivers cross-section values only for excitations to dipole-allowed levels. Cross sections for transitions to dipole-forbidden levels are calculated and added to the cross section of the nearest dipole-allowed level. In other words, the reduced cross section $\overline{\sigma}^{\rm exc}_{n_b\kappa_b;a}(W)$ given by the program is the cross section of the allowed level $\epsilon_{n_b\kappa_b}$ plus small contributions of excitations to neighbouring forbidden levels.

For a given value of κ_b, there exists an infinite series of bound levels $\epsilon_{n_b\kappa_b}$, whose energies increase monotonically with the principal quantum number n_b and have an accumulation point at zero energy. To account for the cross sections for excitation to levels with n_b larger than 18, it is possible to rely on the fact that, regarding the bound levels with energies close to zero as a quasi-continuum, the cross section for excitation continuously joins the ionization cross section at the edge, $W = E_a$ (see, *e.g.*, Refs.

[57] and [58]). Explicitly, from the cross sections for excitation to the levels $\epsilon_{n_b\kappa_b}$, it is defined the following step function

$$S_a(\kappa_b;W) = \frac{\overline{\sigma}^{\rm exc}_{n_b\kappa_b;a}(W)}{\epsilon_{n_b}-\epsilon_{n_b-1}} \qquad \text{if} \qquad \epsilon_{n_b-1}-\epsilon_a < W \le \epsilon_{n_b}-\epsilon_a, \tag{1.1.118}$$

where ϵ_{n_b} are the midpoints of the energy intervals between successive energy levels,

$$\epsilon_{n_b} = \frac{\epsilon_{n_b\kappa_b}+\epsilon_{n_b+1,\kappa_b}}{2}\,. \tag{1.1.119}$$

That is, the excitation cross section is spread over the energy interval that is closest to the final level. Numerical results confirm that the step function $S_a(\kappa_b;W)$ does smoothly join the ionization cross section at the edge (see Fig. 1.3 below). The smooth matching of the discrete and the continuum is due to the fact that, for a given angular momentum κ_b and for not too large radii, the radial functions of bound orbitals with very large n_b differ from those of free orbitals with very small kinetic energies only by a normalization factor. When free-state orbitals are normalized on the energy scale,

$$\int \psi^\dagger_{\epsilon'\kappa'm'}\,\psi_{\epsilon\kappa m}\,{\rm d}\mathbf{r} = \delta(\epsilon'-\epsilon)\,\delta_{\kappa'\kappa}\,\delta_{m'm}\,, \tag{1.1.120}$$

and bound orbitals are normalized to unity, Eq. (1.1.20), the radial functions of bound and free states with energies close to zero are such that

$$\left(\frac{P_{\epsilon_b\kappa_b}(r)}{P_{n_b\kappa_b}(r)}\right)^2 = \frac{1}{\epsilon_{n_b}-\epsilon_{n_b-1}} \tag{1.1.121}$$

for sufficiently small radii r, large n_b, and small ϵ_b. This quantity, which coincides with the “spread factor” in the definition (1.1.118), can be regarded as the number of discrete levels per unit energy interval, the analogue to the density of states of the continuum.

In calculations of excitation to bound levels each series of (optically-allowed) levels $\epsilon_{n_b\kappa_b}$, with κ_b fixed is considered separately. Let $n_0(\kappa_b)$ denote the principal quantum number of the first level in the series. We describe the first three levels in the series [with $n_b = n_0(\kappa_b), n_0(\kappa_b)+1, n_0(\kappa_b)+2$] as discrete resonances. The levels with $n_b > n_0(\kappa_b)+2$ are treated as a quasi-continuum, which extends from a certain cut-off energy $W^{\rm cut}_{a\kappa_b}$ to $W = E_a$, with the excitation cross section expressed as a cubic polynomial in $E_a - W$,

$$\overline{\sigma}^{\rm exc}_a(\kappa_b;W) = A_{\kappa_b,0} + A_{\kappa_b,1}(E_a-W) + A_{\kappa_b,2}(E_a-W)^2 + A_{\kappa_b,3}(E_a-W)^3. \tag{1.1.122}$$

The coefficients of this polynomial are determined from a least-squares fit to a table of values of the step function (1.1.118) at the excitation energies of the levels, $\{\epsilon_{n_b\kappa_b}, S_a(\kappa_b;\epsilon_{n_b\kappa_b}-\epsilon_a)\}$ with $n_b = n_0(\kappa_b)+3$ to 18. The cut-off energy $W^{\rm cut}_{a\kappa_b}$ is fixed so that the integral of the analytical approximation (1.1.122) over W in the interval from $W^{\rm cut}_{a\kappa_b}$ to the upper limit of the subinterval of the $n_b = 18$ level, equals the sum of excitation cross sections of the levels $\epsilon_{n_b\kappa_b}$ with $n_b = n_0(\kappa_b)+3$ to 18. We assume that this polynomial represents the quasi-continuum faithfully and, hence, that it does account for excitations to levels with n_b greater than 18. These considerations can be verified numerically using our computer programs. A graphical analysis of the case of excitations from the K shell of argon atoms is given below in Fig. 1.3.

Note that pseudo-continua of series with different κ_b extend over different intervals. The cross section for excitations to bound levels is then given by

$$\begin{aligned}\sigma_a^{\rm exc}(W) &= \sum_{n_b\kappa_b} \overline{\sigma}^{\rm exc}_{n_b\kappa_b;a}(W)\,\delta(\epsilon_b-\epsilon_a-W)\\ &\quad+\sum_{\kappa_b}\overline{\sigma}_a^{\rm exc}(\kappa_b;W)\,\Theta(W-W^{\rm cut}_{a\kappa_b})\,\Theta(E_a-W)\,, \end{aligned} \tag{1.1.123}$$

where $\Theta(x)$ is the unit step function ($=1$ if $x\geq 0$, $=0$ otherwise). The first summation is over discrete resonances (excitations to the three lowest levels of each κ_b series), and the second summation accounts for excitations to levels in the pseudo-continua.

1.1.10 Ionization cross sections at high energies

The convergence rate of the series (1.1.109) decreases when the energy of the photon increases. Therefore, the program PHOTACS is able to compute the ionization cross section $\sigma_a^{\rm ion}(W)$ for photons with energy W up to a certain maximum value $W_a^{\rm cut}$. Cross sections for photons with energies higher than $W_a^{\rm cut}$ can be obtained by extrapolating the calculated numerical cross sections using the approximate formula given by Pratt [18] (see also Ref. [6]) for K-shell electrons, which combines Pratt's high-energy limit with the general energy dependence determined by Gavrila [59]. The formula for the cross section per electron in the K shell of an atom of atomic number Z reads

$$\begin{aligned}\sigma_{\rm K}^{\rm Pratt}(W) &= \sigma_0\,\frac{(\beta\gamma)^3}{(W/{\rm m_e}c^2)^4}\,\frac{\exp[-2(a/\beta)\arccos a]}{a^{2\xi}}\\ &\qquad\times M(\beta)\,\{1+\pi a[N(\beta)/M(\beta)]+R(a)\}\,, \end{aligned} \tag{1.1.124}$$

where $a=Z\alpha$ [$\alpha=e^2/(c\hbar)\simeq 1/137$ is the fine-structure constant], $\xi=1-\sqrt{1-a^2}$, β is the velocity of the photoelectron in units of c,

$$\beta=\sqrt{\frac{(W-E_a)(W-E_a+2{\rm m_e}c^2)}{(W-E_a+{\rm m_e}c^2)^2}}\,, \tag{1.1.125}$$

and

$$\gamma\equiv\sqrt{\frac{1}{1-\beta^2}}=1+\frac{W-E_a}{{\rm m_e}c^2}. \tag{1.1.126}$$

The quantity σ_0 is the high-energy cross section per electron, given by

$$\sigma_0=2\pi a_0^2\,a^5\alpha^3\,\frac{{\rm m_e}c^2}{W}\,. \tag{1.1.127}$$

The functions $M(\beta)$ and $N(\beta)$ are defined by

$$M(\beta) = \frac{4}{3} + \frac{\gamma(\gamma-2)}{\gamma+1}\left[1 - \frac{1}{2\gamma\sqrt{\gamma^2-1}}\ln\left(\frac{\gamma+\sqrt{\gamma^2-1}}{\gamma-\sqrt{\gamma^2-1}}\right)\right], \tag{1.1.128}$$

and

$$N(\beta) = \frac{1}{15\beta^3}\left[-4\gamma + 34 - \frac{63}{\gamma} + \frac{25}{\gamma^2} + \frac{8}{\gamma^3} + \frac{15(\gamma^2-3\gamma+2)}{2\beta\gamma^3}\ln\left(\frac{1-\beta}{1+\beta}\right)\right]. \tag{1.1.129}$$

Finally, the quantity $R(a)$ is defined so as to reproduce Pratt's high-energy limit of the total cross section (per electron) for the photoeffect in the K shell, which is given by [18, 6]

$$\lim_{W\to\infty}\sigma_{\mathrm{K}}(W) = \sigma_0 F(a) \tag{1.1.130}$$

with

$$\begin{aligned} F(a) \;=\; & \frac{3-2\xi}{2\xi}\,a^{-2\xi}\frac{1}{4}\int_{-1}^{1}\mathrm{d}x\int_{-1}^{1}\mathrm{d}y\left(\frac{1-x}{1+x}\right)^{\mathrm{i}a}\left[a+\mathrm{i}\sqrt{1-a^2}\,x\right]^{-4+2\xi} \\ & \times\left\{(1-x^2y^2)^{1-\xi}\left[1+\left(\frac{\xi}{a}\right)^2\right]\right. \\ & \qquad \left. -2(1-y^2)\,(1-x^2y^2)^{-\xi}\left[\mathrm{i}\,\frac{\xi}{a}\,x + \left(\frac{\xi}{a}\right)^2 x^2\right]\right\}. \end{aligned} \tag{1.1.131}$$

Consistency of Eq. (1.1.124) with this high-energy limit implies that

$$F(a) = \frac{\exp(-2a\cos^{-1}a)}{a^{2\xi}}\left[1 - \frac{4\pi}{15}\,a + R(a)\right]. \tag{1.1.132}$$

Values of the function $F(a)$ calculated numerically by Pratt, with an estimated accuracy of 0.1 %, are given in Table I of Ref. [18]. Numerical values of $R(a)$ are also given by Pratt *et al.* [6] in their Table 6.1. Unfortunately, the latter table contains several erroneous signs. To determine an accurate analytical approximation to $R(a)$, it is calculated the function $F(a)$ for a dense grid of a values by computing the double integral (1.1.131) using an adaptive Gauss-Legendre quadrature method, which allows control of numerical errors, to an accuracy of about 10^{-7}. The calculated table extends from $a = 0.01$ to 0.8, corresponding to Z up to 109, and agrees with Pratt's values [18] within the claimed accuracy of the latter. A least-squares fit of our tabulated values leads to the approximation

$$R(a) = 0.00372a - 0.16326a^2 + 0.94375a^3 - 0.71732a^4, \tag{1.1.133}$$

which, when inserted into expression (1.1.132), approximates the numerical values of $F(a)$ with relative error less than 0.01 %.

As indicated by Pratt *et al.* [6] the ratios of cross sections of different subshells are nearly energy independent. Hence, although the formula (1.1.124) was derived for the K shell, it can be employed to extrapolate the DHFS cross sections of other subshells for energies above their numerical cut-off $W_a^{\rm cut}$. In this calculations it was setted

$$\sigma_a^{\rm ion}(W) = \frac{\sigma_a^{\rm ion}(W_a^{\rm cut})}{\sigma_{\rm K}^{\rm Pratt}(W_a^{\rm cut})}\, \sigma_{\rm K}^{\rm Pratt}(W) \tag{1.1.134}$$

for $W > W_a^{\rm cut}$. In practice, this extrapolation scheme works very well for inner subshells with binding energies larger than about 100 eV, for which the extrapolation matches the numerical cross sections in a wide energy interval, and not so well for outer shells with $E_a \lesssim 100$ eV because the slopes of the numerical and the extrapolation curves at $W = W_a^{\rm cut}$ are slightly different. However, the relative contributions of the outer subshells are less than about 10^{-5} and, consequently, the error introduced by the extrapolation has no practical effects. A similar extrapolation method was employed by Hubbell *et al.* [60], and also by Cullen *et al.* [14], who used a semiempirical formula that reproduces Pratt's high-energy values for the K shell.

1.1.11 Finite level widths and experimental ionization energies

Up to this point it was assumed that excited states are stationary. This assumption leads to the delusive delta function in the excitation cross section, Eq. (1.1.102). In reality, excited states decay by radiative and non-radiative transitions and, consequently, have a finite mean life τ_b and a natural level width $\Gamma_b = \hbar/\tau_b$. Assuming that excited estates decay exponentially with time, it is concluded that absorption lines have a Lorentz profile centred at the resonance energy, with full width at half-maximum equal to Γ_b (see, *e.g.*, Ref. [61]). Consequently, results from measurements of the energy E of an excited level ϵ_b are expected to follow the Lorentz distribution

$$L(\Gamma_b; \epsilon_b - E) = \frac{1}{\pi} \frac{(\Gamma_b/2)}{(\epsilon_b - E)^2 + (\Gamma_b/2)^2}\,. \tag{1.1.135}$$

In addition, the cross section for excitation of an electron from the level ϵ_a (corresponding to the ground state) to a level ϵ_b by absorption of photons with energy W should be calculated as the integral over the continuous level profile,

$$\begin{aligned} \sigma_{ba}^{\rm exc}(W) &= \int_0^\infty \overline{\sigma}_{n_b\kappa_b;a}^{\rm exc}(W)\, \delta(E - \epsilon_a - W)\, L(\Gamma_b; \epsilon_b - E)\, {\rm d}E \\ &= \overline{\sigma}_{n_b\kappa_b;a}^{\rm exc}(W)\, L(\Gamma_b; \epsilon_b - \epsilon_a - W)\,. \end{aligned} \tag{1.1.136}$$

This result differs from the expression (1.1.102) for stationary levels only in that the Lorentz distribution replaces the delta resonance.

As noted by Ritchmyer *et al.* [62], in the case of excitations that produce a single vacancy in an inner subshell $(n_a\kappa_a)$, the first stage of the subsequent decay of the atom is the filling of that vacancy by electrons from nearest subshells, a process practically independent of the condition of the excited electron. Consequently, all excited levels with a vacancy in subshell $(n_a\kappa_a)$ have approximately the same level width, Γ_a, the so-called "core-level width". Calculated values of core-level widths of free atoms are given in the EADL [63]. Campbell and Papp [64] give a complete set of recommended widths for K to N7 levels of atoms obtained from consideration of available experimental data. Typically, the core-level widths increase with the binding energy of the subshell, and are of the order of 0.1 eV or less for weakly bound subshells, and reach values of the order of 100 eV for K shells of transuranic elements.

Assuming that the level width is a characteristic of the active subshell $(n_a\kappa_a)^{q_a}$ where the vacancy is created, its influence on the photoeffect can be accounted for by convolving the calculated cross section with the Lorentzian distribution (1.1.135). That is to say [cf. Eq. (1.1.123)],

$$\begin{aligned}\sigma_a(W) \;=\; & \sum_{n_b,\kappa_b} \overline{\sigma}^{\rm exc}_{n_b\kappa_b;a}(W)\, L(\Gamma_a;\epsilon_b-\epsilon_a-W)\\ & + \sum_{\kappa_b}\int_{W^{\rm cut}_{a\kappa_b}}^{E_a} \overline{\sigma}^{\rm exc}_a(\kappa_b;E)\, L(\Gamma_a;E-W)\,{\rm d}E\\ & + \int_{E_a}^{\infty} \sigma^{\rm ion}_a(E)\, L(\Gamma_a;E-W)\,{\rm d}E \end{aligned} \qquad (1.1.137)$$

where again, the first summation is over discrete resonances with excitation energies less than the corresponding cut-off $W^{\rm cut}_{a\kappa_b}$. The integrals of the second term on the right-hand side, with $\overline{\sigma}^{\rm exc}_a(\kappa_b;W)$ expressed by the polynomial approximation (1.1.122), can be evaluated analytically. The last term can be evaluated similarly when the ionization cross section $\sigma^{\rm ion}_a(W)$ is obtained from a pre-calculated table of values, at suitably spaced energies, by means of cubic spline interpolation.

There is a further empirical correction to be considered. Although the DHFS eigenvalues, E_a, are quite close to the experimental subshell ionization energies $E^{\rm exp}_a$ [65], the differences induce appreciable shifts of the absorption edges (typically, of a few eV). We can correct the calculated cross sections for this discrepancy, by simply shifting the energy scale and setting

$$\sigma^{\rm es}_a(W) = \sigma_a(W + E_a - E^{\rm exp}_a)\,. \qquad (1.1.138)$$

The cross sections given by this formula will be referred to as "energy-shifted cross sections". The post-processing program PHOTACS-PP (see below) allows this energy shift to be applied automatically. The default experimental ionization energies $E^{\rm exp}_a$ have been taken from the compilation of Carlson [66], which covers all the subshells of the elements from $Z = 1$ to 106. Alternatively, the program allows ionization energies to be used from the more updated compilation by Williams [67], which is mostly based on x-ray photoelectron measurements on samples prepared in ultra-high vacuum conditions.

1.1.12 Normalization screening approximation

A primary ingredient of the calculations is the DHFS potential, which provides only a rough approximation to the atomic wave functions. More elaborate atomic structure calculations employ the multi-configuration Dirac-Fock (MCDF) method [21]. Unfortunately, the theoretical scheme underlying this method does not permit easy calculation of photoelectric cross sections, because the MCDF equations involve a non-local potential that is different for each subshell.

A simple method for estimating how the use of more accurate wave functions would affect the cross section for the photoeffect is provided by Pratt's normalization screening approximation, which is presented in Ref. [68] and discussed in Refs. [19, 20, 6]. The key idea under this approximation is that, for photon energies a few keV above the ionization threshold, the dominant contributions to the transition matrix elements come from radial distances of the order of the reduced electron Compton wavelength, $\lambdabar_{\rm e} = \hbar/{\rm m_e}c = 3.8616 \times 10^{-13}$ m. In other words, from distances that are substantially larger than the radius of the nucleus but much smaller than the average radial distance of electrons in bound orbitals. At radii important for photoabsorption, the only effect of screening is a change in the normalization of bound states. It then follows that the photoelectric cross sections for the screened atomic potential (scr) and for the Coulomb potential of the bare nucleus (Coul) differ by an energy-independent factor,

$$\sigma_a^{\rm scr}(W) = \Xi_a^2 \, \sigma_a^{\rm Coul}(W) \,, \tag{1.1.139}$$

where Ξ_a^2 is the ratio of electron densities at $r = 0$. This ratio is determined by the normalization of the bound-state wave functions,

$$\Xi_a^2 = \lim_{r\to 0} \frac{[P^2_{n_a\kappa_a}(r) + Q^2_{n_a\kappa_a}(r)]_{\rm scr}}{[P^2_{n_a\kappa_a}(r) + Q^2_{n_a\kappa_a}(r)]_{\rm Coul}} = \left(\lim_{r\to 0} \frac{[P_{n_a\kappa_a}(r)]_{\rm scr}}{[P_{n_a\kappa_a}(r)]_{\rm Coul}} \right)^2 . \tag{1.1.140}$$

The accuracy of the normalization screening approximation can be practically assessed by running our program with the DHFS potential and with the (unscreened) Coulomb potential. It should be noted, however, that the proportionality (1.1.139) only holds when a point nucleus is considered in the DHFS calculation. Otherwise, the radial functions for the DHFS potential and for the Coulomb potential have different shapes, a fact that complicates the theoretical analysis. Indeed, the approximation is found to work very well for photons with energies larger than the DHFS ionization energies. We may expect that it will perform even better for "similar" screened potentials. Schmickley and Pratt [19] went a step further and suggested that the normalization screening approximation can be effectively employed to relate cross sections calculated with different atomic models. Scofield [7], more explicitly, stated that "the approximation probably holds for an atom as a whole, if the single-particle model is given up." Consistently, he calculates cross sections for all the elements with the DHFS potential and lists the normalization ratios Ξ_a^2 for orbitals obtained from the DHFS code and from restricted relativistic Hartree-Fock calculations for $Z = 1$ to 54.

Following Scofield, it is evaluated Ξ_a^2 for all subshells of the ground-state configuration of the elements $Z = 1$ to 99 using wave functions obtained from calculations with our DHFS program and with the MCDF program of Desclaux [21, 22]. The resulting density ratios for the K shell and the L, M and N subshells of the elements are represented in Fig. 1.1. Because density ratios are less than, and close to unity, the displayed quantity is the difference $1 - \Xi^2_{\mathrm{MCDF},a}/\Xi^2_{\mathrm{DHFS},a}$. We see that the effect of the normalization screening correction is a reduction of the cross section of the order of a few percent or less, except for outer subshells with small binding energies, where it can rise up to about 30 percent. Furthermore, the correction is larger for the outer subshells and, consequently, its effect is most visible for photons with relatively low energies. We can thus apply the normalization screening correction to the photoionization cross sections obtained from DHFS calculations,

$$\sigma_a^{\mathrm{scr}}(W) = \frac{\Xi^2_{\mathrm{MCDF},a}}{\Xi^2_{\mathrm{DHFS},a}}\, \sigma_a^{\mathrm{DHFS}}(W)\,, \tag{1.1.141}$$

to get better estimates of cross sections, whose accuracy is expected to be comparable to that of the MCDF model.

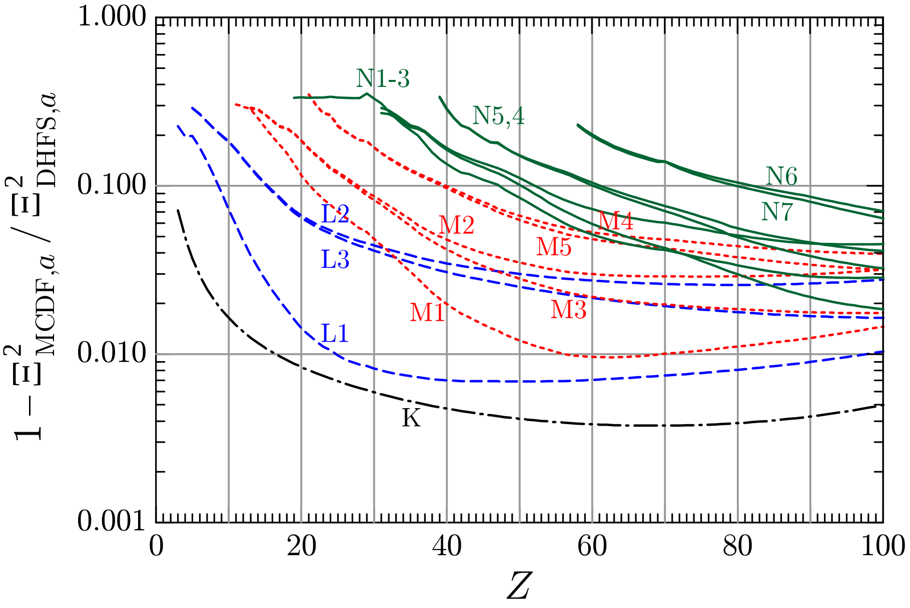

Figure 1.1: Relative reduction of the subshell cross sections introduced by the normalization screening correction, obtained from electron density ratios resulting from MCDF and DHFS self-consistent atomic calculations.

1.2 Angular distribution of photoelectrons

Although the polarization of the photon does not affect the total cross section, it does have an effect on the angular distribution of photoelectrons which, classically, accelerate in the direction of the electric field of the incident electromagnetic wave. The DCS for ionization, Eq. (1.1.107), can be expressed as

$$\frac{\mathrm{d}\sigma_a^{\mathrm{ion}}(W,\boldsymbol{\zeta})}{\mathrm{d}\hat{\mathbf{k}}_b} = \frac{(2\pi)^2 e^2 c\hbar}{W}\,\frac{k_b}{\pi\epsilon_b}\,\frac{q_a}{2|\kappa_a|}\sum_{m_a}\left[g_{\kappa_a m_a}(\boldsymbol{\zeta},\hat{\mathbf{k}}_b)\right]^{\dagger}\left[g_{\kappa_a m_a}(\boldsymbol{\zeta},\hat{\mathbf{k}}_b)\right], \tag{1.2.142}$$

where it is introduced the emission amplitude (spinor)

$$\begin{aligned} g_{\kappa_a m_a}(\boldsymbol{\zeta},\hat{\mathbf{k}}_b) &\equiv \sum_{\kappa_b m_b} \mathrm{i}^{-\ell_b}\,\exp\left(\mathrm{i}\delta_{\kappa_b}\right)\,\boldsymbol{\zeta}\cdot\mathbf{G}^{\mathrm{ion}}(\kappa_b,m_b;\kappa_a,m_a)\,\Omega_{\kappa_b m_b}(\hat{\mathbf{k}}_b) \\ &= \sum_{\kappa_b m_b} U_{\kappa_b,m_b;\kappa_a,m_a}\,\Omega_{\kappa_b m_b}(\hat{\mathbf{k}}_b), \end{aligned} \tag{1.2.143}$$

where

$$U_{\kappa_b,m_b;\kappa_a,m_a} = \mathrm{i}^{-\ell_b}\,\exp\left(\mathrm{i}\delta_{\kappa_b}\right)\left\{\sum_{\nu=\pm1}(-1)^{\nu}\zeta_{\nu}G^{\mathrm{ion}}_{-\nu}(\kappa_b,m_b;\kappa_a,m_a)\right\}. \tag{1.2.144}$$

and [see Eq. (1.1.98a)]

$$\begin{aligned} G^{\mathrm{ion}}_{\pm1}(\kappa_b m_b;\kappa_a m_a) &= (-1)^{j_a-m_a}\sum_{J=1}^{\infty}\mathrm{i}^J\,\langle j_a,j_b,m_a,-m_b|J,\mp1\rangle \\ &\qquad\times\left\{{}^{\mathrm{e}}\mathcal{Y}^{J}_{\epsilon_b\kappa_b;\epsilon_a\kappa_a} \pm \mathrm{i}\;{}^{\mathrm{m}}\mathcal{Y}^{J}_{\epsilon_b\kappa_b;\epsilon_a\kappa_a}\right\}, \end{aligned} \tag{1.2.145}$$

with [see Eqs. (1.1.97b) and (1.1.97c)]

$${}^{\mathrm{e}}\mathcal{Y}^{J}_{\epsilon_b\kappa_b;\epsilon_a\kappa_a} = \sqrt{\frac{2J+1}{2J(J+1)}}\,\left\langle \ell_b\tfrac{1}{2}j_b\left\|\mathbf{C}^{(L)}\right\|\ell_a\tfrac{1}{2}j_a\right\rangle{}^{\mathrm{e}}\mathcal{R}^{J}_{\epsilon_b\kappa_b;\epsilon_a\kappa_a}, \tag{1.2.146a}$$

$${}^{\mathrm{m}}\mathcal{Y}^{J}_{\epsilon_b\kappa_b;\epsilon_a\kappa_a} = \sqrt{\frac{2J+1}{2J(J+1)}}\,\left\langle \ell_b\tfrac{1}{2}j_b\left\|\mathbf{C}^{(L)}\right\|\bar{\ell}_a\tfrac{1}{2}j_a\right\rangle{}^{\mathrm{m}}\mathcal{R}^{J}_{\epsilon_b\kappa_b;\epsilon_a\kappa_a}. \tag{1.2.146b}$$

The value of the component G^{ion}_0 is irrelevant here because the polarization vector is on the x-y plane, *i.e.*, $\zeta_0 = 0$.

Evidently, the DCS (1.2.142) is more difficult to compute than the total cross section, Eq. (1.1.109), because of the dependence of the emission amplitude on the magnetic quantum numbers of the initial and final states. As it will be seen, the DCS can be effectively computed from Eq. (1.2.142). Of course, the resulting DCS is consistent with the total cross section (1.1.109), that is, when the emission amplitude is calculated using the same number of κ_b terms as in expression (1.1.109), numerical evaluation of the integral (1.1.108) should yield the same result as Eq. (1.1.109).

To obtain a more explicit expansion of the DCS in terms of Legendre functions (similar, *e.g.*, to that derived by Scofield [69] for linearly polarized photons), it is introduced the expression (1.1.14) of the spherical spinors, and make use of the orthogonality of the unit spinors χ_μ, to write

$$\begin{aligned}\frac{\mathrm{d}\sigma_a^{\mathrm{ion}}(W,\boldsymbol{\zeta})}{\mathrm{d}\hat{\mathbf{k}}_b} &= \frac{(2\pi)^2 e^2 c\hbar}{W}\,\frac{k_b}{\pi\epsilon_b}\,\frac{q_a}{2|\kappa_a|}\sum_{m_a}\sum_{\nu\nu'}(-1)^{\nu+\nu'}\zeta_\nu\zeta^*_{\nu'}\sum_{\mu}\\ &\times\sum_{\kappa_b\kappa'_b}\mathrm{i}^{\ell'_b-\ell_b}\exp\left[\mathrm{i}\left(\delta_{\kappa_b}-\delta_{\kappa'_b}\right)\right]\sum_{m_b m'_b}G_{-\nu}(\kappa_b,m_b;\kappa_a,m_a)\,G^*_{-\nu'}\left(\kappa'_b,m'_b;\kappa_a,m_a\right)\\ &\times\langle\ell_b,\tfrac{1}{2},m_b-\mu,\mu|j_b,m_b\rangle\langle\ell'_b,\tfrac{1}{2},m'_b-\mu,\mu|j'_b,m'_b\rangle\;Y_{\ell_b,m_b-\mu}(\hat{\mathbf{k}}_b)Y^*_{\ell'_b,m'_b-\mu}(\hat{\mathbf{k}}_b)\,.\end{aligned}$$

Introducing the Clebsch-Gordan series for the spherical harmonics, and after rather lengthy transformations using conventional angular momentum recoupling algebra [38, 41, 39], the DCS can be written in the form (cf. Ref. [69])

$$\frac{\mathrm{d}\sigma_a^{\mathrm{ion}}(W,\boldsymbol{\zeta})}{\mathrm{d}\hat{\mathbf{k}}_b} = \frac{(2\pi)^2 e^2 c\hbar}{W}\,\frac{k_b}{\pi\epsilon_b}\,\frac{q_a}{2|\kappa_a|}\sum_{\nu\nu'}\zeta_\nu\zeta^*_{\nu'}\sum_{\ell}A^{\ell}_{\nu\nu'}\;Y_{\ell,\nu'-\nu}(\hat{\mathbf{k}}_b) \tag{1.2.147}$$

with

$$\begin{aligned}A^{\ell}_{\nu\nu'} &= (-1)^{\ell+\nu'}\sqrt{\frac{2\ell+1}{4\pi}}\sum_{\kappa_b,J,\kappa'_b,J'}(-1)^{j_a+j_b+j'_b+1/2}\\ &\times\sqrt{(2j_b+1)\,(2j'_b+1)\,(2\ell_b+1)\,(2\ell'_b+1)\,(2J+1)\,(2J'+1)}\\ &\times\begin{pmatrix}\ell_b & \ell'_b & \ell\\ 0 & 0 & 0\end{pmatrix}\begin{Bmatrix}j'_b & j_b & \ell\\ \ell_b & \ell'_b & \frac{1}{2}\end{Bmatrix}\begin{Bmatrix}J & J' & \ell\\ j'_b & j_b & j_a\end{Bmatrix}\\ &\times\begin{pmatrix}J & J' & \ell\\ \nu & -\nu' & \nu'-\nu\end{pmatrix}\mathrm{i}^{\ell'_b-\ell_b+J-J'}\exp\left[\mathrm{i}\left(\delta_{\kappa_b}-\delta_{\kappa'_b}\right)\right]\\ &\times\left\{{}^{\mathrm{e}}\mathcal{Y}^{J}_{\epsilon_b\kappa_b;\epsilon_a\kappa_a}-\mathrm{i}\,\nu\;{}^{\mathrm{m}}\mathcal{Y}^{J}_{\epsilon_b\kappa_b;\epsilon_a\kappa_a}\right\}\left\{{}^{\mathrm{e}}\mathcal{Y}^{J'}_{\epsilon_b\kappa'_b;\epsilon_a\kappa_a}+\mathrm{i}\,\nu'\;{}^{\mathrm{m}}\mathcal{Y}^{J'}_{\epsilon_b\kappa'_b;\epsilon_a\kappa_a}\right\},\end{aligned} \tag{1.2.148}$$

where (:::) and {:::} are, respectively, Wigner's $3j$ and $6j$ symbols, [38, 41, 39]. A convenient simplification is obtained by using the formula

$$\upsilon(\ell,\ell_b,\ell'_b)\begin{pmatrix}\ell & j_b & j'_b\\ 0 & \frac{1}{2} & -\frac{1}{2}\end{pmatrix} = -\sqrt{(2\ell_b+1)(2\ell'_b+1)}\begin{pmatrix}\ell_b & \ell'_b & \ell\\ 0 & 0 & 0\end{pmatrix}\begin{Bmatrix}j'_b & j_b & \ell\\ \ell_b & \ell'_b & \frac{1}{2}\end{Bmatrix}, \tag{1.2.149}$$

where $\upsilon(\ell, \ell_b, \ell'_b)$ is the parity factor (1.1.30). Noting that $(-1)^{\nu'} = -1$, and considering the symmetry of the $3j$ symbols, we get

$$\begin{aligned} A^{\ell}_{\nu\nu'} &= (-1)^{j_a+1/2}\sqrt{\frac{2\ell+1}{4\pi}} \sum_{\kappa_b, J, \kappa'_b, J'} \sqrt{(2j_b+1)\,(2j'_b+1)\,(2J+1)\,(2J'+1)} \\ &\quad \times \upsilon(\ell, \ell_b, \ell'_b) \begin{pmatrix} \ell & j_b & j'_b \\ 0 & -\frac{1}{2} & \frac{1}{2} \end{pmatrix} \begin{Bmatrix} J & J' & \ell \\ j'_b & j_b & j_a \end{Bmatrix} \\ &\quad \times \begin{pmatrix} J & J' & \ell \\ \nu & -\nu' & \nu'-\nu \end{pmatrix} \mathrm{i}^{\ell'_b-\ell_b+J-J'} \exp\left[\mathrm{i}\left(\delta_{\kappa_b} - \delta_{\kappa'_b}\right)\right] \\ &\quad \times \left\{ {}^{\mathrm{e}}\mathcal{Y}^{J}_{\epsilon_b\kappa_b;\epsilon_a\kappa_a} - \mathrm{i}\,\nu\; {}^{\mathrm{m}}\mathcal{Y}^{J}_{\epsilon_b\kappa_b;\epsilon_a\kappa_a} \right\} \left\{ {}^{\mathrm{e}}\mathcal{Y}^{J'}_{\epsilon_b\kappa'_b;\epsilon_a\kappa_a} + \mathrm{i}\,\nu'\; {}^{\mathrm{m}}\mathcal{Y}^{J'}_{\epsilon_b\kappa'_b;\epsilon_a\kappa_a} \right\}. \end{aligned} \tag{1.2.150}$$

From the symmetry properties of the $3j$ and $6j$ symbols, it follows that

$$A^{\ell}_{\nu\nu'} = \left[A^{\ell}_{\nu'\nu}\right]^{*}. \tag{1.2.151}$$

In addition, because of the parity factor in the reduced matrix element of the Racah tensor, Eq. (1.1.29), the vector coupling coefficients in (1.2.150) have reinforced symmetries which imply that

$$A^{\ell}_{+1,+1} = A^{\ell}_{-1,-1} \quad \text{and} \quad A^{\ell}_{+1,-1} = A^{\ell}_{-1,+1}. \tag{1.2.152}$$

The right-hand side of Eq. (1.2.147) can be reduced further by expressing the spherical harmonics in terms of Legendre functions [41, 39]. We have

$$\begin{aligned} \sum_{\nu\nu'} \zeta_\nu \zeta^*_{\nu'} \sum_{\ell} A^{\ell}_{\nu\nu'}\, Y_{\ell,\nu-\nu'}(\hat{\mathbf{k}}_b) &= \sum_{\ell} \sqrt{\frac{2\ell+1}{4\pi}} \\ &\quad \times \Bigg[\left(|\zeta_{+1}|^2 + |\zeta_{-1}|^2\right) A^{\ell}_{+1,+1}\, P_\ell(\cos\theta) \\ &\quad + \sqrt{\frac{(\ell-2)!}{(\ell+2)!}}\, 2\mathrm{Re}\left(\zeta_{-1}\zeta^*_{+1}\, \mathrm{e}^{\mathrm{i}2\varphi}\right) A^{\ell}_{+1,-1}\, P^{(2)}_\ell(\cos\theta) \Bigg], \end{aligned} \tag{1.2.153}$$

where θ and ϕ are the polar and azimuthal angles of the direction $\hat{\mathbf{k}}_b$, $P_\ell(\cos\theta)$ are Legendre polynomials and $P^{(2)}_\ell(\cos\theta)$ are associated Legendre functions of order 2. Finally, the DCS (1.2.147) can be cast in the form

$$\begin{aligned} \frac{\mathrm{d}\sigma^{\mathrm{ion}}_a(W, \boldsymbol{\zeta})}{\mathrm{d}\hat{\mathbf{k}}_b} &= \frac{(2\pi)^2 e^2 c\hbar}{W}\, \frac{k_b}{\pi\epsilon_b}\, \frac{q_a}{2|\kappa_a|} \Bigg\{ \sum_{\ell} A_\ell\, P_\ell(\cos\theta) \\ &\quad + 2\left[\mathrm{Re}\left(\zeta_{-1}\zeta^*_{+1}\right)\cos(2\phi) - \mathrm{Im}\left(\zeta_{-1}\zeta^*_{+1}\right)\sin(2\phi)\right] \sum_{\ell} B_\ell P^{(2)}_\ell(\cos\theta) \Bigg\} \end{aligned} \tag{1.2.154}$$

where the coefficients A_ℓ and B_ℓ are real. It is worth noticing that the DCS is invariant under inversion of the polarization vector ($\hat{\boldsymbol{\zeta}} \to -\hat{\boldsymbol{\zeta}}$). Evidently, expressions of the coefficients A_ℓ and B_ℓ are quite involved and hard to compute because of the abundance of vector coupling coefficients. In practice, it is more efficient to calculate the DCS from the less elaborate formula (1.2.142) and the expansion (1.2.143) of the emission amplitude.

For linear polarization along the x axis, $\hat{\boldsymbol{\zeta}} = \hat{\mathbf{x}}$ ($\zeta_{+1} = -1/\sqrt{2}$, $\zeta_{-1} = 1/\sqrt{2}$), the DCS takes the form obtained by Scofield [69],

$$\frac{\mathrm{d}\sigma_a^{\mathrm{ion}}(W, \hat{\mathbf{x}})}{\mathrm{d}\hat{\mathbf{k}}_b} = \frac{(2\pi)^2 e^2 c\hbar}{W} \frac{k_b}{\pi \epsilon_b} \frac{q_a}{2|\kappa_a|} \sum_\ell \left\{ A_\ell \, P_\ell(\cos\theta) - B_\ell \cos(2\phi) \, P_\ell^{(2)}(\cos\theta) \right\}. \tag{1.2.155}$$

In the case of circular polarization, which corresponds to $\boldsymbol{\zeta} = -\boldsymbol{\xi}_{+1}$ ($\zeta_{+1} = -1$, $\zeta_{-1} = 0$, right handed) or $\boldsymbol{\zeta} = \boldsymbol{\xi}_{-1}$ ($\zeta_{+1} = 0$, $\zeta_{-1} = 1$, left handed), Eq. (1.2.154) becomes

$$\frac{\mathrm{d}\sigma_a^{\mathrm{ion}}(W, \mp\boldsymbol{\xi}_{\pm 1})}{\mathrm{d}\hat{\mathbf{k}}_b} = \frac{(2\pi)^2 e^2 c\hbar}{W} \frac{k_b}{\pi \epsilon_b} \frac{q_a}{2|\kappa_a|} \sum_\ell A_\ell \, P_\ell(\cos\theta). \tag{1.2.156}$$

As expected, in this case the angular distribution of photoelectrons is axially symmetrical, *i.e.*, independent of the azimuthal angle ϕ of the direction $\hat{\mathbf{k}}_b$. We also note that the DCSs for right- and left-handed circular polarizations are identical, and equal to the DCS for unpolarized photons (see Section 1.2.1).

Sauter [29] derived an analytical expression of the DCS for ionization of the K shell of atoms by photons linearly polarized along the x axis from the Born approximation, *i.e.*, from the above formulation with hydrogenic initial orbital and the photoelectron distorted plane waves replaced by Dirac plane waves. The normalized probability distribution function of the photoelectron direction obtained by Sauter reads [29, 70]

$$\begin{aligned} p_{\mathrm{Sauter}}(\cos\theta, \phi) &\equiv \frac{1}{\sigma_{\mathrm{K}}^{\mathrm{ion}}(W)} \frac{\mathrm{d}\sigma_{\mathrm{K}}^{\mathrm{ion}}(W, \hat{\mathbf{x}})}{\mathrm{d}\hat{\mathbf{k}}_{\mathrm{b}}} \\ &= \frac{3}{4\pi\gamma^4} \left[1 + \frac{3}{4} \frac{\gamma(\gamma-2)}{\gamma+1} \left(1 - \frac{1}{2\beta\gamma^2} \ln\frac{1+\beta}{1-\beta} \right) \right]^{-1} \\ &\quad \times \frac{\sin^2\theta}{(1-\beta\cos\theta)^4} \left\{ \cos^2\phi \left[1 - \frac{1}{2}\gamma(\gamma-1)(1-\beta\cos\theta) \right] \right. \\ &\quad \left. + \frac{1}{4}\gamma(\gamma-1)^2(1-\beta\cos\theta) \right\}, \end{aligned} \tag{1.2.157}$$

where β and γ are defined by Eqs. (1.1.125) and (1.1.126). The angular distribution for unpolarized photons is obtained by averaging over polarization directions (or, equivalently, over the azimuthal angle ϕ), which gives

$$p_{\text{Sauter}}(\cos\theta) = \frac{3}{8\pi\gamma^4}\left[1+\frac{3}{4}\frac{\gamma(\gamma-2)}{\gamma+1}\left(1-\frac{1}{2\beta\gamma^2}\ln\frac{1+\beta}{1-\beta}\right)\right]^{-1} \times \frac{\sin^2\theta}{(1-\beta\cos\theta)^4}\left[1+\frac{1}{2}\gamma(\gamma-1)(\gamma-2)(1-\beta\cos\theta)\right]. \tag{1.2.158}$$

Sauter's distribution is used in the majority of high-energy Monte Carlo radiation codes. It gives fairly realistic results for the K shell of elements with small and moderate atomic numbers, say up to $Z \sim 30$. However, the corresponding total cross section is less accurate than Pratt's high-energy formula (1.1.124).

1.2.1 Partially polarized photons

Pure polarization states can be described by the Poincaré vector, $\mathbf{P} = (P_1, P_2, P_3)$, whose components are the Stokes parameters (see Appendix B). The Poincaré vector of pure states has unit length and can be expressed in polar form, [see Eq. (1.1.53)],

$$\mathbf{P} = (\sin\alpha\,\cos\beta, \sin\alpha\,\sin\beta, \cos\alpha)\,. \tag{1.2.159}$$

The corresponding polarization vector is [see Eq. (1.1.55)]

$$\boldsymbol{\zeta}(\mathbf{P}) = \cos(\alpha/2)\hat{\boldsymbol{\epsilon}}_1 + \sin(\alpha/2)\exp(\mathrm{i}\beta)\hat{\boldsymbol{\epsilon}}_2, \tag{1.2.160}$$

with spherical components [$\zeta_\nu = \boldsymbol{\xi}_\nu\cdot\boldsymbol{\zeta}$, see Eqs. (1.1.35) and (1.1.33)]

$$\zeta_{+1}(\mathbf{P}) = -\frac{1}{\sqrt{2}}\left[\cos(\alpha/2) + \mathrm{i}\sin(\alpha/2)\exp(\mathrm{i}\beta)\right], \tag{1.2.161a}$$

and

$$\zeta_{-1}(\mathbf{P}) = \frac{1}{\sqrt{2}}\left[\cos(\alpha/2) - \mathrm{i}\sin(\alpha/2)\exp(\mathrm{i}\beta)\right]. \tag{1.2.161b}$$

It follows that

$$\zeta_{-1}(\mathbf{P})\zeta^*_{+1}(\mathbf{P}) = -\tfrac{1}{2}\left(\cos\alpha - \mathrm{i}\sin\alpha\cos\beta\right) = -\tfrac{1}{2}(P_3 - \mathrm{i}P_1). \tag{1.2.162}$$

Consequently, the DCS (1.2.154) can be written as

$$\frac{\mathrm{d}\sigma_a^{\text{ion}}(W,\mathbf{P})}{\mathrm{d}\hat{\mathbf{k}}_b} = \frac{(2\pi)^2 e^2 c\hbar}{W}\frac{k_b}{\pi\epsilon_b}\frac{q_a}{2|\kappa_a|}\left\{\sum_\ell A_\ell\,P_\ell(\cos\theta) - [P_3\cos(2\phi) + P_1\sin(2\phi)]\sum_\ell B_\ell P_\ell^{(2)}(\cos\theta)\right\}. \tag{1.2.163}$$

Let us now consider the angular distribution of photoelectrons for photons with arbitrary polarization represented by the Poincaré vector, $\mathbf{P} = (P_1, P_2, P_3)$. The polarization density matrix can be expressed as [see Eq. (1.1.60)]

$$\rho = (1-P)\,\frac{1}{2}\begin{pmatrix} 1 & 0 \\ 0 & 1 \end{pmatrix} + P\,\frac{1}{2}\begin{pmatrix} 1+P_3' & P_1'-\mathrm{i}P_2' \\ P_1'+\mathrm{i}P_2' & 1-P_3' \end{pmatrix}, \tag{1.2.164}$$

where $P = (P_1^2 + P_2^2 + P_3^2)^{1/2}$ is the degree of polarization and $P_i' = P_i/P$. The latter quantities are the Stokes parameters of a pure state with polarization vector

$$\boldsymbol{\zeta}(\mathbf{P}') = \cos(\alpha'/2)\,\hat{\boldsymbol{\epsilon}}_1 + \sin(\alpha'/2)\exp(\mathrm{i}\beta')\,\hat{\boldsymbol{\epsilon}}_2 \tag{1.2.165}$$

where

$$\alpha' = \arccos P_3', \qquad \exp(\mathrm{i}\beta') = \frac{P_1' + \mathrm{i}P_2'}{\sqrt{1-P_3'^2}}\,. \tag{1.2.166}$$

Equation (1.2.164) means that the photon beam can be regarded as the incoherent superposition of two partial beams: an unpolarised beam with relative intensity $(1-P)$, and a fully polarized beam with Poincaré vector $\mathbf{P}' = \mathbf{P}/P$ and relative intensity equal to the degree of polarization. On the other hand, the unpolarised beam is equivalent to the superposition of two polarized beams with opposing polarizations, $\mathbf{P}'$ and $-\mathbf{P}'$, and equal intensities. This implies that the DCS for photons with polarization $\mathbf{P}$ can be calculated as a weighted average of the DCSs for photons with pure polarizations $\mathbf{P}'$ and $-\mathbf{P}'$,

$$\begin{aligned}\frac{\mathrm{d}\sigma_a^{\mathrm{ion}}(W,\mathbf{P})}{\mathrm{d}\hat{\mathbf{k}}_b} &= \frac{1-P}{2}\left(\frac{\mathrm{d}\sigma_a^{\mathrm{ion}}(W,\boldsymbol{\zeta}(\mathbf{P}'))}{\mathrm{d}\hat{\mathbf{k}}_b} + \frac{\mathrm{d}\sigma_a^{\mathrm{ion}}(W,\boldsymbol{\zeta}(-\mathbf{P}'))}{\mathrm{d}\hat{\mathbf{k}}_b}\right) + P\,\frac{\mathrm{d}\sigma_a^{\mathrm{ion}}(W,\boldsymbol{\zeta}(\mathbf{P}'))}{\mathrm{d}\hat{\mathbf{k}}_b} \\ &= \frac{1+P}{2}\,\frac{\mathrm{d}\sigma_a^{\mathrm{ion}}(W,\boldsymbol{\zeta}(\mathbf{P}'))}{\mathrm{d}\hat{\mathbf{k}}_b} + \frac{1-P}{2}\,\frac{\mathrm{d}\sigma_a^{\mathrm{ion}}(W,\boldsymbol{\zeta}(-\mathbf{P}'))}{\mathrm{d}\hat{\mathbf{k}}_b}\end{aligned} \tag{1.2.167}$$

where

$$\boldsymbol{\zeta}(-\mathbf{P}') = \sin(\alpha'/2)\,\hat{\boldsymbol{\epsilon}}_1 - \cos(\alpha'/2)\exp(\mathrm{i}\beta')\,\hat{\boldsymbol{\epsilon}}_2 \tag{1.2.168}$$

is the polarization vector corresponding to the Poincaré vector $-\mathbf{P}'$ [see Eq. (1.1.55)]. The DCS (1.2.167) can be expressed as a Legendre series in terms of the Stokes parameters,

$$\begin{aligned}\frac{\mathrm{d}\sigma_a^{\mathrm{ion}}(W,\mathbf{P})}{\mathrm{d}\hat{\mathbf{k}}_b} &= \frac{(2\pi)^2 e^2 c\hbar}{W}\,\frac{k_b}{\pi\epsilon_b}\,\frac{q_a}{2|\kappa_a|}\left\{\sum_\ell A_\ell\,P_\ell(\cos\theta)\right. \\ &\qquad \left. - \left[P_3\cos(2\phi) + P_1\sin(2\phi)\right]\sum_\ell B_\ell P_\ell^{(2)}(\cos\theta)\right\}.\end{aligned} \tag{1.2.169}$$

1.3 Numerical calculation of cross sections

Our Fortran program PHOTACS calculates cross sections for ionization and excitation of subshells of free atoms and ions using the theory presented above (Section 1.1). The structure and numerical algorithms adopted in the program are similar to those employed in the programs developed by Bote and Salvat [71, 72] to compute cross sections for inelastic collisions of charged particles with atoms. PHOTACS calculates the radial functions of initial and final electron states by means of an updated version of the subroutine package RADIAL [73, 74], which allows strict control of numerical round-off errors. The RADIAL subroutines are also used in the self-consistent calculation of the DHFS potential [74]. Vector-coupling coefficients and reduced matrix elements of the Racah tensors are calculated from their analytical formulas [38, 39] using a subroutine package that performs arithmetic operations at a high level of precision, well beyond Fortran double precision, by working in radix (base) 1,000.

The program reads the potential $V(r)$ felt by the active electron from an input file; the information to be provided in that file is a table of values of the function $rV(r)$, for a dense enough grid of radii to allow accurate interpolation by natural cubic splines. The function $rV(r)$ is required to be finite for all r, but is otherwise arbitrary. Optionally, the program also allows the unscreened Coulomb potential of the bare point nucleus to be used. As indicated above, in the calculations it is normally used the DHFS potential described in Section A.2. For the evaluation of the integrals (1.1.96), the radial functions are calculated for a non-uniform radial grid, with 16 points in a wavelength, from which the integrals are evaluated using the 6-point Lagrange quadrature formula. The stability of the calculations was verified by using denser radial grid with 25 points/wavelength; cross sections computed with the two radial grids differ by less that 10^{-6}.

The reduced cross section for excitation, $\overline{\sigma}_{ba}^{\rm exc}(W)$, is computed according to Eq. (1.1.103). The difficulty of the calculation increases with the principal quantum number n_b of the final level because the radial functions of the final state extend to larger radii. We only need values of the radial functions of the final level for computing the radial integrals (1.1.96) for the relatively small radii at which the radial functions of the initial state take appreciable values. However, the radial equations of the final state still need to be integrated up to large radii to determine the energy and normalization of the state. As indicated in Section 1.1.9 above, the program effectively computes the reduced cross sections for excitations to discrete levels with $n_b \leq 18$.

The calculation of ionization cross section $\sigma_a^{\rm ion}(W)$, Eq. (1.1.109), is performed by adding the grouped contributions from $\kappa_b = \pm|\kappa_b|$ in increasing order of $|\kappa_b|$. The summation is discontinued at the first term which becomes less than 10^{-6} times the accumulated sum. Our program allows values of $|\kappa_b|$ to be considered up to ~ 200. The number of terms $N_{|\kappa|}$ needed to get convergence of the series (1.1.109) increases with the energy of the photon, and it is fairly independent of atomic number of the target atom and the considered subshell. Typical values of $N_{|\kappa|}$ are about 5, 7, 10, 15, 35, and 150 for photons with energies of 100 eV, 1 keV, 10 keV, 100 keV, 1 MeV, and 10 MeV, respectively. An analysis of the variation of the calculated $\mathcal{G}^{\rm ion}(\kappa_b, \kappa_a)$ values with $|\kappa_b|$

indicates that the relative numerical errors of the computed ionization cross sections are usually less than about 10^{-5}.

The ionization cross section $\sigma_a^{\rm ion}(W)$ can be calculated for photon energies W from threshold ($W = E_a$) up to a cut-off energy $W_a^{\rm cut}$ for which the spacing of the radial grid where wave functions are tabulated is insufficient to reproduce the fast oscillations of the integrands in Eqs. (1.1.96). Typically, the cut-off energy is larger than about $500E_a$, where $E_a = -\epsilon_a$ is the ionization energy of the active shell. It is worth mentioning that, despite our superior computer power, PHOTACS does not allow much higher energies than Scofield's calculations to be reached.

The computer program generates a table of $\sigma_a^{\rm ion}(W)$ for a grid of energies extending from threshold up to the cut-off energy. This table contains a nearly logarithmic grid, with 15 points per decade, plus a number of additional energies that are set by means of a self-adaptive method. The resulting energy grid is such that linear log-log interpolation errors are kept below some prescribed limit, which in the program was set equal to 0.05 %. For elements with atomic numbers near 19, 37, 55, and 87 (*i.e.*, near the alkalies), this procedure reveals near-edge structures that were partially overlooked in Scofield's tables. Otherwise, our results agree closely with those of Scofield, typically to within about 0.05 %, the differences being mostly attributable to the different numerical methods employed to solve the radial Dirac equations.

Figure 1.2 displays the cross section for photoionization ($W > E_a$) of the K shell of argon atoms as a function of the photon energy. The solid line represents results calculated from the general formula (1.1.109), and extends over the energy interval where calculations with PHOTACS are feasible, *i.e.*, from the ionization threshold up to $W_a^{\rm cut}$, which in the present case is 2 MeV. For comparison purposes, it is included cross-section data from the EPDL [14], which were calculated by Scofield using the DHFS potential. The close agreement between our results and those of Scofield, which were generated using different computer codes, provides a clear indication of the accuracy of the numerical algorithms. Notice that the extrapolation formula (1.1.133) agrees well with the numerical results in a wide interval, differences are less than 2 % down to about 200 keV.

Because excitation to bound levels is limited to a narrow energy interval, it is neglected in most of the existing databases and Monte Carlo simulation codes. Furthermore, the finite width of atomic levels is usually disregarded. These two effects become significant for describing the penetration and dosimetry of photon beams with energies near absorption edges. A situation where these effects are observed is in experimental measurements of the photon mass energy-absorption coefficient of air [75]. The values of the coefficient predicted by Monte Carlo codes, although in fairly good agreement with experiment, fail to reproduce the structure displayed by the measured coefficient near the energy of the K absorption edge of argon.

The contribution from excitation to bound levels (Section 1.1.9), the effect of the atomic-level width (Section 1.1.11), and the normalization screening correction (Section (1.1.12)), are accounted for by a post-processing program, named PHOTACS-PP, which

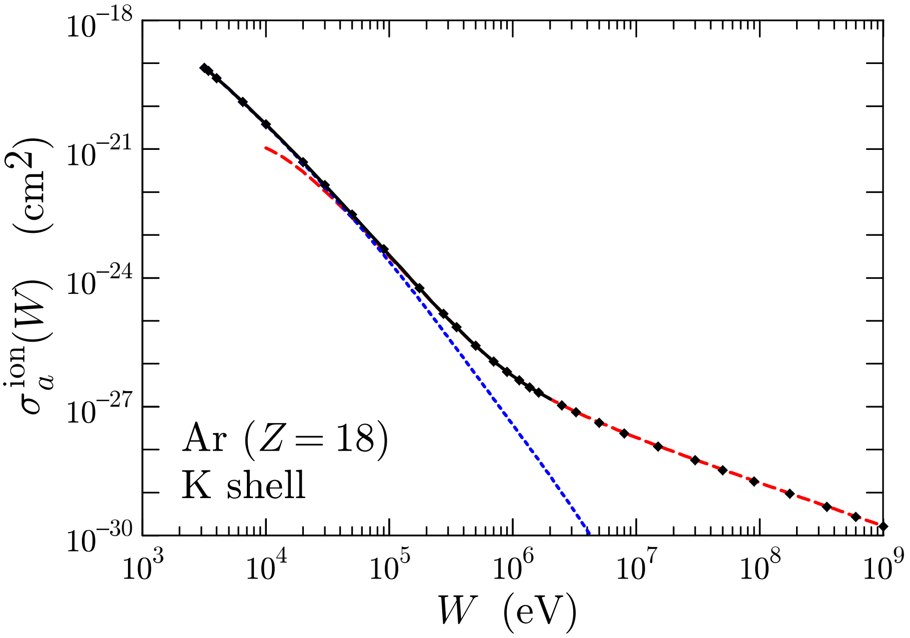

Figure 1.2: Cross section for ionization of the K shell of argon atoms by absorption of photons, as a function of the photon energy W. The solid curve, which extends from threshold up to about 2 MeV, is the numerical result calculated from expression (1.1.109). The dashed curve (red online) is the prediction of the extrapolation formula (1.1.134). The dotted curve (blue online) was obtained from the dipole approximation. Diamonds represent data from the EPDL [14].

reads the tables of numerical cross sections generated by PHOTACS. This program determines the polynomial approximation (1.1.122) for the excitation pseudo-continua, extrapolates the ionization cross section to high energies using the formula (1.1.134), and performs a convolution with the Lorentzian profile (1.1.135) [see Eq. (1.1.137)]. The result from PHOTACS-PP is a realistic photoelectric cross section, which varies continuously with energy and exhibits excitation structures that are in qualitative agreement with measurements in gases. Figure 1.3 displays this cross section for absorption in the K shell of argon atoms of photons with energies near the edge (using the original DHFS energies calculated by PHOTACS). The right panel is a magnified view of the step function (1.1.118) which describes the contribution of excitations to bound levels with $n_b \leq 18$, and the polynomial approximation (1.1.122) to the quasi-continuum. Notice that, as it is already mentioned, the excitation and ionization cross sections match at the edge. Figure 1.4 shows calculated cross sections for the subshells of argon and their sum, the atomic cross section. Interestingly, the dipole approximation is seen to predict subshell cross sections quite accurately for photon energies up to about 10 keV.

Optionally, the program PHOTACS can calculate the DCS for ionization, *i.e.*, the photoelectron angular distribution, for a photon beam with energy W and polarization defined by the Stokes parameters $\mathbf{P}$ [see Eq. (1.2.167)]. The calculation starts by computing the ionization cross section $\sigma_a^{\rm ion}(W)$, Eq. (1.1.108), as described above. The

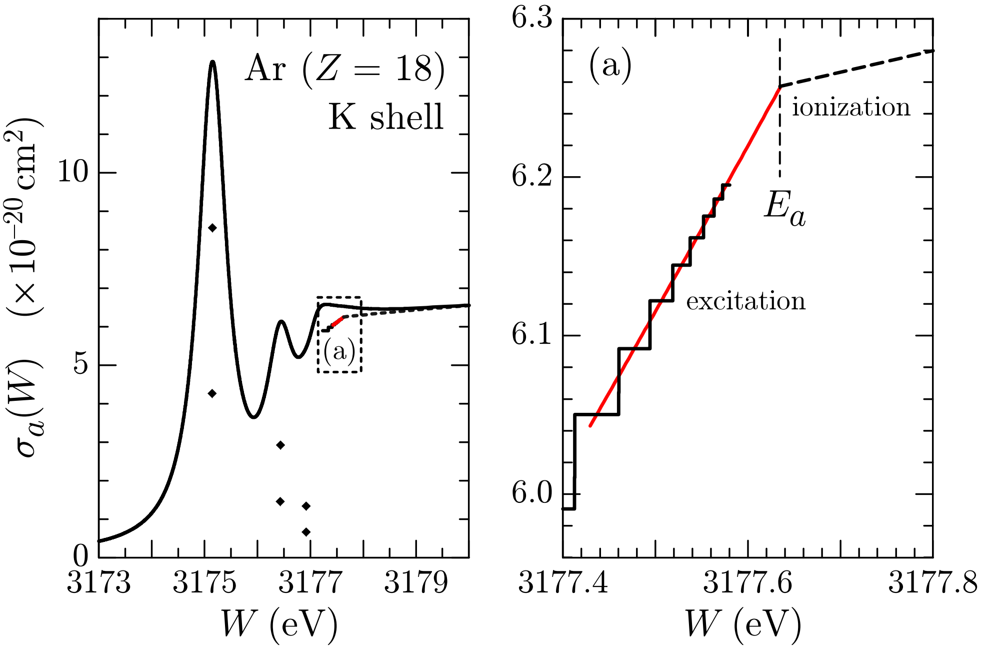

Figure 1.3: Left: Cross section for absorption in the K shell of argon atoms as a function of the photon energy W in a narrow interval around the edge energy. The solid curve in the left panel is the cross section given by PHOTACS-PP, including contributions from excitations to bound levels and accounting for the finite level width. Diamonds represent the energies and relative contributions (not to scale) of the lowest excited levels, which are treated as discrete resonances. Right: Magnified view of the step function (1.1.118), the polynomial approximation (1.1.122) (solid curve, red online) to the excitation quasi-continuum, and a part of the photoionization cross section (dashed curve).

quantities ${}^{\text{e,m}}\mathcal{Y}^{J}_{\epsilon_b\kappa_b;\epsilon_a\kappa_a}$ [see Eqs. (1.2.146)] computed at this stage are stored in memory. The DCSs for pure polarization states can be calculated either from Eq. (1.2.142), which involves a minimum of angular momentum algebra, or from the more elaborate expression (1.2.154), which requires lengthier preliminary calculations. The DCS is calculated and tabulated for a dense grid of directions $\hat{\mathbf{k}}_b$ of the photoelectron, defined by the polar and azimuthal angles, θ and ϕ, respectively. The DCSs obtained from the two schemes [*i.e.*, from Eqs. (1.2.142) and (1.2.154)] are identical because we are using exact (double precision) values of vector coupling coefficients. The amount of work needed to sum the series (1.2.150) increases quickly with photon energy. Consequently, for photon energies well above the absorption edge, the calculation from Eq. (1.2.142) is much faster than from Eq. (1.2.154). The accuracy of the results can be verified by comparing the cross section $\sigma_a^{\text{ion}}(W)$ calculated previously with the value obtained by numerical integration of the DCS table for non-polarized photons. The numerical values resulting from the two calculations normally agree to more than 5 digits.

Figure 1.5 shows calculated DCS for ionization of the K shell of argon by unpolarized (or circularly polarized) photons. For comparison purposes, it is also included

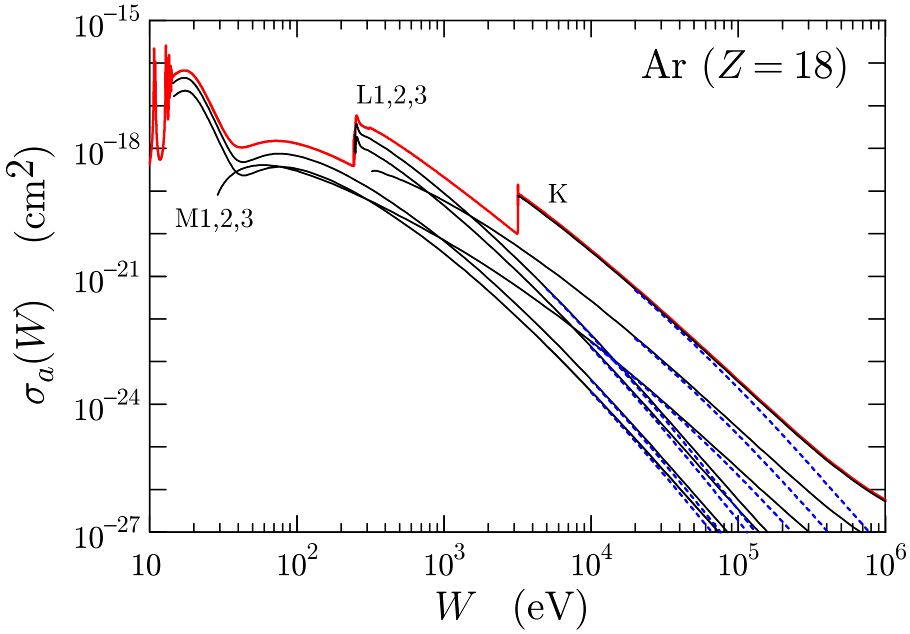

Figure 1.4: Cross sections for photoabsorption (excitation and ionization) in the subshells of argon atoms as functions of the photon energy W (thin solid curves), calculated by PHOTACS-PP using experimental level widths. The thick solid curve (red online) represents the total atomic cross section. Dashed curves (blue online) are cross sections obtained from the dipole approximation.

results from the dipole approximation, *i.e.*, DCS calculated from the emission amplitude (1.2.143) with the $G_\pm$ coefficients given by Eq. (1.1.115). It is seen that the dipole approximation works much better for the total cross section than for the DCS. The dipole DCS agrees reasonably with the partial-wave results only for energies near the ionization threshold; it fails to describe the progressive decrease of the most probable emission angle when the photon energy increases. Interestingly, the Sauter distribution, Eq. (1.2.158), renormalized to reproduce the calculated cross section, provides quite an accurate description of the angular distribution for all energies because the example falls within the domain of applicability of Sauter's theory (K shell, moderate atomic number). For other subshells and for heavier elements the approximation is much less satisfactory.

Figure 2.17 displays DCSs of the K shell of argon for 50 keV photons with linear polarizations along the x and y axes. The sum of these two distributions, with weights equal to $\frac{1}{2}$, is the DCS for an unpolarized photon beam [see Eq. (1.2.167)], the numerical results agree with those obtained for a circularly polarized beam, which are independent of the azimuthal angle ϕ [cf. Eq. (1.2.156)], to more than 5 digits. The DCS for linear polarization at 45 degrees from the x axis, which corresponds to the Poincaré vector $\mathbf{P} = (1, 0, 0)$, is also displayed. Evidently, the maxima in the DCS are at directions with the azimuthal angle coinciding with that of the electric field; the polar angle of the maxima is close to 90 deg at small energies and decreases when the photon energy

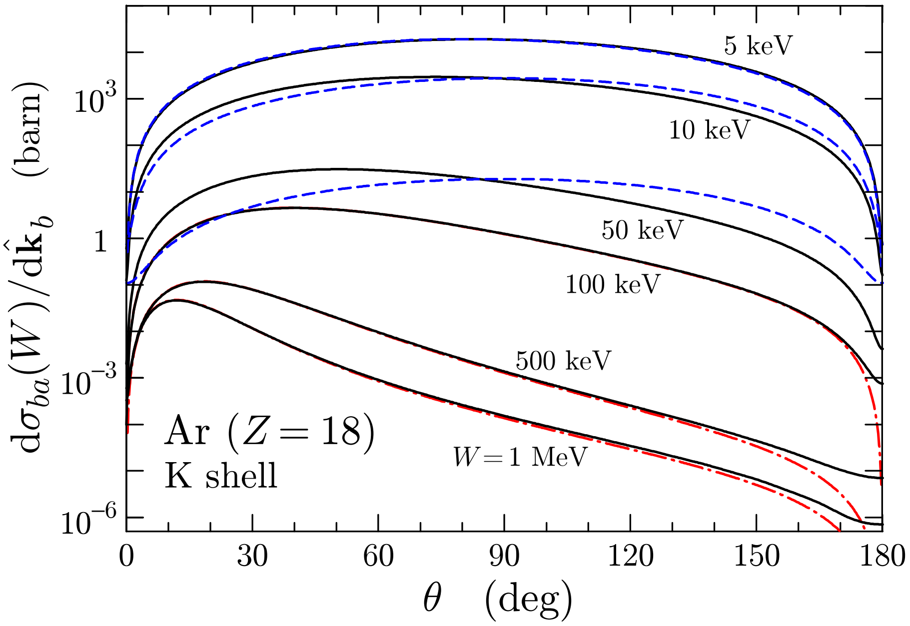

Figure 1.5: Differential cross sections for ionization of the K shell of argon atoms by unpolarized photons of the indicated energies. Solid curves represent partial-wave numerical results. Dashed curves (blue online) are results from the dipole approximation. Dot-dashed curves (red online) correspond to the Sauter distribution, Eq. (1.2.158), multiplied by the numerical total cross section calculated from Eq. (1.1.109).

increases (Fig. 1.5) because photoelectrons do absorb part of the linear momentum of the photon.

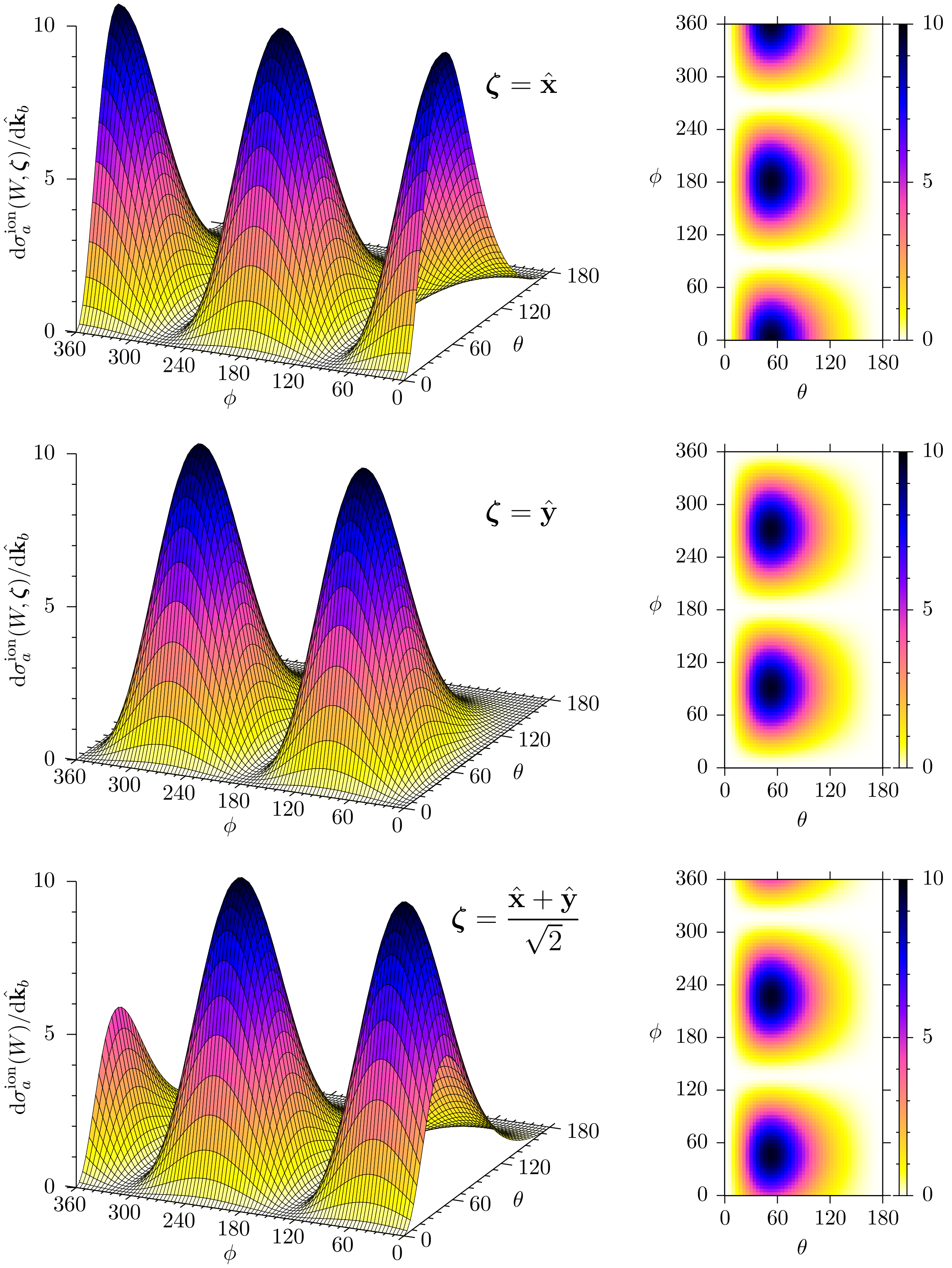

Figure 1.6: DCSs for ionization of the K shell of Ar atoms by absorption of 50 keV photons, in barn ($= 10^{-24}$ cm^2), as functions of the polar angle θ and the azimuthal angle ϕ of the direction of the emitted photoelectron, both in degrees. The plots correspond to photons linearly polarized along the x axis [$\mathbf{P} = (0, 0, 1)$, top], along the y axis [$\mathbf{P} = (0, 0, -1)$, middle], and along the direction $\hat{\boldsymbol{\zeta}} = (\hat{\mathbf{x}} + \hat{\mathbf{y}})/\sqrt{2}$, at 45 deg from the x axis [$\mathbf{P} = (1, 0, 0)$, bottom]. (Color online)

Chapter 2

Inverse problems in radiation spectrometry

Inverse problems are a relatively recent mathematical branch. They were studied for the first time by the Soviet-Armenian physicist Viktor Ambartsumian which published his work in the Zeitschrift für Physik journal in 1929. Ambartsumian studied the inverse of the Sturm-Liouville problem trying to find the form of an equation given an ensemble of eigenvalues. The work of Ambartsumian remained in obscurity until the interest on these problems, coming from both the scientific and the industrial community, started to increase with the technological development of modern diagnostics machines like TAC, SPECT, etc. The principle of operation of these technologies is to reconstruct two or three dimensional objects given their projections. Practically they solve the inverse problem of reconstructing the geometry of an object using its projection.

This kind of problem has ancient roots. About 2000 years ago Plato in the VII book of "The Republic" described the so called "Problem of the cave". A prisoner, trapped in a cave, try to reconstruct the objects outside the cave by observing their shadows projected on the cave wall. Plato used, without having no idea of it, an inverse problem as a metaphor for the human discovery of reality and its real nature. Such metaphor describes perfectly the essence of one of the most well known inverse problem type: the unfolding.

In the unfolding process the data, coming from a measurement, are corrected by the influences of the measurement system. Practically the unfolding recovers, when it is possible, the loss of informations due to the measuring process.

Actually there is no generalized procedure to follow for solving an inverse problem. Each different situation could require a special strategy, centred on the specific characteristics of the problem. Sometimes the formalization of an inverse problem can lead to the so called ill position which prevents any attempt to find a meaningful solution.

A more rigorous description of an inverse problem can be given by considering the following equation:

$$\mathbf{y} = \mathcal{K}\mathbf{x} \;, \tag{2.0.1}$$

where $\mathbf{x}$, $\mathcal{K}$ and $\mathbf{y}$ are respectively a generic input vector, an operator and an output vector. Equation (2.0.1) represents a classical cause-effect (input-output) direct problem which is the standard description for several physical systems. From the direct problem it is possible to define two different types of inverse problems:

1)Given the output and the operator, reconstruct the input.

2)Given the output and the input reconstruct the operator.

Unfolding problem belongs to the first category and it will be the central topic of this chapter. Formally it is possible to represent an inverse problem by the inversion of the operator $\mathcal{K}$:

$$\mathbf{x} = \mathcal{K}^{-1}\mathbf{y} \ . \tag{2.0.2}$$

Usually and unfortunately it is not easy to compute the inverse of an operator and the inverse problem has to be formalized by using the direct one. This is not the only difficult in approaching this topic. Another fundamental peculiarity is that inverse problems are usually ill posed.

A mathematical problem is ill posed if it does not respect the so called Hadamard conditions:

1)Existence: Given $\mathbf{y}$ it exists, at least, one $\mathbf{x}$ which satisfies Eq.(2.0.1)

2)Uniqueness: Given $\mathbf{y}$ it exists only and only one $\mathbf{x}$ which satisfies Eq.(2.0.1)

3)Stability: $\mathbf{x}$ depends with continuity on $\mathbf{y}$

The most frequent situation is that the direct problem is well-posed and its related inverse one is not. With an Ill-posed problem there is no hope to find a solution with physical meaning, however in some cases it is possible to reformulate the problem avoiding the ill-position.

All this peculiarity characterize also unfolding for radiation spectrometry, which is the central topic of this chapter.

Referring to fig. (2.1) when it is performed an X- or Gamma-Ray measurement part of the scattered beam, coming from the target, is captured by the detector which produces a signal collected by the pulse handling circuitry with the multi-channel analyser (MCA). Unfolding strategy reconstructs the scattered spectrum (original spectrum) by the knowledge of the measurement (the spectrum given by the multichannel analyser) and all the effects (o the measure) of the detector and its related pulse handling circuitry. It is worth nothing that the effects coming from the pulse handling circuitry and the detector are uncorrelated and they can be separated without any consequences to the generality of the problem. This means that the unfolding can be divided as well in two steps:

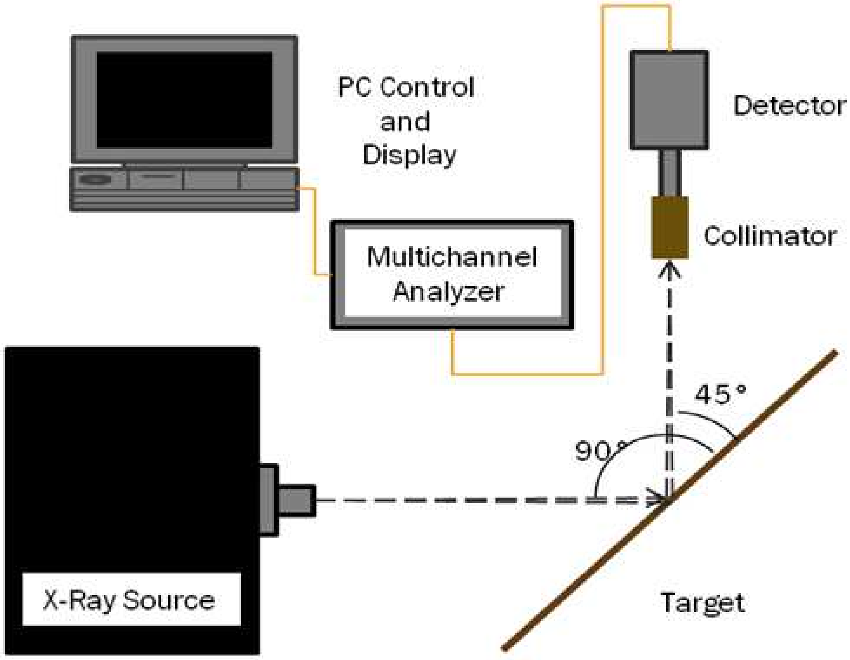

Figure 2.1: Radiation measure system

1)Unfolding from the effects of the pulse handling circuitry (Pulse pile-up).

2)Unfolding from the effects of the detector (detector response function).

Following this subdivision the present chapter is organized in three sections.

In the first section it will be discussed the so called pulse pile-up effect and its consequences on a measure. This is one of the most important pulse handling circuitry effects on the measured spectrum. Other effects coming from pulse handling circuitry will be discarded. This is possible because modern detectors comprise built in electronics which can efficiently correct these effects on-line (i.e. during the measure), without the need of post process correction.

Then a second section regarding the computation of the so called detector response function which represents an elegant formalism for describing together the principal mechanism of interaction between the radiation and the detector.

Finally it is reported a concluding section on the detector unfolding strategy.

For all the topics described before it will be reported all the results obtained during this PhD course which are published in [2] [3] [4] [5]

2.1 Pulse pile-up

One of the most important influence of the pulse handling circuitry, on the radiation measure, is represented by the so called pulse pile-up effect (PPU). The PPU is an always present effect which cannot be completely avoided in every measure performed with an high counting rate (necessary for a good statistics). Pulse handling circuitry cannot process correctly too many pulses arriving in a too short time interval. When pulses are too close together they can be overlapped and recorded at wrong energies.

PPU effect is strictly connected to the shape into which the pulses are modelled inside the pulse handling circuitry. As reported in [76], there are two different type of PPU: tail and peak PPU.

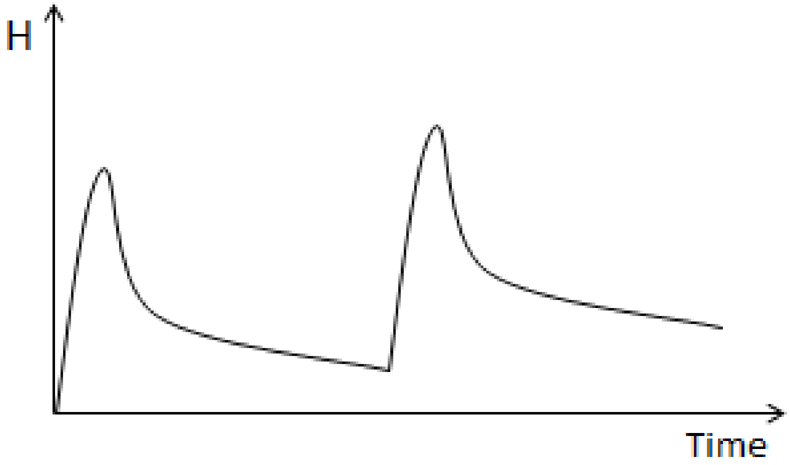

Figure 2.2: Tail pile-up

If the pulse shape is characterized by long duration tail or undershoot it is possible that one or several pulses can be superposed to the tail (or to the undershoot) leading to the so called tail pile-up. The direct consequence of this superposition are pulses collected with wrong energies. In fig.(2.2) it is possible to see the tail PPU between two pulses characterized by long tail. Through tail PPU long pulse tail or undershoot worsen the detector resolution adding wings to the recorded peaks in the pulse height spectra. Unfortunately tail and undershoot can persist for relatively long time periods so tail pile-up can be significant even at relatively low counting rates.

Actually this effect can be efficaciously corrected on-line by the so called rise time discriminator (RTD) [76] function which is comprised in several modern detector pulse handling circuitry. RTD cuts the long pulse tail or undershoot allowing to discard this effect without a significant error.

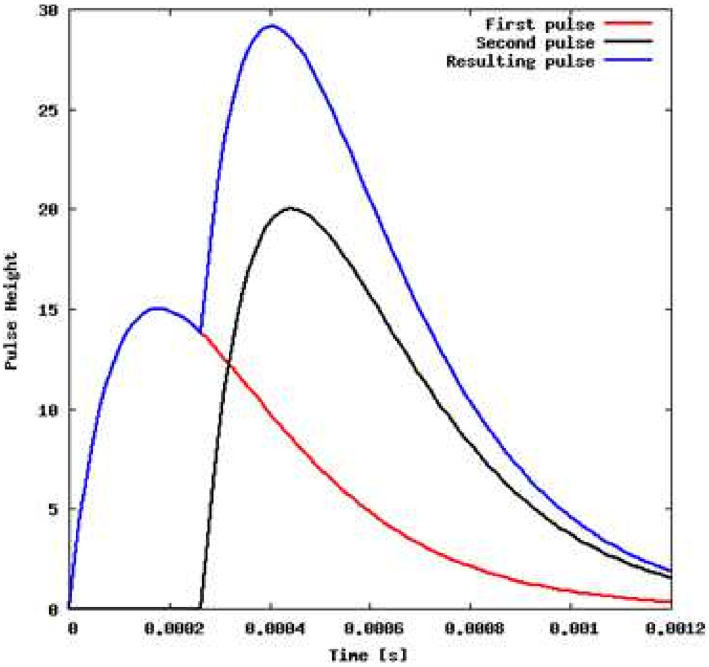

Figure 2.3: Peak pile-up

Regarding Peak PPU (from now when is used the acronym PPU it will refer only to peak pulse pile-up) it is the most difficult PPU effect to correct in a measured spectrum. It is directly connected to the so called dead time τ of the counting system. This parameter, τ, is defined as the minimum amount of time necessary to record two pulses as separated events [76]. If the time gap between two pulses is lower than the dead time, they cannot be distinguished and are recorded as a single pulse at a distorted energy (PPU effect, see fig.2.3). It is possible that not only two but also three or more pulses (a pulse train) are recorded as one. The number of pulses piled-up together is called the order of the pile-up.

Due to the random nature of emission, the PPU worsen with the increasing of the radiation source emission rate. Increasing the emission rate, in fact, the probability to have time gap smaller than τ increases and, as a consequence, PPU becomes more and more visible. High emission rate is mandatory for obtaining spectra with good statistics in an acceptable amount of time. In order to avoid severe distortions due to PPU, modern detectors comprises built in rejection circuitry which performs an on-line correction of PPU. Unfortunately the current state of the art of rejection circuitry can only attenuate PPU without correcting it at all. The remaining distortion could be still evident and not negligible in the measures requiring a post process correction.

There are two opposite and so called dead time behaviours for a pulse handling circuitry as showed in fig.(2.4).

In the paralyzable detector true events occurring during a dead time are assumed

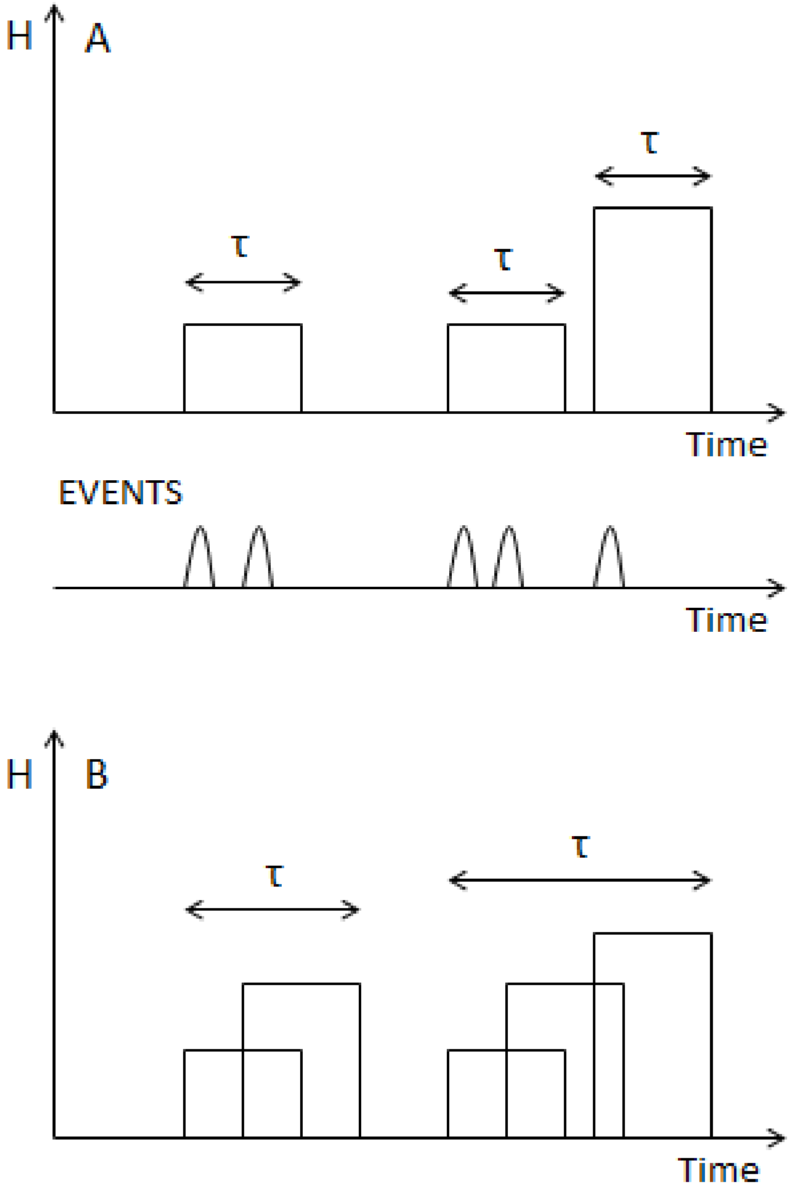

Figure 2.4: Dead time behaviours: (A) Non paralyzable detector. (B) paralyzable detector.

to extend the dead time by another τ period following the lost event. In the non paralyzable, events occurring in the dead time are assumed to have no effect on the behaviour of the detector. The paralyzability behaviour of a detector directly affects the measured counting rate which can be strongly different from the true interaction rate.

It is possible to define the true interaction rate n as the total number of events occurring in the detector during the real measurement time. Instead the measured counting rate m represents the total number of recorded pulses during the live time of the detector. As reported in [76] in the nonparalyzable detector:

$$n - m = nm\tau, \tag{2.1.3}$$

where $n\tau$ represents the average number of pulses lost in the dead time. Multiplying this average loss with the measured counting rate it is obtained the difference in Eq.(2.1.3) which give the relation:

$$n = \frac{m}{1 - m\tau}. \tag{2.1.4}$$

In the paralyzable case dead periods are not of fixed lengths and it is not possible to apply the same argument for the nonparalyzable. However the rate m is identical to the rate of occurrences of time intervals between true events which exceed τ:

$$m = n\mathrm{e}^{-n\tau}. \tag{2.1.5}$$

Real detectors have always an hybrid behaviour and paralyzable and nonparalyzable models are only extreme cases (see [76]).

PPU has three important consequences on the measured spectra: in first place, the recorded spectrum suffer a net loss of counts; secondly, pile-up photons are assigned to wrong energy channels and, finally, the whole spectrum is distorted since the lost pulses are not collected at the proper energies.

Different post processing methods have been developed for characterizing the PPU and to obtain a corrected high counting spectrum. Analytical techniques based on first principles were implemented in the works [77] and [78]. Statistical methods were also implemented. The Monte Carlo approach was introduced by Bristow and Harrison [79]. In order to make the Monte Carlo strategy adaptable to different kind of detectors Sabbatucci et al. [3] proposed the code MCPPU which allows to consider the specific pulse shape of the detector.

In what follows it will be exposed a new theoretical approach developed during this PhD course [2] and a revisited Monte Carlo approach [3] to the PPU. Regarding the theoretical approach it will be considered only second order PPU and a rectangular pulse shape. Due to this assumptions it is possible to provide a simple and fast strategy for PPU correction which requires a minimum amount of information for being applied (the dead and live time and the measurement). The Monte Carlo approach indeed will be introduced for handling more complicated situations where the pulse shape can not be considered rectangular and higher PPU orders are not negligible. The solutions of both approaches will be compared for some paradigmatic examples. In particular, it will be considered a Si solid state detector (SSD) comprising PPU suppression circuitry active.

2.1.1 Peak PPU Balance equation

Consider a measured spectrum $y(E)$ in a continuous energy range and the related measured counts in each infinitesimal energy bin dE, i.e. $y(E)dE$. From the physical point of view it is considered the measured spectrum before the action of the MCA. The $y(E)$ spectrum can be related to the original spectrum $h(E)$, free from PPU effect, through the following counts balance equation:

$$y(E)dE = h(E)dE - L(E)dE + R(E)dE \; , \tag{2.1.6}$$

where $L(E)dE$ and $R(E)dE$ denote, respectively, the probable number of lost and incoming pulses due to PPU in the generic bin $[E, E+dE]$. It is possible to introduce the normalized original spectrum $\overline{h}(E)$ and the total number of counts N_t as:

$$\overline{h}(E) = h(E) / \int_0^\infty h(E')dE' = h(E)/N_t \; , \tag{2.1.7}$$

and the related quantity $\overline{h}(E)dE$ which represents the probability of having one pulse with energy between E and $E + dE$. Assuming the generation of different pulses as an ensemble of completely independent processes the probability to have two pulses with energy in $[E_1, E_1 + dE_1]$ and in $[E_2, E_2 + dE_2]$ is simply $\overline{h}(E_1)\overline{h}(E_2)dE_1dE_2$.

In order to find the mathematical expressions for both $L(E)dE$ and $R(E)dE$, it is possible to introduce the differential PPU probability $\left(\partial\overline{P}/\partial E\right) dE$. This quantity represents the probability of having second order PPU with the resulting pulse energy lying in $[E, E+dE]$. The integral over all the possible resulting energies represents the total probability $\overline{P}$ of having second order PPU.

Using the total PPU probability the expression of $L(E)dE$ is:

$$L(E)dE = 2\overline{P}h(E)dE \; . \tag{2.1.8}$$

The probability of having PPU, considering the pulse coming from $[E, E + dE]$ as the first or the second pulse, is the same and so the factor 2 is introduced.

Regarding $R(E)dE$ the probability of having two pulses with energy in $[E_1, E_1+dE_1]$ and $[E_2, E_2+dE_2]$ which, piled-up together, produce a new pulse with energy in $[E, E+dE]$ is $\overline{h}(E_1)\overline{h}(E_2)\left(\partial\overline{P}/\partial E\right) dE_1dE_2dE$. By integrating this expression and multiplying it by N_t we obtain:

$$R(E)dE = N_t \left(\int_0^\infty \int_0^\infty \overline{h}(E_1)\overline{h}(E_2) \frac{\partial\overline{P}}{\partial E} dE_1 dE_2 \right) dE \; . \tag{2.1.9}$$

By replacing Eqs.(2.1.8) and (2.1.9) in Eq. (2.1.6) we obtain the nonlinear integral balance equation:

$$y(E) = \left(1 - 2\overline{P}\right) h(E) + N_t \int_0^\infty \int_0^\infty \overline{h}(E_1)\overline{h}(E_2)\frac{\partial \overline{P}}{\partial E} dE_1 dE_2 \,. \tag{2.1.10}$$

2.1.2 Pulse pile-up probability

In order to find the mathematical expression of $\partial\overline{P}/\partial E$ it is possible to adapt, to our case, the method proposed in [77] for finding PPU probabilities. Assuming the generation of pulses as a Poisson's process, the probability that n uncorrelated events (generations) occur in the time distance, from 0 to t, is:

$$P_n(t) = \frac{(\lambda t)^n}{n!} \mathrm{e}^{-\lambda t} \,. \tag{2.1.11}$$

where λ is the original counting rate not affected by PPU. Considering two pulses, with energies E_1 and E_2, one generated at $t = 0$ and the other generated in $[t_1, t_1 + dt_1]$ with $t_1 < \tau$:

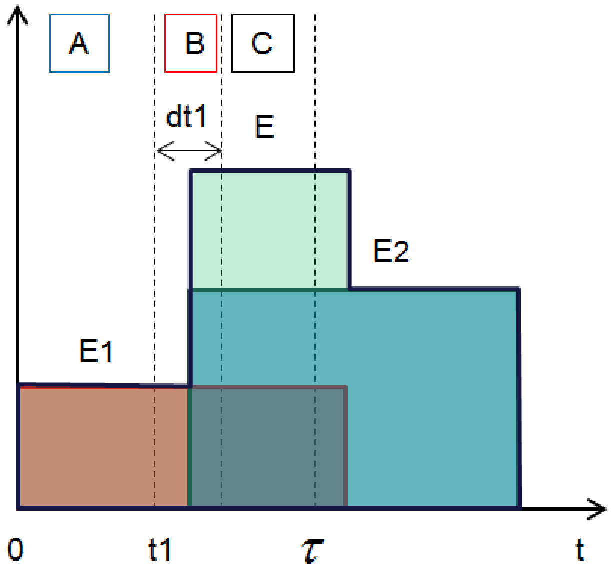

Figure 2.5: Pile-up between two rectangular pulses with energies E_1 and E_2 and a time gap $t_1 + dt_1$. The resulting pulse is still rectangular with energy E.

Following the Bayes theorem we can define the differential probability that two pulses are piled-up together as the product of three separated probabilities:

$$d\overline{P} = P_0(t_1)P_1(dt_1)P_0(\tau - t_1 - dt_1) \,, \tag{2.1.12}$$

where using the Poisson formula we have:

$$P_0(t_1) = \mathrm{e}^{-\lambda t_1} \ , \tag{2.1.13}$$

$$P_1(dt_1) = \lambda dt_1 \mathrm{e}^{-\lambda dt_1} = \lambda dt_1 \ , \tag{2.1.14}$$

$$P_0(\tau - t_1 - dt_1) = \mathrm{e}^{-\lambda(\tau - t_1 - dt_1)} = \mathrm{e}^{-\lambda(\tau - t_1)} \ . \tag{2.1.15}$$

Inserting Eqs.(2.1.13), (2.1.14) and (2.1.15) in Eq.(2.1.12) we obtain:

$$d\overline{P} = \lambda \mathrm{e}^{-\lambda\tau} dt_1 \ , \tag{2.1.16}$$

Integrating Eq.(2.1.16) between 0 and τ we obtain the total probability of having pile-up of order 2:

$$\overline{P} = \lambda \mathrm{e}^{-\lambda\tau} \tau \ . \tag{2.1.17}$$

As reported in [77] [80] t_1 is directly correlated to the energy of the resulting pulse. Calling $f(t)$ the pulse shape function, two pulses piled-up together will produce a new pulse with shape $\overline{f}(t)$:

$$\overline{f}(t) = E_1 f(t) + E_2 f(t - t_1) \ , \tag{2.1.18}$$

The energy of the resulting pulse, E, will be:

$$E = E_1 f(\bar{t}) + E_2 f(\bar{t} - t_1) \ , \tag{2.1.19}$$

where $\bar{t}$ is the time where $\overline{f}(t)$ reaches its maximum. It is possible to invert Eq.(2.1.19) for obtaining t_1 as functions of E_1, E_2 and the resulting pulse energy E. Differentiating t_1 considering only the resulting pulse energy E, i.e. $dt_1 = (\partial t_1 / \partial E)\, dE$, we have:

$$d\overline{P} = \lambda \mathrm{e}^{-\lambda\tau} \frac{\partial t_1}{\partial E} dE \ . \tag{2.1.20}$$

2.1.3 PPU balance equation for rectangular pulses

Eqns.(2.1.17) and (2.1.20) can be used to generate the balance equation for a generic pulse shape. In particular, for a rectangular pulse shape the energy of the resulting pulse from PPU is:

$$E = E_1 + E_2 \quad \forall \Delta t_1 \in (0, \tau) \quad , \tag{2.1.21}$$

This allows us to write:

$$\frac{\partial t_1}{\partial E} = \tau \delta[E - (E_1 + E_2)] \ . \tag{2.1.22}$$

$$d\overline{P} = \lambda \tau \mathrm{e}^{-\lambda\tau} \delta[E - (E_1 + E_2)] dE \ . \tag{2.1.23}$$

By replacing Eqs.(2.1.17) and (2.1.23) in Eq.(2.1.10) we obtain the following nonlinear balance equation:

$$\omega(E) = a\overline{h}(E) + b \int_{E_{\min}}^{E\max} \overline{h}(E_1)\overline{h}(E - E_1)dE_1 \ . \tag{2.1.24}$$

where $\omega(E) = y(E)/N_t$, $b = \lambda\tau \mathrm{e}^{-\lambda\tau}$ and $a = 1 - 2b$. This equation is valid either for paralyzable and nonparalyzable detector models because paralyzabilty affects only higher orders of PPU.

In order to test Eq.(2.1.24), we can consider for example a monochromatic normalized original spectrum, $\overline{h}(E) = \delta(E - \overline{E})$. Then, Eq.19 becomes:

$$\omega(E) \ = \ a\delta(E - \overline{E}) + b\delta(E - 2\overline{E}) \ . \tag{2.1.25}$$

which integrated for all the energies of the spectrum gives:

$$M_t \ = \ N_t[1 - \lambda\tau \mathrm{e}^{-\lambda\tau}] \tag{2.1.26}$$

with M_t representing the total number of counts of the measured spectrum. As reported in [76] considering the live time t_m we have the measured counting rate λ_m:

$$\lambda_m = \frac{M_t}{t_m} = \lambda[1 - \lambda\tau \mathrm{e}^{-\lambda\tau}] \tag{2.1.27}$$

Using Eq. (2.1.5) we obtain the well-known expression:

$$\lambda_m = \lambda[1 - \tau\lambda_m] \tag{2.1.28}$$

which allows to find N_t and the original counting rate λ and from λ_m, τ and t_m.

It is possible also to test the stability of Eq.(2.1.24) supposing to have a corrected spectrum perturbed by a limited function:

$$\overline{h}(E) = x(E) + \beta \sin(n\beta E) \ \ for \ \ n = 1, 2, ... \tag{2.1.29}$$

substituting this expression in Eq. 2.1.24 we obtain:

$$\begin{aligned}\omega(E) \ = \ & a\left[x(E) + \beta\sin(n\beta E)\right] + b\int_{E_{min}}^{Emax} \left[x(E_1) + \beta\sin(n\beta E_1)\right] \\ & \times\{x(E - E_1) + \beta\sin[n\beta(E - E_1)]\}dE_1 \ .\end{aligned} \tag{2.1.30}$$

which becomes:

$$\begin{aligned}\omega(E) \;=\; & a\,x(E) + b\int\limits_{E_{min}}^{Emax} x(E_1)x(E-E_1)dE_1 + a\,\beta\sin(n\beta E) + \\ & +b\int\limits_{E_{min}}^{Emax} x(E_1)\beta\sin[n\beta(E-E_1)]dE_1 + \\ & +b\int\limits_{E_{min}}^{Emax} \beta\sin(n\beta E_1)x(E-E_1)dE_1 + \\ & +b\int\limits_{E_{min}}^{Emax} \beta\sin(n\beta E_1)\beta\sin[n\beta(E-E_1)]dE_1\;. \end{aligned} \tag{2.1.31}$$

calling:

$$\omega_{unp.}(E) \;=\; a\,x(E) + b\int\limits_{E_{min}}^{Emax} x(E_1)x(E-E_1)dE_1\;, \tag{2.1.32}$$

it is obtained:

$$\begin{aligned}\omega(E) \;=\; & \omega_{unp.}(E) + a\,\beta\sin(n\beta E) \\ & +b\int\limits_{E_{min}}^{Emax} x(E_1)\beta\sin[n\beta(E-E_1)]dE_1 + b\int\limits_{E_{min}}^{Emax} \beta\sin(n\beta E_1)x(E-E_1)dE_1 \\ & +b\int\limits_{E_{min}}^{Emax} \beta\sin(n\beta E_1)\beta\sin[n\beta(E-E_1)]dE_1\;. \end{aligned} \tag{2.1.33}$$

considering that:

$$\sin(n\beta E_1)\sin[n\beta(E-E_1)] = \frac{1}{2}\{\cos[n\beta(2E_1-E)] - \cos(n\beta E)\} \tag{2.1.34}$$

we have:

$$\begin{aligned}\omega(E) \;=\; & \omega_{unp.}(E) + a\,\beta\sin(n\beta E) + b\int\limits_{E_{min}}^{Emax} x(E_1)\beta\sin[n\beta(E-E_1)]dE_1 + \\ & +b\int\limits_{E_{min}}^{Emax} \beta\sin(n\beta E_1)x(E-E_1)dE_1 + \frac{b\beta^2}{2}\left\{\frac{1}{2n\beta}\left[\sin(n\beta(2E_{max}-E))\right.\right. \\ & \left.\left. -\sin(n\beta(2E_{min}-E))\right] - \cos(n\beta E)(E_{max}-E_{min})\right\}\;. \end{aligned} \tag{2.1.35}$$

From the Riemann Lebesque theorem [81] we can see that, for $n >> 1$:

$$\omega(E) \; = \omega_{unp.}(E) + a\,\beta\sin(n\beta E) - \frac{b\beta^2}{2}\cos(n\beta E)(E_{max} - E_{min}) \; . \qquad (2.1.36)$$

The problem is always stable.

2.1.4 Iterative method for solving order two PPU balance equation

In what follows it will be shown that the solution of Eq.(2.1.24) can be found by computing iteratively:

$$\omega(E) = -a\,x^{(i)}(E) + b\int\limits_{E_{min}}^{Emax} x^{(i)}(E_1)x^{(i-1)}(E - E_1)dE_1 \quad i = 1, 2..., n \; , \qquad (2.1.37)$$

with the condition:

$$x^{(0)}(E) = \omega(E) \; . \qquad (2.1.38)$$

To find the solution of Eq.(2.1.24), let us compute its Laplace transform::

$$\overline{y}(s) = a\,\overline{h}(s) + b\,\overline{h}(s)^2 \; . \qquad (2.1.39)$$

One solution of this equation can be written as a continued fraction:

$$\overline{h}(s) = -\frac{a}{b} + \frac{1}{b}\frac{\overline{y}(s)}{\overline{h}(s)} \; . \qquad (2.1.40)$$

which becomes:

$$\overline{h}(s) = -\frac{a}{b} + \cfrac{\overline{y}(s)}{-a + \cfrac{\overline{y}(s)}{-\frac{a}{b} + \cfrac{\overline{y}(s)}{-a + \cfrac{\overline{y}(s)}{\cdots}}}} \; . \qquad (2.1.41)$$

The term with the continued fraction in Eq.(2.1.41) can be obtained from the following iterative equation:

$$\omega(s) = -a\,x^{(i)}(s) + bx^{(i)}(s)x^{(i-1)}(s) \quad i = 1, 2..., n \; , \qquad (2.1.42)$$

with $x^{(0)}(s) = \omega(s)$. Then, $x^{(1)}(s)$ becomes:

$$x^{(1)}(s) = \frac{\omega(s)}{-a + b\,\omega(s)} \; . \qquad (2.1.43)$$

and similarly we find the subsequent $x^{(2)}(s)$, $x^{(3)}(s)$,, $x^{(n)}(s)$ in the Laplace domain:

$$\lim_{n\to\infty} x^{(n)}(s) = \cfrac{\omega(s)}{-a + \cfrac{\omega(s)}{-\frac{a}{b} + \cfrac{\omega(s)}{-a + \cfrac{\omega(s)}{\cdots}}}} \,. \tag{2.1.44}$$

The difference between Eq.(2.1.41) and (2.1.44) is only the constant term which antitransformed gives a delta in the zero energy which is not relevant. Then we find Eq.(2.1.37) by antitransforming Eq.(2.1.42).

Let us considering the discretization of Eq.(2.1.37) in N energy bins:

$$\omega_j = -a\, x_j^{(i)} + b \sum_{k=1}^{j} x_k^{(i)} x_{j-k}^{(i-1)} \,. \tag{2.1.45}$$

Each iteration of Eq.(2.1.45) requires the solution of a numerical system:

$$\vec{\omega} = \mathbf{P}\vec{x}^{(i)} \tag{2.1.46}$$

Where the matrix P can be expressed using the step and Kronecker functions $H(j-k)$ and $\delta_{j,k}$:

$$P_{j,k} = -a\,\delta_{j,k} + b x_{j-k}^{(i-1)} H(j-k) \tag{2.1.47}$$

The coefficients a and b allows the diagonal dominance, so for each iteration a SOR (successive over relaxation) method can be implemented.

The algorithm used for implementing the deterministic strategy of this work can be summarized as follows:

(1) Read the input data: τ, y, t_m.

(2) compute the integrated spectrum: $M_t = \sum_{i=1}^{N} y_i$

(3) compute the the measured emission rate: $\lambda_m = M_t/t_m$

(4) compute the true emission rate: $\lambda = \lambda_m/(1-\tau\lambda_m)$

(5) compute: $b = \lambda\tau \mathrm{e}^{-\lambda\tau}$

(6) compute: $a = 1 - 2b$

(7) compute the integrated original spectrum: $N_t = M_t/(1-b)$

(8) compute: $\omega_j = y_j/N_t \;\; for \;\; j = 1, 2, ..., N$

(9) initialize: $x_j^{(0)} = \omega_j \;\; for \;\; j = 1, 2, ..., N$

(10) for $i = 1, n$ (n is the total number of iteration chosen equal to 5)

  (a) Initialize: $P_{jk} = 0$

```
    (b) for $j = 1, N$
        (I) set: $P_{jj} = a$
        (II) for $k = 1, N$
            ($\alpha$) if $j \geq k$ then
                ($a$) set: $l = j - k + 1$
                ($b$) compute: $P_{jk} = P_{jk} + bx_l^{(i-1)}$
            ($\beta$) end if.
        (IV) end for.
    (c) end for
    (d) Introduce SOR relaxation factor $\Omega$ (used $\Omega = 1.7$)
    (e) initialize $z_j = 0 \;\; for \;\; j = 0, 1, ..., N$
    (f) initialize $z_j^0 = x_j^{(i-1)} \;\; for \;\; j = 0, 1, ..., N$
    (g) for $l = 1, nsor$ ($nsor$ max iterations of the SOR routine, chosen equal to 30)
        (I)for $j = 1, N$
            ($\alpha$) $sum\_row = 0$
            ($\beta$) for $k = 1, j - 1$
                ($a$) $sum\_row = sum\_row + P_{jk} z_k$
            ($\gamma$) end for
            ($\delta$) for $k = j + 1, N$
                ($a$) $sum\_row = sum\_row + P_{jk} z_k^0$
            ($\epsilon$) end for
            ($\zeta$) $sum\_row = (\omega_j - sum\_row)/P_{jj}$
            ($\eta$) $z_j = z_j^0 + \omega_j (sum\_row - z_j^0)$
        (II) end for
        (III) $z_j^0 = z_j \;\; for \;\; j = 1, ..., N$
    (h) end for
    (i) $x_j^{(i)} = z_j \;\; j = 1, ..., N$
(11) end for
(12) $h_j = -N_t x_j^{(n)} \;\; for \;\; j = 1, ..., N$
```

2.1.5 Si detector application

It is possible to show now some examples with a Si SSD detector using XRF experimental spectra of different samples collected at the Laboratory of Montecuccolino. For all the measures, the X-ray source is a Hamamatsu X-ray tube operated at 35 kV and the detector is a Si SSD XR-100CR from Amptek, used without collimator. The scattering angle is 90 degrees.

Two different target materials are used: pure lead and tin alloy. The live time for each measure is 600 seconds and the dead time was estimated using MCPPU giving a value of 2.5 μs considering the rise time discriminator (RTD) active. For each sample, both a High counting rate (HCR) and a low counting rate (LCR) measure are acquired, with the RTD and the rejection circuitry both active.

Figures 2.6-a and 2.6-b show the results for the lead sample. In figure 2.6 the peaks in channels 200-300 correspond to the Pb L-lines. The four peaks in channels 400-600, in the HCR spectrum, do not correspond to any X-ray line, therefore it can be assumed that they are due to PPU. Figure 2.6-b shows the comparison with the LCR spectrum and makes it clear that the PPU effects have been recognized and corrected. From the figure it is possible to note the presence of numerical artefacts appearing in the region where PPU is higher. These artefacts are due to the statistical fluctuations combined with the influence of the detector energy calibration and the MCA discretization in energy, unfortunately they cannot be avoided because are independent from the calculation.

Analogous considerations can be done for the tin alloy spectrum in fig.2.7. In the HCR measure, it is apparent the presence of photons above the excitation energy of the X-ray source (channels 700-1024). These peaks are clearly due to PPU. For these two examples it was necessary to compute only five iterations. Each iteration took few seconds (on a Windows 7-64 AMD Athlon$^{\text{TM}}$ II X4 640 @3.0 GHz).

2.1.6 Monte Carlo method for pulse pile-up

In the previous section it was showed a deterministic approach to PPU correction which can be applied to a limited experimental cases. It is possible to generalize this approach taking into account the real detector pulse shape and all PPU orders following the same concept schema showed before. However this procedure leads to an extremely hard mathematical problem without fast solution. In order to avoid these difficulties it is possible to consider a statistical approach using the Monte Carlo method (MC).

The MC, applied to PPU correction, allows to consider not only the real pulse shape of the detector, but also all PPU orders without an excessively increase of the computation difficulty. This approach was investigated in the works [79], [82], [83] and [84]. Based on the MC algorithm developed in [83] and [84] during this PhD course it was developed the code MCPPU [3] which allows to perform pulse pile-up correction of spectra adaptable to different detectors.

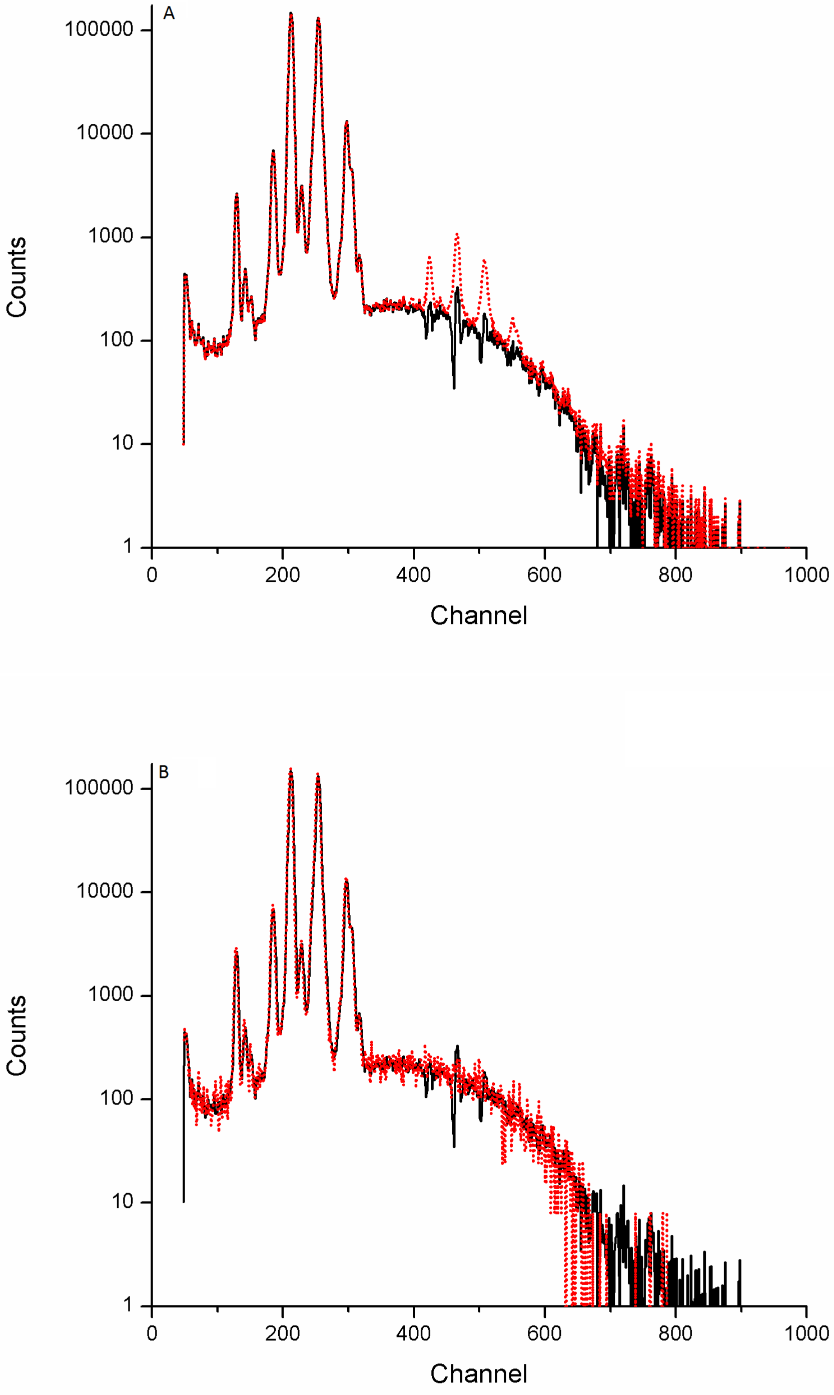

Figure 2.6: PPU correction for a sample of pure Lead considering a Si SSD with RTD active. (a) high counting rate measure (dots) together with the original spectrum (line). (b) Comparison between the original spectrum (line) and a scaled low counting rate spectrum (dots).

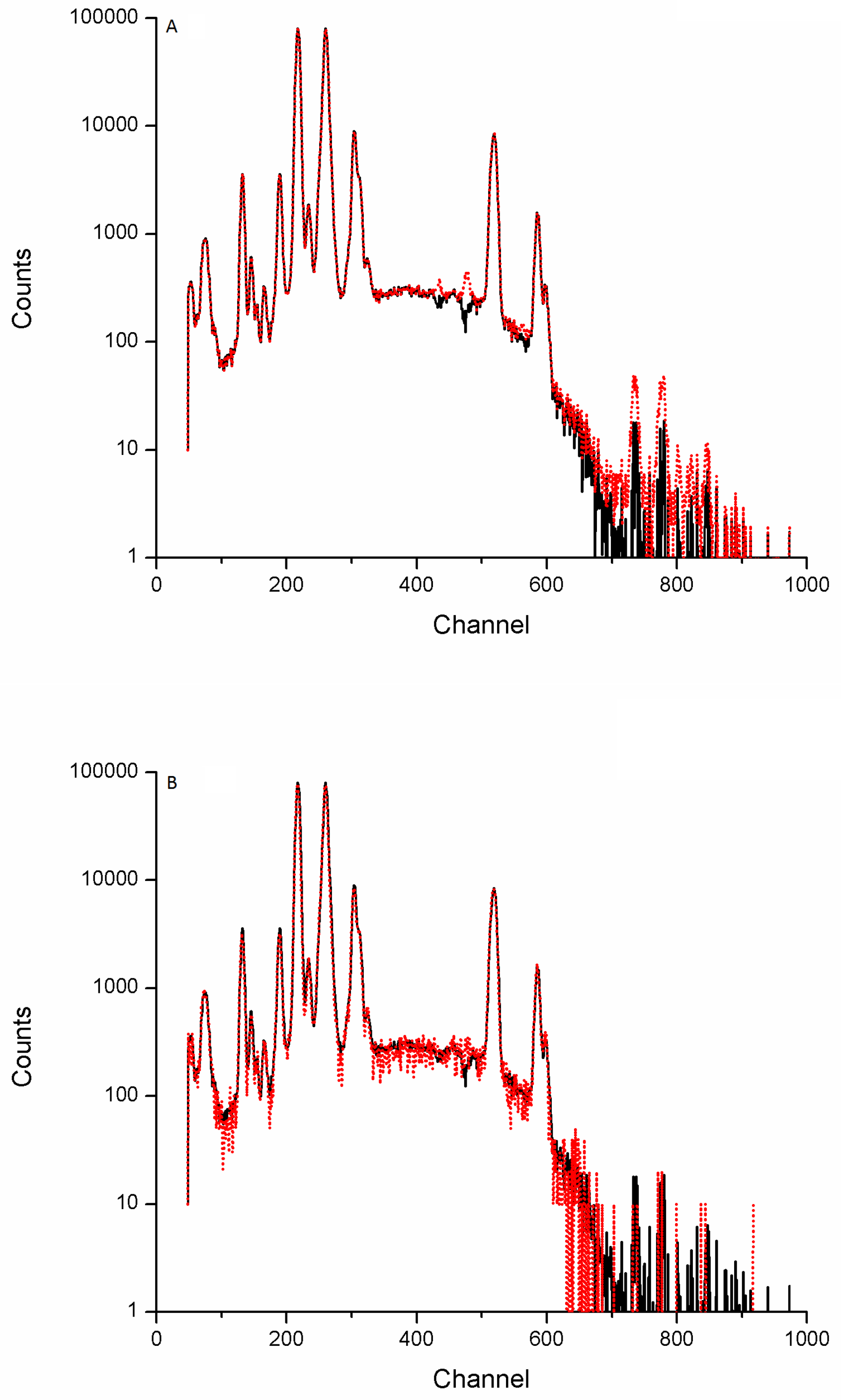

Figure 2.7: PPU correction for a sample of Tin alloy considering a Si SSD: (a) high counting rate measure (dots) together with the original spectrum (line). (b) Comparison between the original spectrum (line) and a scaled low counting rate spectrum (dots).

The core of the method can be represented by two sampling process:

1) Sampling the channel of all the recorded pulses in a measured spectrum,

2) Sampling the time gap which separates the production of two different pulses.

It is possible to compute the probability of having two pulses separated by a certain time gap using the Poisson formula in Eq.(2.1.11). Assuming one pulse fixed at $t = 0$ and the second one at $t = t_1 + dt_1$ the differential probability of having a time gap of $t_1 + dt_1$ is:

$$dP(t_1) = P_0(t_1)P_1(dt_1) = \lambda \mathrm{e}^{-\lambda t_1} dt_1 \quad . \tag{2.1.48}$$

Integrating between 0 and Δt we find the probability of having two pulses with a time gap Δt:

$$P(\Delta t) = \int_0^{\Delta t} \lambda \mathrm{e}^{-\lambda t_1} dt_1 = 1 - \mathrm{e}^{-\lambda \Delta t} \quad . \tag{2.1.49}$$

It is possible to sample Δt using a random number ξ uniformly distributed in $[0, 1]$:

$$1 - \mathrm{e}^{-\lambda \Delta t} = \xi \quad , \tag{2.1.50}$$

which leads to:

$$\Delta t = -\frac{\log(1 - \xi)}{\lambda} \equiv -\frac{\log(\xi)}{\lambda} \quad . \tag{2.1.51}$$

Using a reference spectrum h, it is possible to sample the channel j of the pulse (which is directly connected to its heigh) using another random number ξ_1 with the same properties of ξ:

$$\sum_{i=1}^{j} h_i = \xi_1 \quad , \tag{2.1.52}$$

Inverting this equation it is obtained the channel of the pulse as a function of the random number.

The MC method can be implemented initializing a first pulse at the time $t = 0$ in a sampled channel. Then a second pulse channel and the time gap Δt are sampled. If $\Delta t < \tau$ the two pulses are summed, obtaining a new pulse in a new channel. The process is continued, keeping in memory the piled-up pulses of the previous step, sampling another pulse channel and a new time gap $\Delta t'$. If $\Delta t' < \tau$ the pulse will be summed to the piled-up pulses of the previous step and they will be kept in memory. The summation is stopped when the time gap is greater then τ. In this case the piled-up pulses are stored as a single pulse in the resulting channel. After that a new pulse train is sampled until all the pulses of the measure are considered.

It is evident that the choice of h is of primary importance for the channel sampling. There are two possible choices for h:

1) A low counting rate spectrum (LCR) [82].

2) The measure itself [83] [84].

The first strategy implies long low counting rate measurements for obtaining a LCR spectrum with an acceptable statistics. Moreover long measurements can overheat the detector changing the operational condition. It is worth nothing that the dead time is extremely sensible to the operational conditions [76]. The change of these conditions can greatly modify the referenced dead time making it bigger and increasing PPU effect. This is one of the most important reason for avoiding this choice.

The second strategy implies the construction of an iterative procedure where the spectrum used for the channel sampling is, in each iteration, updated starting from the measure until it reaches the original spectrum, solution of the problem. In what follows it will be discussed this strategy which is implemented in the code MCPPU [3].

2.1.7 The code MCPPU

The MC strategy described in the previous section was implemented in the post-processing code MCPPU [3] (Monte Carlo Pulse Pile-Up) developed during this PhD course.

The code implements a robust procedure for PPU correction capable to be applied to any kind of detector-amplifier combination. It is well known that this combination and the use of PPU suppression circuitry concurs to produce the final pulse shape [76] [80]. Thus, it is difficult that simple analytical shapes may describe properly the real shape of the pulse. For this reason MCPPU allows the user to insert an external text file with the digitized measured pulse shape, as collected from the pulse handling circuitry. The pulse shape needs to be normalized and discretized in a vector in which each component represents the value at a time step of 1μs.

MCPPU is also capable to give an estimation of the dead time using both high and low counting rate measures.

The MCPPU algorithm can be described as follows:

(1) Read the input data: τ, the measure y, the discretized pulse shape in the vector D, the live time t_m.

(2) Set $h_i^0 = y_i \;\; for \;\; i = 1, 2, ..., N$ (where N is the total number of channels in the measure)

(3) for $m = 1, max_it$ (external iteration cycle)

  (a) compute the total number of counts $N_t = \sum_{i=1}^{N} h_i^{(m-1)}$

  (b)compute $\lambda = N_t/t_m$

  (c) compute the Cumulative Distribution Function (CDF):

  $$C_j = \sum_{i=1}^{j} h_i^{(m-1)} \;\; for \;\; j = 1, 2, ..., N$$

  (d) sample the channel of a first pulse solving $C_{j^{(0)}} = \xi_1$

```
    (e) set $D_i^{(0)} = D_i \;\; for \;\; i = 1, 2, ..., N_{max}$ (where $N_{max}$ is the size of the vector $D$ allowed)
    (f) for $n = 1, N_t$
        (I) sample the energy of a new pulse $C_j = \xi_1$
        (II)sample the time gap: $\Delta t = -\frac{\log(\xi)}{\lambda}$
        (III)if $\Delta t < \tau$ then:
            ($\alpha$)compute $l = int(\Delta t * 10^6)$
            ($\beta$) set $D_\alpha^{(n)} = \begin{cases} 0 & if \; \alpha < l \\ D_{\alpha-l+1}^{(0)} & if \; \alpha \geq l \end{cases}$
            ($\gamma$)compute the pile-up pulse shape $D_\alpha^{(n)} = j^{(n-1)} D_\alpha^{(n-1)} + j D_\alpha^{(n)}$
            ($\delta$)compute $j^{(n)}$ searching the maximum value of $D^{(n)}$
            ($\epsilon$) Update recovery spectrum $R_j = R_j + 1$
            ($\zeta$) set $PPU = .TRUE.$ (PPU flag)
        (IV) else:
            ($\alpha$)if (PPU) update pile-up spectrum $P_{j^{(n-1)}} = P_{j^{(n-1)}} + 1$
            ($\beta$)if (PPU) update the measure simulation spectrum $S_{j^{(n-1)}} = S_{j^{(n-1)}} + 1$
            ($\gamma$)update $S_j = S_j + 1$
            ($\delta$)set $j^{(n)} = j$
            ($\epsilon$)set $PPU = .FALSE.$
        (IV)end if
    (g) end for (inner cycle)
    (h) compute $h^{(m)} = y - P + R$
    (i) compute $\chi^2 = \frac{1}{N} \sum_{i=1}^{N} \frac{(y_i - S_i)^2}{y_i}$
    (j) if $\chi^2 \leq toll$ then exit
(4) end for
```

From the algorithm it is evident that each iteration increases the total number of pulses (counts) in the corrected spectrum, since the recovered pulses are always at least twice the number of pile-up pulses.

The evaluation of the dead time of the counting system is mandatory for having a good PPU correction. In MCPPU the dead time is evaluated using a HCR spectrum and a LCR spectrum without the need of additional experimental devices as requested in [85] and [76]. Firstly, the user inserts the dead time starting value and the dead time increment, and the number of iterations. Then the pile-up correction is calculated for all the dead time values in the selected range with the given dead time increment and the result of each computation is stored. MCPPU compares automatically the corrected spectrum resulting from each calculation, with the given LCR measure. The dead time which gives the spectrum minimizing the chi-square is selected.

$$\chi^2 = \frac{1}{N}\sum_{i=1}^{N}\frac{(L_i - h_i)^2}{L_i}, \tag{2.1.53}$$

where in Eq.(2.1.53) L_i is the low rate spectrum. The presented dead time calculation operates well also in the presence of rejection circuitry for PPU suppression and needs to be performed only once for given conditions of acquisition.

2.1.8 Si application of MCPPU

In order to test the correctness of MCPPU results it is here replicated the correction of PPU for a Lead and tin alloy showed in the preivous sections.

The method was tested successfully with Si SSD obtaining the same results obtained with the deterministic methodology using the digitalized pulse shape of the detector. The presence in the results of both MCPPU and deterministic strategies of the same numerical artifacts shows that they are not influenced by the Monte Carlo statistics and they are due to the statistical fluctuation with the combined influence of the detector energy calibration and the MCA discretization in energy, and cannot be avoided.

The choice between the two proposed approaches depends on the characteristics of the detector. It has to be preferred the deterministic approach (when the hypothesis of the method are compatible with the detector) because it is simpler to be used and faster.

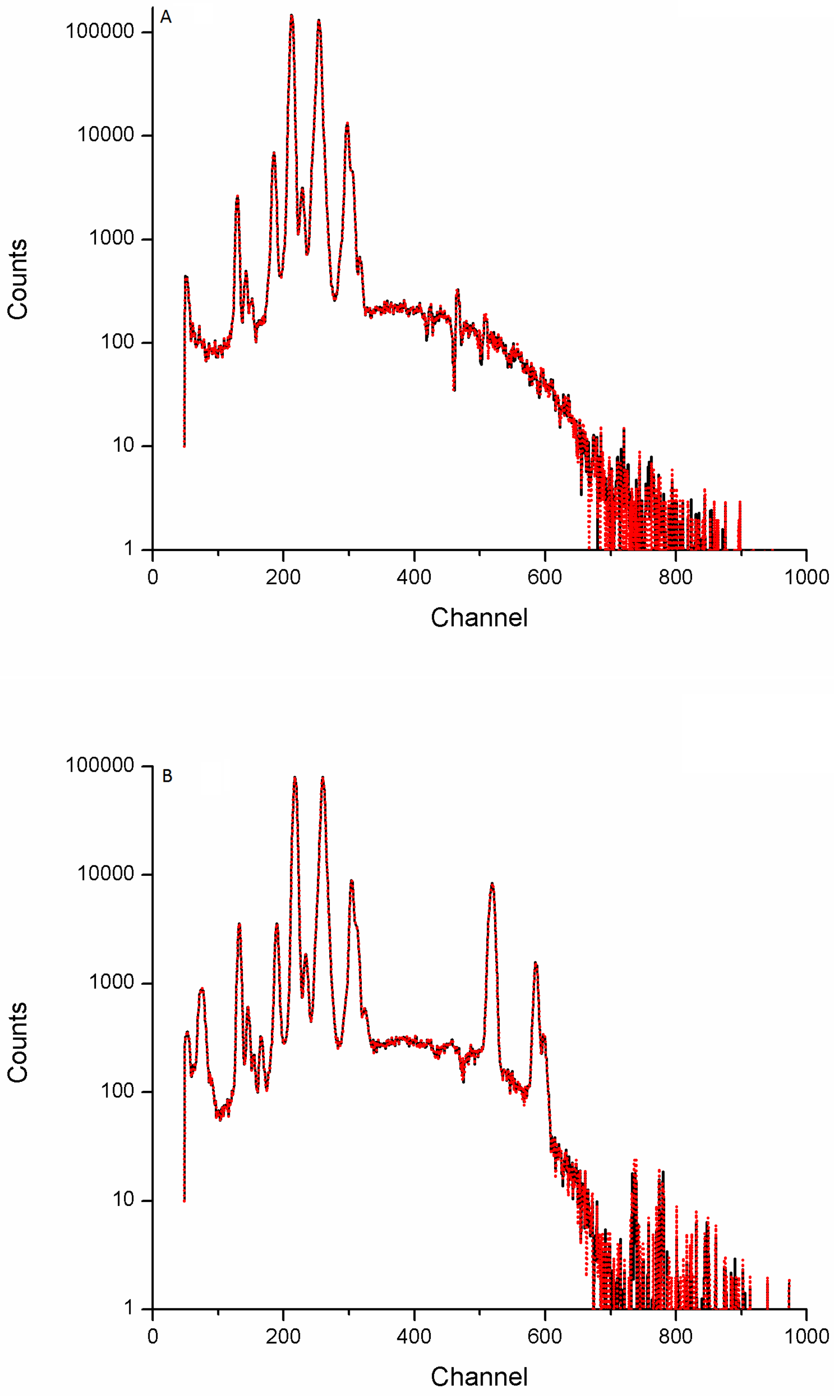

Figure 2.8: PPU correction comparison between deterministic method (dots) and MC one (line) for a sample of: (a) Lead target. (b) Tin alloy target. The detector used is the one described in sec. 2.1.5

2.2 Detector Response function

Pulse pile-up correction described in the previous section can not be sufficient for recovering the scattered spectrum (see fig.(2.1)). The second step to follow is the unfolding from the detector response function (DRF) which represents an almost complete description of the detector effects on a measure.

DRF for X- and Gamma-ray detectors can be formalized as a convolution of three fundamental contributions, each one referred to a different physical process inside the detector.

1) The energy deposition spectrum, which is the distribution of the amount of energy absorbed by the detector.

2) The detector resolution function, which represents the smearing effect of the detector on the measure.

3) The detector efficiency, which gives an estimation of the amount of radiation not absorbed by the detector for each energy bin.

The energy deposition spectrum depends on the physical properties of the detector (such as, composition, thickness, geometry, etc.). It represents the result of the radiation transport inside the detector, which can be described by the principal interaction mechanism between radiation and matter: Compton, Rayleigh and Photoelectric effects.

Inside the detector active media (for example a semiconductor crystal) a photon has to be completely absorbed in order to produce a pulse of heigh proportional to the photon energy. When photon absorption is due to Scattering (Rayleigh or Compton) or photoeffect nearby the boundary surfaces, of the active media, only a part of the photon energy may be actually absorbed. Photoelectric effect, Compton and Rayleigh scattering produce a new photon which can escape from the boundary surfaces of the detector. There are several consequences of these incomplete photon absorption on the measured spectra. For photoelectric effect the partial absorbed energy is related to the characteristics lines of the active media, generating the so called escape peaks. For Compton scattering it is produced a continuous spectrum (Compton escape) below the excitation energy. This effect is due to the dependence between the energy of the resulting pulse and the scattering angle. For Rayleigh scattering there is no energy absorption (coherent scattering) and the photon is completely lost. However this effect can be taken into account in the energy deposition spectrum considering a contribution at the zero energy. The energy deposition spectrum can be computed by using deterministic or MC codes. In this work they will be computed using MC codes such as PENELOPE [27] and MCSHAPE [86].

Regarding the energy resolution it depends specifically on the detection mechanism which is characteristic of the single detector. In a first approximation, the energy resolution can be modelled using a normalized Gaussian distribution having its full width at half maximum (FWHM) expressed in terms of specific semi-empirical formulas for semiconductors detectors (solid-state detectors), scintillators and gas proportional counters. However, this approach is not sufficient with some SSD. It is frequent to find that the peaks show a deviation from the Gaussian shape: a long flat shelf structure from the peak centroid to the lower energies, and an asymmetry in the Gaussian which can be described with an exponential decay on the left side of the peak. Some authors [87] [88] attribute these artifacts to incomplete charge collection (like carrier trapping and charge escape). Other authors show that the interactions between the metal contact and the detector material produce a low energy shelf structure, with defined steps [89]. Papp [90] points out the effect of the signal processing electronics on the evolution of the electronic signal and, from the details of the electron transport processes, proposes an approximate analytical function to describe the detector response. The line shape can be modeled with analytical [91] or semi-empirical formulas [88] [87] [92]. Among them, the so-called HYPERMET [87] function represents a general semi-empirical formula which was initially proposed for describing the line-shape of a Ge detector. Campbell et al [88] tested the HYPERMET function also in the case of Si(Li) detectors with satisfactory results. Usually, the HYPERMET function is fitted to a given measured spectrum. In the present work the energy resolution will be computed using the Gaussian model and an adaptation of the HYPERMET model which are implemented in the graphical tool RESOLUTION [86] [4].

Finally regarding the detector efficiency, as the energy deposition spectrum, it can be both empirically measured or computed using deterministic or MC codes.

In what follows it will be discussed both the theoretical model for the DRF and its computation through the new version of the software RESOLUTION [4] which was developed during this PhD course by an older version done by the research group of Prof. J.E. Fernandez [86]. The application of RESOLUTION will be explained with some examples using commercial solid state detectors.

2.2.1 Theoretical model

In what follows it is assumed a measured spectrum I_m corrected from pulse handling circuit effects. The scattered spectrum I, i.e. original spectrum, can be related to the measured one through an integral equation [86] [93]:

$$I_m(E) = \int \mathcal{K}(E', E) I(E') dE', \tag{2.2.54}$$

where $\mathcal{K}(E', E)$ is the DRF. It is possible to rewrite the DRF as:

$$\mathcal{K}(E', E) = R(E', E)\phi(E'), \tag{2.2.55}$$

where $R(E', E)$ represents the contribution of both the energy deposition spectrum and the energy resolution. The other function $\phi(E')$ is the detector efficiency. The function $R(E', E)$ is the convolution of the energy deposition spectrum $Q(E'', E_0)$ with the detector resolution function $G(E'', E)$:

$$R(E', E) = \int Q(E'', E')G(E'', E)dE''. \tag{2.2.56}$$

By replacing Eqn(2.2.56) in (2.2.54) and changing the order of integration, it is finally possible to write:

$$I_m(E) = \int S(E'')G(E'', E)dE'' \ , \qquad S(E'') = \int Q(E'', E')\phi(E')I(E')dE'. \tag{2.2.57}$$

When $I(E')$ is monochromatic the function $S(E'')$ depends only on the physical properties of the detector, such as geometry, composition, density, thickness, etc. and can be computed by means of deterministic or Monte Carlo codes.

Regarding the energy resolution it depends on the detector type and it does not present an ideal behaviour. Assuming that the formation of each energy carrier is a Poisson process and that the total number of carriers is high, the energy resolution due to the statistical noise can be represented, in a first approximation, by a Gaussian distribution:

$$\begin{aligned} G(E'', E) &= \frac{A}{\sigma\sqrt{2\pi}} \exp\left(-\frac{(E''-E)^2}{2\sigma^2}\right) \\ &= 0.939\frac{A}{\mathrm{FWHM}} \exp\left(-2.773\frac{(E''-E)^2}{\mathrm{FWHM}^2}\right), \end{aligned} \tag{2.2.58}$$

where FWHM is the full width at half maximum and $\sigma \cong \mathrm{FWHM}/2.355$. E and A represent the centroid and the peak area, respectively.

It is worth nothing that the FWHM, which is a function of the energy, is the most commonly used parameter for characterizing the energy resolution. It is possible to give a more applicative definition of the energy resolution as the FWHM of a single energy peak divided by the peak centroid, it is usually expressed as a percentage.

As reported in [76], there are different sources of fluctuation that result in imperfect energy resolution (a Dirac delta in the peak centre): a drift of the operational characteristics during the measure, the random noise and the statistical noise. The latter one depends on the discrete nature of the measurement itself: the energy deposited inside the detector is revealed by a discrete number of charge carriers which is subject to random fluctuations. It is also worth noting that the processes inside the detector are not independent and therefore the Poisson statistics is not valid. As a consequence, the resolution computed with purely statistical methods is much worse that the observed one and must be corrected by means of the so-called Fano factor F [94]. Any other source of fluctuations combines with the statistical noise. It can be proved that the overall energy resolution can be represented by a Gaussian function with FWHM given by [76]:

$$\mathrm{FWHM}_{\mathrm{overall}} = \sqrt{\mathrm{FWHM}_{\mathrm{statistical}} + \mathrm{FWHM}_{\mathrm{noise}} + \mathrm{FWHM}_{\mathrm{drift}} + \ldots}, \tag{2.2.59}$$

where $\text{FWHM}_{\text{statistical}}$ is the contribution due to statistical noise, $\text{FWHM}_{\text{noise}}$ is the one due to electronic noise and $\text{FWHM}_{\text{drift}}$ the one due to operational drift during the measure process.

Sometimes, in the particular case of SSD, the line shape can appear skewed with a long tail going from the peak centroid to the zero energy [87] [88]. In this case the Gaussian line profile should be corrected with proper models. As reported in [87] [88] charge carrier trapping and incomplete charge collection can subtract counts from the full energy peak by creating an exponential distribution below it:

$$T(i_0, i) = \begin{cases} H_D \exp\left(\frac{i_0 - i}{\alpha}\right) & i \leq i_0 \\ 0 & i > i_0 \end{cases}, \tag{2.2.60}$$

where i is the channel, i_0 the full energy line channel, α the exponential slope and H_D the amplitude of the tail. Charge collection mechanism and electronic noise can also introduce a flat continuous (plateau) going from the peak centroid to the zero energy [87] [88]:

$$M(i_0, i) = \begin{cases} H_S & i \leq i_0 \\ 0 & i > i_0 \end{cases}, \tag{2.2.61}$$

where H_S is the height of the plateau which contributes to produce the continuous part of the DRF. The exponential tail $T(i_0, i)$ and the plateau $M(i_0, i)$ can be considered as part of the energy deposition spectrum and must be included in the response function before applying the energy resolution. The convolution of $T(i_0, i)$ and $M(i_0, i)$ with the Gaussian distribution gives the tail and shelf function presented in literature as the HYPERMET functions [87] [88] [89] :

$$S(i_0, i) = \frac{1}{2} H_S \, erf\left(\frac{i - i_0}{\sigma\sqrt{2}}\right) \tag{2.2.62}$$

$$D(i_0, i) = \frac{1}{2} H_D \, \exp\left(\frac{i - i_0}{\alpha}\right) erf\left(\frac{i_0 - i}{\sigma\sqrt{2}} + \frac{\sigma}{\alpha\sqrt{2}}\right) \tag{2.2.63}$$

where σ is the standard deviation of the Gaussian distribution. fig. 2.9 shows the effect of the function $D(i_0, i)$ and $S(i_0, i)$ on a full energy line.

The parameters H_S, H_D and α, the so-called HYPERMET parameters, are all function of the energy. Among the several empirical models in literature to express these parameters, it was chosen to use a modification of the one that was proposed by Campbell et al [88]:

$$SF(E) = a_0 + a_1 \exp(a_2 E) \tag{2.2.64}$$

$$TF(E) = b_0 \exp(b_1 E) + b_2 \exp(b_3 E) \tag{2.2.65}$$

$$\beta(E) = c_0 + c_1 E + c_2 E^2 + c_3 E^3 \tag{2.2.66}$$

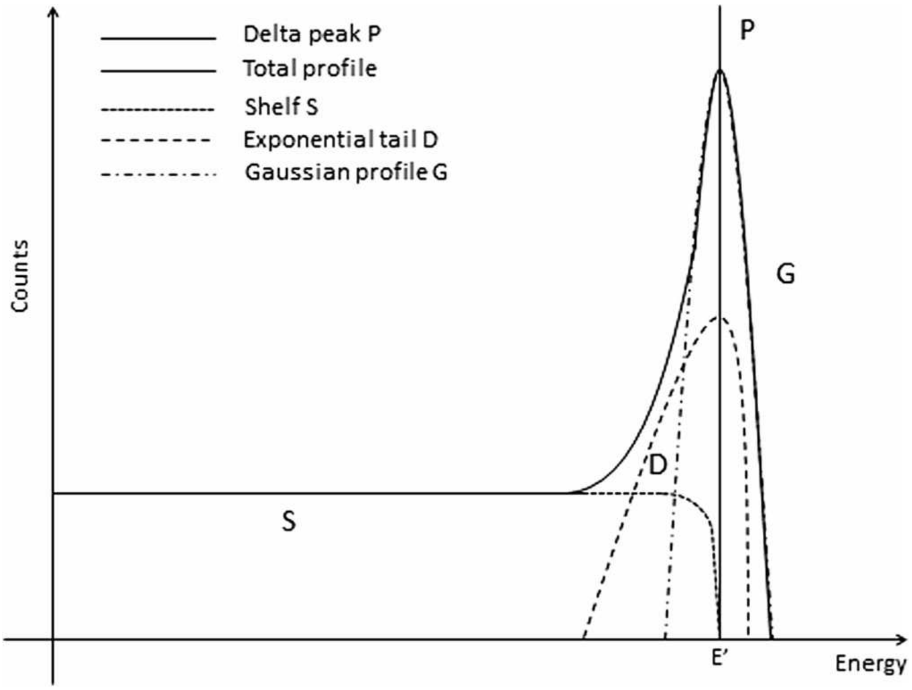

Figure 2.9: Qualitative representation of the different functions that concur to describe a single peak.

where SF (shelf fraction) and TF (tail fraction) are expressed as a function of the channel energy E; a_0, a_1, a_2, b_0, b_1, b_2, b_3, c_0, c_1, c_2 and c_3 are fitting parameters determined empirically for each detector. Once these functions have been estimated, the number of counts can be as follows. Under the full energy peak (at channel i_0) it becomes:

$$\tilde{H}(i_0) = H(i_0) - SFH(i_0) - TFH(i_0) \tag{2.2.67}$$

where $H(i_0)$ represents the total number of counts lost in the full energy peak that are uniformly distributed in $i_0 - 1$ channels below (uniform shelf distribution) and $TFH(i_0)$ represents the total number of counts lost in the full energy peak that forms the exponential tail. The counts lost by the full energy peak are distributed at lower energies. The generic bin below the full energy peak gains counts according to the expression:

$$\tilde{H}(i_0) = H(i_0) - \frac{SFH(i_0)}{i_0 - 1} - \frac{TFH(i_0)\exp\left(\frac{i}{\alpha}\right)}{\sum\limits_{i=1}^{i_0-1}\exp\left(\frac{i}{\alpha}\right)} \tag{2.2.68}$$

where $\alpha = \beta\sigma/\Delta E$, and σ is the standard deviation of the Gaussian distribution at the energy and the channel width. The chosen strategy, which is implemented in the new version of RESOLUTION, H_s and H_D of the HYPERMET functions are obtained from SF and TF by introducing the two corrective (normalization) factors:

$$H_S = \frac{SFH(i_0)}{i_0 - 1} \tag{2.2.69}$$

$$H_D = \frac{TFH(i_0)}{\sum\limits_{i=1}^{i_0-1} \exp\left(\frac{i}{\alpha}\right)} \tag{2.2.70}$$

2.2.2 The tool RESOLUTION

RESOLUTION is a software tool which adds the smearing effect of energy resolution and incomplete charge collection to simulated x- and gamma-ray spectra comprising the energy deposition spectrum in the detector. To model the energy resolution, the code, in a first approximation, redistributes in the energy E the counts collected in the channel energy E'' (referring to Eq.(2.2.58)) using a normalized Gaussian distribution whose FWHM, for each kind of detector, is given by the following expressions:

1. Gas proportional counters:

$$FWHM = \sqrt{W(F+\beta)E} \tag{2.2.71}$$

2. Solid state detectors:

$$FWHM = \sqrt{8\log(2)[WFE + aE^b] + \Delta E^2_{elec}} \tag{2.2.72}$$

3. Scintillators:

$$FWHM = \sqrt{c + dE} \tag{2.2.73}$$

The above formulas are taken from Knoll [76] for gas proportional counters and scintillators, and from Devanathan et al. [95] and Owens [96] for solid state detectors. W represents the average energy to produce a ion pair (in keV). Typical values of W are 2.96 eV for Ge and 3.62 eV for Si [96]. β is the parameter for the Polya distribution; a, b, c and a are semi-empirical constants and $\Delta E_{elec}$the electronic noise. F is the Fano factor. Different values for F can be found in literature: according to Papp et al [97] F is 0.06 for Ge and Si; Owens et al [98] suggest to adopt values greater than 0.10 for Si-detectors. However, as pointed out by Owens [96], in Eqn.(2.2.72), both F, a and b can be treated as fitting parameters. The RESOLUTION algorithm can be summarized as follows:

```
(1) Read the input parameter and the input spectrum $H$ with the energy of the bins $E$.
(2)Initialize the output spectrum $D$ to zero in each channel.
(3) If the detector is a SSD then:
    (a) For $k = 1, N$ ($N$ is the total number of channels of the input spectrum),
        (I) If $H(k) > 0$ then compute:
            ($\alpha$) $SF = a_0 + a_1\exp[a_2E(k)]$
            ($\beta$) If $SF > 0$ then:
```

```
                ($a$)$H_S = \frac{H(k)SF}{k-1}$
                ($b$) For $i = k-1, 1, -1$
                    (1) $H(i) = H(i) + HS$
                ($c$) End for
            ($\gamma$) else
                ($a$)$SF = 0$
            ($\delta$) End if
            ($\epsilon$) $FWHM = \sqrt{8\log(2)[WFE(k) + aE^b(k)] + \Delta E_{elec}^2}$
            ($\zeta$) $\sigma = \frac{FWHM}{2.355}$
            ($\eta$) $\beta = c_0 + c_1E + c_2E^2 + c_3E^3$
            ($\theta$) $\alpha = \frac{\beta\sigma}{\Delta E}$
            ($\iota$) $\epsilon = \sum_{i=1}^{k-1} \exp\left(\frac{i}{\alpha}\right)$
            ($\kappa$) $TF = b_0\exp[b_1E(k)] + b_2\exp[b_3E(k)]$
            ($\lambda$) If $TF > 0$ then compute:
                (a) $H_D = \frac{H(k)TF}{\epsilon}$
                (b) If $H_D > 0$ then:
                    (1) For $i = k-1, 1, -1$
                        ($I$) $H(i) = H(i) + H_D\exp\left(\frac{i}{\alpha}\right)$
                    (2) End for
                (c) End if
            ($\mu$) else
                (a) $TF = 0$
            ($\nu$) End if.
            ($\xi$) $H(k) = H(k) - SFH(k) - TFH(k)$.
        (II) End If
    (b) End For
(4) End IF
(5) For $m = 1, N$
    (a) if the detector is SSD then:
        (I) $FWHM = \sqrt{8\log(2)[WFE(m) + aE^b(m)] + \Delta E_{elec}^2}$
    (b) Else if the detector is a scintillator then:
```

```
        (I) $FWHM = \sqrt{a + bE(m)}$
    (c) Else if the detector is a Gas proportional counter then:
        (I) $FWHM = \sqrt{W(F + \beta)E(m)}$
    (d) End If
    (e) For $j = 1, N$
        (I) $D(j) = D(j) + H(m)\frac{2.355}{2\pi FWHM[E(m)]}\exp\left[-\frac{2.355^2}{2}\frac{[E(m)-E(j)]^2}{FWHM^2[E(m)]}\right]$
    (f) End For
(6) End For
```

The input spectrum of RESOLUTION can be the result of a MC simulation. It is introduced as an ASCII file which contains, for each channel, a line with two real values specifying the energy at the center of the bin (in keV) and the corresponding number of counts of the bin. The total number of bins is arbitrary. The peak shape is specified by several input parameters, which are introduced by means of a graphical user interface (fig. 2.10).

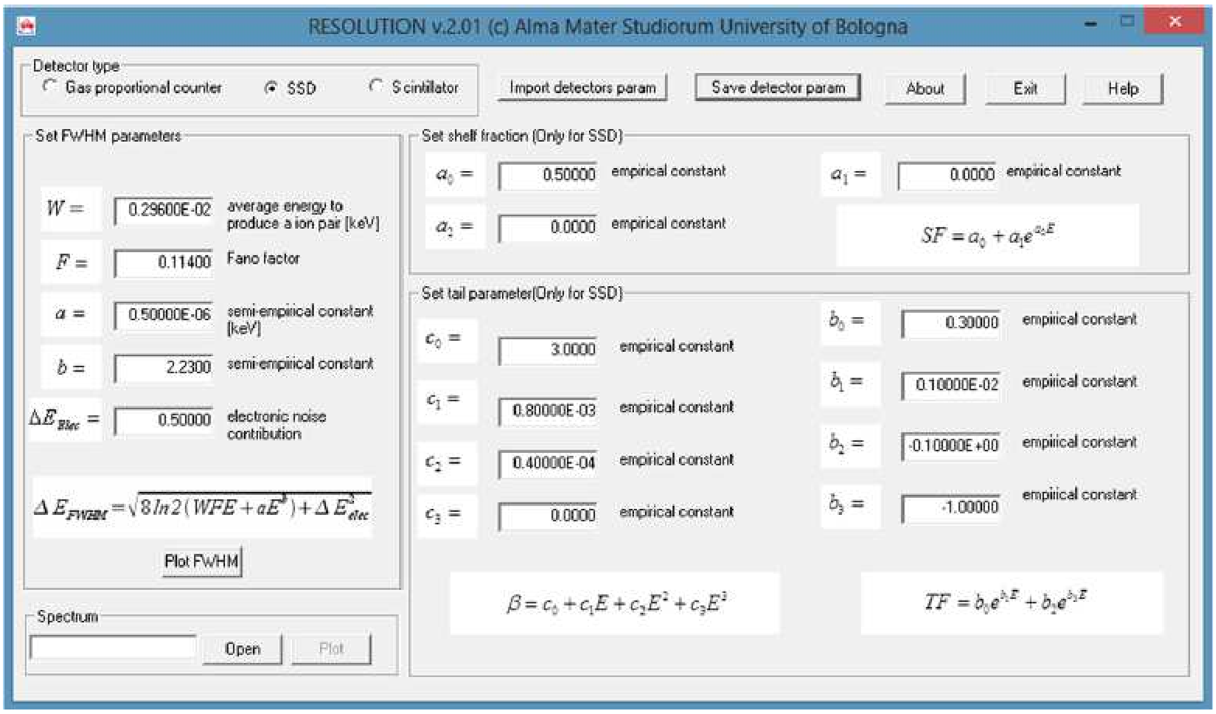

Detector type: ○ Gas proportional counter ● SSD ○ Scintillator

$W =$ 0.29600E-02 average energy to produce a ion pair [keV]

$F =$ 0.11400 Fano factor

$a =$ 0.50000E-06 semi-empirical constant [keV]

$b =$ 2.2300 semi-empirical constant

$\Delta E_{Elec} =$ 0.50000 electronic noise contribution

$a_0 =$ 0.50000 empirical constant

$a_1 =$ 0.0000 empirical constant

$a_2 =$ 0.0000 empirical constant

$c_0 =$ 3.0000 empirical constant

$c_1 =$ 0.80000E-03 empirical constant

$c_2 =$ 0.40000E-04 empirical constant

$c_3 =$ 0.0000 empirical constant

$b_0 =$ 0.30000 empiiical constant

$b_1 =$ 0.10000E-02 empiiical constant

$b_2 =$ -0.10000E+00 empiiical constant

$b_3 =$ -1.00000 empiiical constant

Figure 2.10: Graphical interface of the tool RESOLUTION reporting the parameters for a CdTe detector.

The parameters are divided into groups. The first one (Set FWHM parameters in figure 2.10) allows to model the FWHM of the Gaussian shape. Depending on the detector type, formula and parameters change automatically in the interface to resemble

Eqns.(2.2.71)-(2.2.73). The button *PlotFWHM* allows the visualization of the computed FWHM as a function of the energy (fig.2.11).

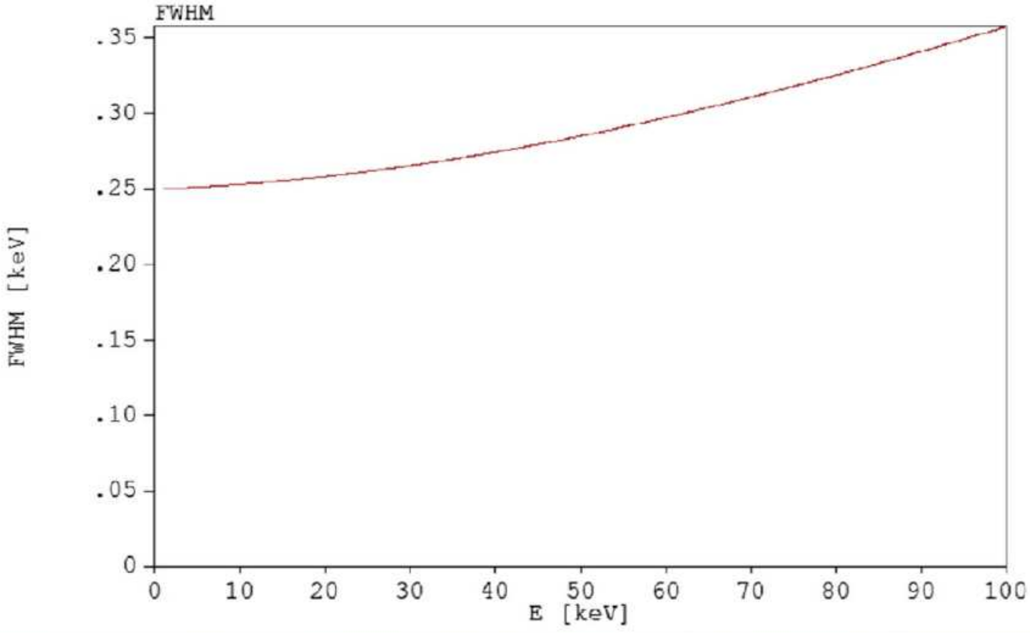

Figure 2.11: Full width at half maximum (FWHM) computed with RESOLUTION as a function of the energy for a Ge detector.

For SSD, the groups "Set shelf fraction" and "Set tail parameters" (on the right side in fig. 2.10) contains the parameters to model the departures from the Gaussian shape. It possible to insert the detectors parameters manually or by means of an external text file and to save them in a text file.

An error message appears any time the introduced parameters produce negative values in the output spectrum. At the end of the computation, RESOLUTION automatically plots the results of the convolution with the possibility to choose the scale from linear to logarithmic.

2.2.3 Examples of RESOLUTION applications with SSD

As it is apparent from Eqs.(2.2.64)-(2.2.66) and Eqs.(2.2.71)-(2.2.73), RESOLUTION requires many parameters to completely describe the detector resolution, providing a very adaptable model. On the other side, to find the best parameter combination may be tricky in practical cases. In what follows, a suggested procedure is described.

1. Measure one (or more) well isolated peak(s), taking care that effects like PPU are kept to a minimum. It is advisable to perform a pulse pile-up correction when possible before to proceed.

2. Compute the energy deposition spectrum for the same peak using, for example, a deterministic or a MC code.

3. Import this energy deposition spectrum into the code RESOLUTION by reading the corresponding ASCII file.

4. Model the energy resolution using the code RESOLUTION.

  A. As first attempt, it is recommended to express the line shape using only the Gaussian function, with standard parameters for the considered detector type. Set to zero all the other groups.

  B. Compare the results of RESOLUTION with the measurement, and change the Gaussian parameters until the agreement is good. For some detectors, no further improvement is required.

  C. If the Gaussian function fails to describe properly the detector line shape, then start including the shelf and the tail distribution, in separate steps.

    i. If the continuum of the energy deposition spectrum differs significantly from the one in the measurement, add the shelf distribution. First, set a proper value of a_0 while leaving the other parameters equal to zero. The parameters a_1 and a_2 represents a refinement and can be adjusted in a second moment, if necessary.

    ii. The comparison between the Gaussian function and the measurement is helpful to understand the entity of the asymmetry of the full energy peak. If the measured peak is skewed on the lower energy, add the tail parameters. First, set all the tail fraction parameters equal to zero except for b_0 and c_0. By means of an iterative comparison with the measurement, adjust b_0 and c_0. The other parameters can be added after a first raw representation of the exponential tail is completed, to improve the agreement with the experimental data. As it is apparent from Eq.(2.2.70), both TF and β concur to model the tail fraction, and therefore cannot be set separately.

Fig.2.12-A shows the Monte Carlo simulation of the energy deposition in a Ge detector for a monochromatic source of photons of 34.4 keV. The simulation was performed using the code PENELOPE [27] by considering a cylindrical germanium crystal surrounded by a layer of aluminum and protected by a Be window. Figure 2.12-B shows the application of RESOLUTION by considering the modified Gaussian distribution with the complete model, including shelf and tail description.

Another example of RESOLUTION application can be introduced by considering a CdTe SSD. A known problem in CdTe detectors is the presence of a significant hole tailing in their response above 50 keV [99]. As an example, the response of the Amptek CdTe detector is computed with the code MCSHAPE. The source is Co-57, emitting at 14.41300 keV (9.16%), 122.0614 keV (85.60%) and 136.4743 keV (10.68%). The result of the MC simulation (without the effect of energy resolution and charge collection) is then

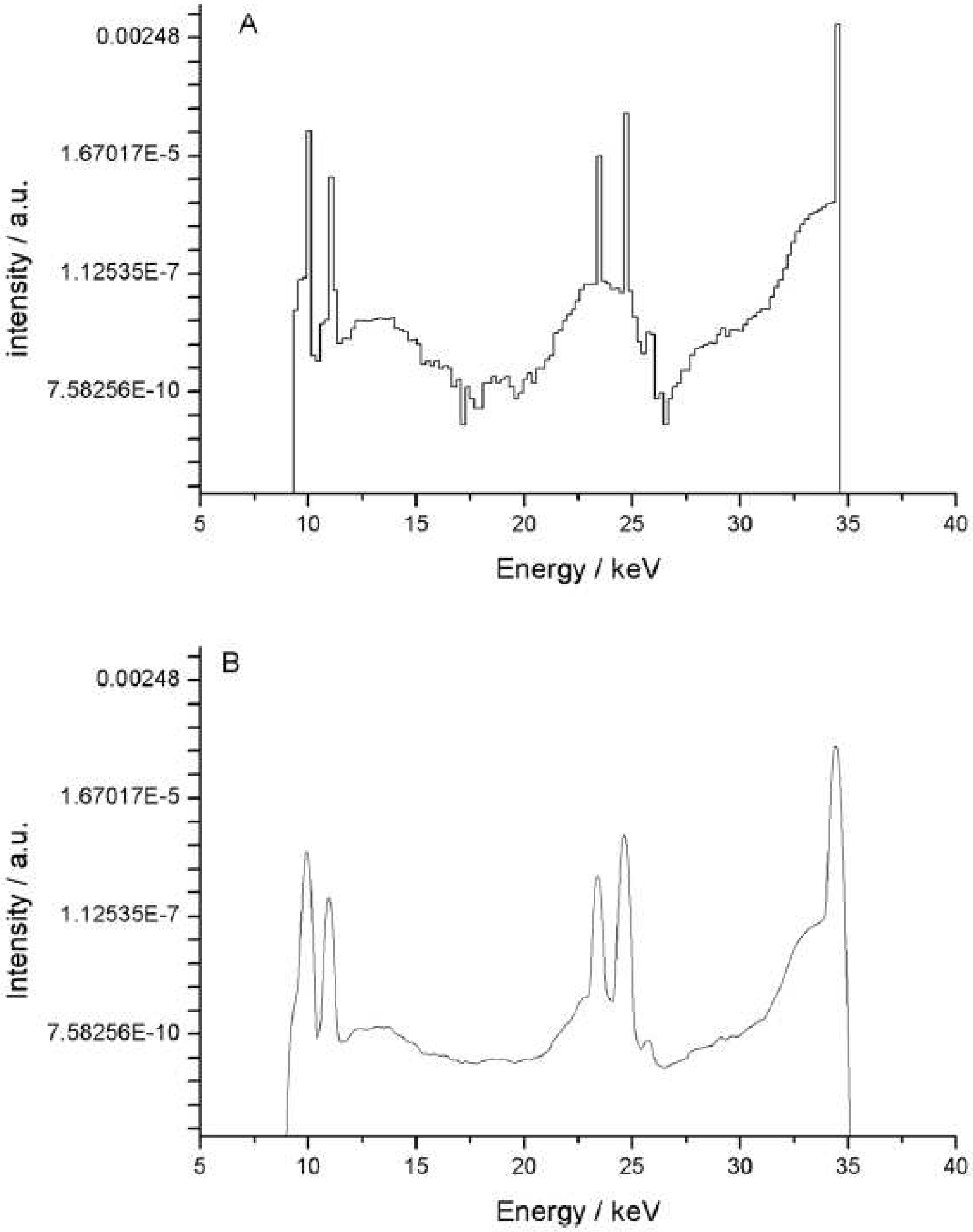

Figure 2.12: (A) Result of the Monte Carlo simulation of a Ge detector response function for a monochromatic source of photons of 34.4 keV and (B) detector response function after the application of the code RESOLUTION. In this case, the departure from the Gaussian model is negligible.

used as input by the tool RESOLUTION. Fig.2.13-A shows the comparison between the measure and the result of RESOLUTION applying a Gaussian model for the main peak of Co-57. It is apparent the poor capability to describe the peak shape without a correction for the low energy tail of the peak. Fig.2.13-B shows the result of RESOLUTION after applying the complete model, including shelf and tail description. It is worth noting that the agreement with the measure is good also for the peak at 136 keV (see fig.2.14).

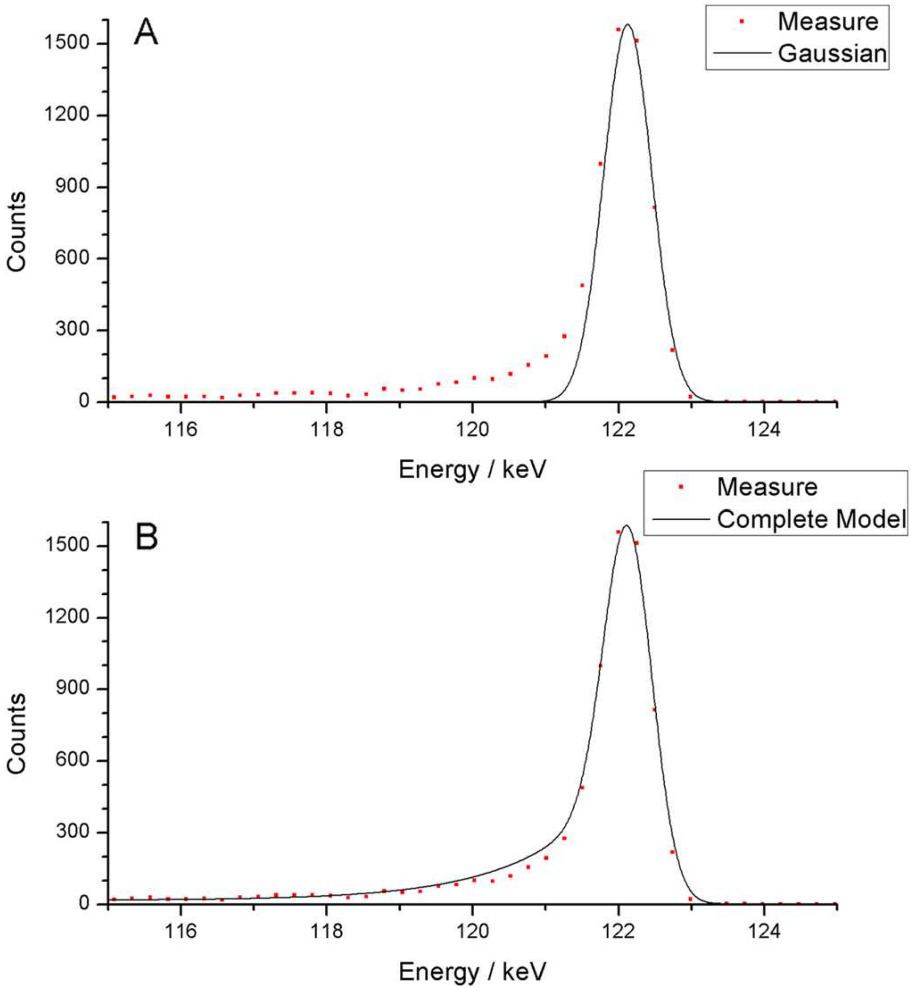

Figure 2.13: Main peak of Co-57 at 122.06 keV, collected with an AMPTEK CdTe detector (dots), compared with the energy resolution computed by RESOLUTION with (A) only the normalized Gaussian function and (B) the complete model including hole tailing.

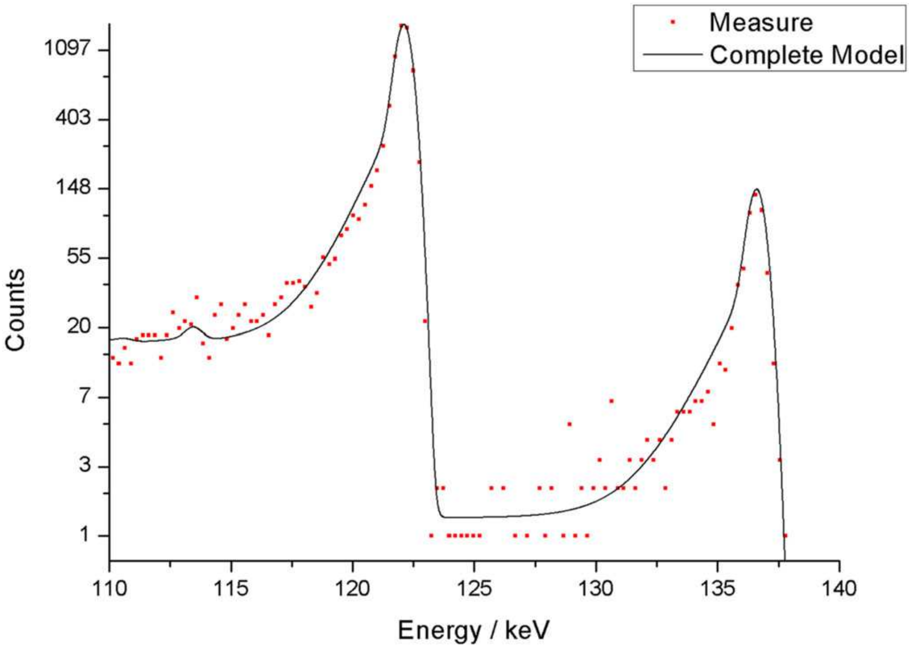

Figure 2.14: Co-57 spectrum collected with an AMPTEK CdTe detector (dots). The output of RESOLUTION describes correctly the shape of the two peaks located at 122.06 and 136.47 keV.

2.3 Detector unfolding

Once the detector response function (DRF) is computed it can be used for recovering the scattered spectrum (see fig.2.1) which is the final result of the complete unfolding procedure (including the pulse pile-up correction). In the DRF theoretical model it was introduced (Eq.(2.2.54)) the fundamental relation between the measured spectrum and the scattered one. In order to give a brief introduction on the mathematical difficulties concerning detector unfolding here Eq.(2.2.54)is reported as:

$$I_m(E) + \epsilon_m(E) = \int\limits_{E_{min}}^{E_{max}} \mathcal{K}(E', E) f(E') dE', \tag{2.3.74}$$

where the measure is split in its true value I_m and the associated absolute error ϵ_m. E_{min} and E_{max} are the chosen minimum and maximum energies of the scattered spectrum with a non negligible contribution of counts.

Considering the Hadamard conditions, exposed at the beginning of this chapter, existence and uniqueness of the solution of Eq.(2.3.74) depends almost exclusively on the mathematical typology of the kernel. Stability instead depends on the structure itself of this equation. It can be showed that stability condition is always not satisfied by Eq.(2.3.74).

Following what was done for the pulse pile-up balance equation, it can be considered a solution of the type:

$$f(E) = x(E) + \beta \sin(n\beta E) \;\; n = 1, 2, ... \tag{2.3.75}$$

where $x(E)$ is an un-perturbed solution of the integral equation and $\beta \sin(n\beta E)$ a perturbation. Inserting Eq.(2.3.75) in Eq.(2.3.74):

$$I_m(E) + \epsilon_m(E) = \int\limits_{E_{min}}^{E_{max}} \mathcal{K}(E', E)x(E')dE' + \beta \int\limits_{E_{min}}^{E_{max}} \mathcal{K}(E', E) \sin(n\beta E')dE'. \tag{2.3.76}$$

For the Riemann-Lebesgue theorem [81]:

$$\int\limits_{E_{min}}^{E_{max}} \mathcal{K}(E', E) \sin(n\beta E')dE' \rightarrow 0 \quad for \;\; n \rightarrow \infty, \tag{2.3.77}$$

which means that for n big enough the perturbation on the solution gives irrelevant change on the measured spectrum.

The reason for this instability is in the smoothing property of the integral. Smoothing process (which is the direct problem related to this unfolding one) is always well-posed giving as a consequence an ill-posed inverse problem.

Several methods have been developed for avoiding the discussed ill-posed behaviour in order to solve the inverse problem (see [100]; [101]). Most of these methods recur to purely mathematical criteria and may lead to an non physical solution, i.e. negative values in the resulting spectrum. In particular, fast Fourier transforms algorithms have been used in the past to improve the detector resolution [102]; [103]. These methods present some additional drawbacks: they create false peaks that can be confused with the real ones and need to be applied to limited energy regions around the peaks and not to the entire spectrum.

Another important category of methods for solving an ill-posed problem are the so called Regularization techniques which introduce additional information as constraints for avoiding the ill-position. Among the different regularization techniques developed, in order to perform the unfolding from the DRF function, the method of the maximum entropy [104] is chosen for its fundamental property of preserving the positive-defined character of the spectrum. The maximum entropy method has been implemented in the code MAXED [105] which solves the inverse problem by optimizing the entropy functional, taking advantage of the known a priori information on the original spectrum. MAXED represents the state-of-the-art for unfolding of neutron spectra. GRAVEL [104] is another useful unfolding algorithm which preserves positive values in the spectra. Both codes, MAXED and GRAVEL, are contained in the UMG (Unfolding with MAXED and GRAVEL) package version 3.3, released in March 2003, developed at the Physikalisch Technische Bundesanstalt (PTB) and distributed by NEA Data Bank [106].

The code UMESTRAT [107] developed recently at the University of Bologna, exploits the maximum entropy approach in X-ray spectrometry applications, for the unfolding of X- and gamma-ray spectra. UMESTRAT provides a semi-automatic unfolding strategy based on a suitable combination of MAXED and GRAVEL. The original algorithm presented in [107] leads to solutions which can be considered qualitative but not quantitative. In what follows it will be discussed the principal features of the new version of UMESTRAT [5] which allows to obtain quantitative results. This is possible by introducing the additional constraint of the total number of photons of the spectrum which can be determined by inverting the diagonal efficiency matrix. The features of the upgraded code are discussed with some examples which illustrate the important software improvement of the detector resolution as a consequence of the unfolding.

2.3.1 MAXED algoritm

Consider the discretization of Eq.(2.3.74):

$$I_k + \epsilon_k = \sum_{i=1}^{n} R_{ki} f_i \quad k = 1, 2, ..., m \tag{2.3.78}$$

where n and m are the number of energy bins; k and i are channel indices, R is the DRF and ϵ_k represents the (unknown) errors, which require estimation.

The chi-square per degree of freedom χ^2 can be introduced as follows:

$$\chi^2 = \frac{1}{n} \sum_{k=1}^{m} \frac{\epsilon_k^2}{\sigma_k^2}. \tag{2.3.79}$$

Eq.(2.3.79) assumes that the errors are normally distributed with zero mean and variances σ_k^2.

As reported in [105], from the set of possible solutions, the one that maximizes the information entropy S is selected:

$$S = -\sum_{i=1}^{n} \left[f_i \log\left(\frac{f_i}{f_i^{def}} \right) + f_i^{def} - f_i \right]. \tag{2.3.80}$$

In Eq.(2.3.80) f_i^{def} denotes the so-called default spectrum, which contains all the a-priori information on the original spectrum. In other words, the solution represents the maximum of S (Eq.(2.3.80)), with the constraints given by Eqs.(2.3.78) and (2.3.79).

As shown in [105], starting from Eqs (2.3.78)-(2.3.80), and defining a set of m Lagrange multipliers λ_k, the problem can be reformulated in terms of the maximization of the potential function Z :

$$Z = -\sum_{i=1}^{n} f_i^{def} \exp\left(-\sum_{k=1}^{m} \lambda_k R_{ki} \right) - \left[\chi^2 \sum_{k=1}^{m} (\lambda_k \sigma_k)^2 \right]^{\frac{1}{2}} - \sum_{k=1}^{m} \lambda_k I_k. \tag{2.3.81}$$

In MAXED the values of λ_k which maximize Z are obtained by means of a simulated annealing algorithm. These values are then introduced in the following expression:

$$f_i = f_i^{def} \exp\left(-\sum_{k=1}^{m} \lambda_k R_{ki}\right), \tag{2.3.82}$$

to find the unfolded spectrum f (free of detector influences).

It is worth noting that the χ^2 constraint introduces a dependence of the total number of counts in the unfolded spectrum with the chosen value of the chi-square. This can be illustrated by considering a single energy channel detector with DRF R. From Eqs.(2.3.78) and (2.3.79) it is possible to find the original spectrum as:

$$f = \frac{I}{R} + \frac{\sigma\sqrt{\chi^2}}{R}. \tag{2.3.83}$$

In general, after the unfolding, the total number of counts in the original spectrum depends on the chi-square. In MAXED, this parameter is arbitrarily introduced as an input by the user, considering not only the physics but also the numerical characteristics of the problem, ensuring the convergence of the algorithm. It is worth noting that incorrect values of χ^2 lead to meaningless results (or no results at all). The variability of the unfolded spectrum with the selected χ^2, makes the result only qualitative. In order to obtain a quantitative result it is necessary to introduce the additional constraint of the total number of counts in the unfolded spectrum, as illustrated in the following section.

2.3.2 UMESTRAT

UMESTRAT [107] is a graphical tool developed at the University of Bologna to obtain the unfolding solution applying a combination of the codes MAXED [105] and GRAVEL [104]: MAXED is used to compute the unfolding, whereas GRAVEL is used to find suitable parameters to ensure the convergence of MAXED. Given the measurement and the DRF, UMESTRAT computes and plots the unfolded spectrum, as a function of the energy. The main features of the code are illustrated in [107]. In this work it is presented an improvement of UMESTRAT [5] including a strategy to recover the quantitative meaning of the unfolded spectrum. As shown in the previous section, the total number of counts of the unfolded spectrum depends on the value of the χ^2 which, in the UMESTRAT strategy, can be obtained by running GRAVEL first or can be set arbitrarily by the user. In order to obtain a solution which is independent of the selected χ^2, it is necessary to link the unfolded spectrum to the measurement by introducing a common magnitude not considered yet in the algorithm. A good candidate is the total number of counts which can be estimated with good precision by taking advantage of the detector physics as shown below.

Consider the discretization of the DRF (Eqs.(2.2.55) and (2.2.56)) and also given [86]:

$$R_{ki} = \sum_{r=1}^{n} \left(\sum_{j=1}^{n} Q_{kj} G_{jr} \right) \phi_{ri} = \sum_{r=1}^{n} N_{kr} \phi_{ri}, \tag{2.3.84}$$

where j, r, and k are channel indices and n is the total number of channels. The detector response matrix can be split in the product of a normalized part N (given by the product of the energy deposition spectrum Q and the energy resolution G) and efficiency ϕ. The efficiency is a diagonal matrix expressed as:

$$\phi_{ri} = \begin{cases} \phi_{ri} & r = i_0 \\ 0 & r \neq i \end{cases} . \tag{2.3.85}$$

Introducing Eq.(2.3.84) in Eq.(2.3.78) gives:

$$I_k + \epsilon_k = \sum_{i=1}^{n} \sum_{r=1}^{n} N_{kr} \phi_{ri} f_i \quad k = 1, ..., m \tag{2.3.86}$$

By inverting the sum order it is possible to obtain:

$$I_k + \epsilon_k = \sum_{r=1}^{n} N_{kr} \sum_{i=1}^{n} \phi_{ri} f_i \quad k = 1, ..., m \tag{2.3.87}$$

To maintain the quantitative meaning in the solution, it is necessary to introduce the additional constraint given by the total number of counts of the unfolded spectrum. For this purpose, the new strategy implemented in UMESTRAT [4] splits the solution of the linear system in Eq.(2.3.87) (i.e. the unfolding of the measurement) in three steps.

In the first step, UMESTRAT unfolds the measured spectrum considering only the normalized part of the DRF, finding the solution y of the linear system:

$$I_k + \epsilon_k = \sum_{r=1}^{n} N_{kr} y_r \; with \; k = 1, ..., m \tag{2.3.88}$$

From the physical point of view the unfolded spectrum y in Eq(2.3.88) must have the same number of counts of the measured spectrum because the normalized matrix N produces only a smearing effect on the original spectrum. The difference in the total number of counts between the measured and the original spectrum is a consequence of the efficiency.

In the second step, the constraint on the total number of counts is introduced. The spectrum y is normalized by using the total number of counts of the measurement $\sum_{i=1}^{n} I_i$, thus finding the spectrum y^{norm}:

$$y_r^{norm} = \frac{\sum_{i=1}^{n} I_i}{\sum_{i=1}^{n} y_i} y_r . \tag{2.3.89}$$

In the third and last step, the original spectrum f_i is computed by solving:

$$y_r^{norm} = \sum_{i=1}^{n} \phi_{ri} f_i = \phi_{rr} f_r \quad r = 1, ..., n \tag{2.3.90}$$

It is worth noting that this new UMESTRAT strategy, comprising the constraint in the total number of counts of the original spectrum, requires as separated input the efficiency and the normalized detector response matrix. An additional advantage of this strategy is that it avoids the modification of the MAXED algorithm.

2.3.3 Energy resolution improvement in radiation measurements

The unfolded spectrum obtained with UMESTRAT can now be considered quantitative. The old version of UMESTRAT was firstly tested on X-ray fluorescence (XRF) spectra measured with a XR-100CR Amptek Si detector, using a bin width of 50 eV. As shown in [107], by using UMESTRAT it was possible to resolve the Zn Kα and Cu Kβ peaks which were overlapped in the brass measurement. The spectrum after unfolding showed a FWHM of about 200 eV for the Cu Kβ peak, which was half of the measured one giving the detector resolution for that energy.

In this work, the capabilities of the new version of UMESTRAT are explored with SSD other than Si. The first example shows the unfolding of XRF spectra revealed using a XR-100T Amptek CdTe detector and collected with a MCA-8000A multichannel analyzer, with 1024 bins of 100 eV of bin width. The source is a Tungsten X-ray tube, with a glass window, operating at 50 kV. The DRF matrix is estimated using the MC code MCSHAPE [86] and the post processing tool RESOLUTION [4] (described in the previous section 2.2.2), which adds the effects of incomplete charge collection and the energy resolution of the detector. For the energies in the range 6-50 keV, the CdTe detector has an almost ideal efficiency and charge trapping effects are limited. Fig.2.15 shows the XRF lines of a brass target. It is apparent that after unfolding with the new version of UMESTRAT the peaks appear better resolved: due to the choice of the bin width, the Zn-Kα and the Cu-Kβ peaks cannot be separated anymore. The FWHM is now less than 300 eV which is 30% less of 400 eV, the detector resolution for that energy.

Fig.2.16 shows the unfolding of the L Pb lines of a Pb target, under the same experimental conditions. For the Pb L α peak, the FWHM goes from 430 eV in the measurement to 244 eV after the unfolding with UMESTRAT. In the unfolded spectrum some minor Pb L lines are visible, in particular Pb Ls (9.9688 keV) and Pb Lη (11.349 keV). A second example shows the unfolding of a direct measurement of a X-ray tungsten tube operating at 110 keV, collected with a ORTECH PGE detector(Fig.2.17). The DRF is computed with the MC code PENELOPE [27] considering a complete 3D model of the detector. The computed energy deposition spectra are post processed with the tool RESOLUTION [4], adding the energy resolution and the charge trapping effects. It is worth noting that in this case the effects of incomplete charge collection are high, increasing the ill-conditioning of the problem. Nevertheless, UMESTRAT may find the unfolding solution. It is apparent that the lower energy part of the measured spectrum (below 20 keV) represents a detector artefact due to the DRF (escape plus resolution shelf). In this example the energy discretization of the measure(with a bin width of 200eV) allows only a coarse description of the peaks. The improvement of the FWHM is apparent: for W Kα the FWHM goes from 470 eV in the measurement to 306 eV in the unfolded spectrum.

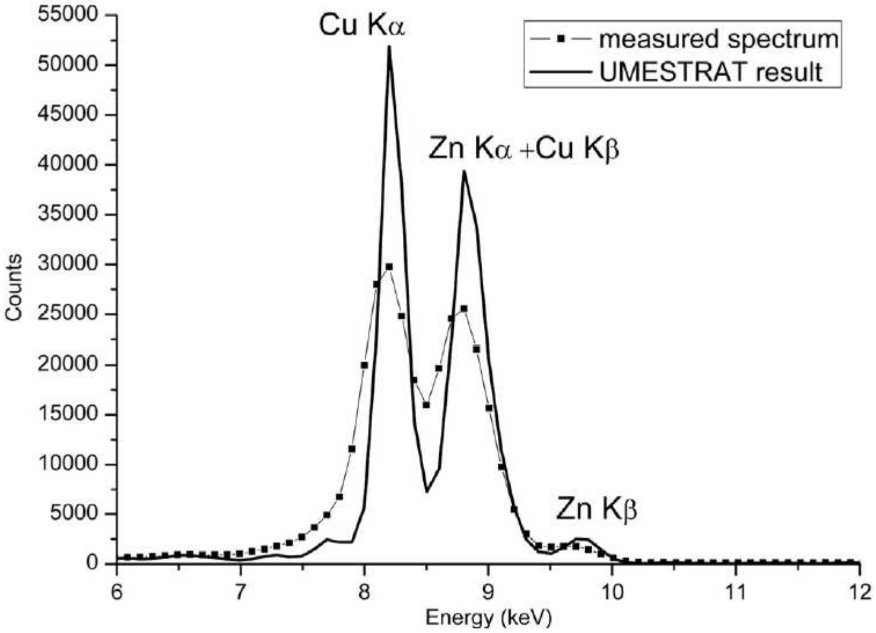

Figure 2.15: Unfolding of a brass spectrum collected with a XR-100T Amptek CdTe detector and a bin width of 100eV. The resolution is improved by 30% and the Zn-Kβ peak is better resolved. The Zn-Kα and the Cu-Kβ peaks cannot be separated as for the Si detector.

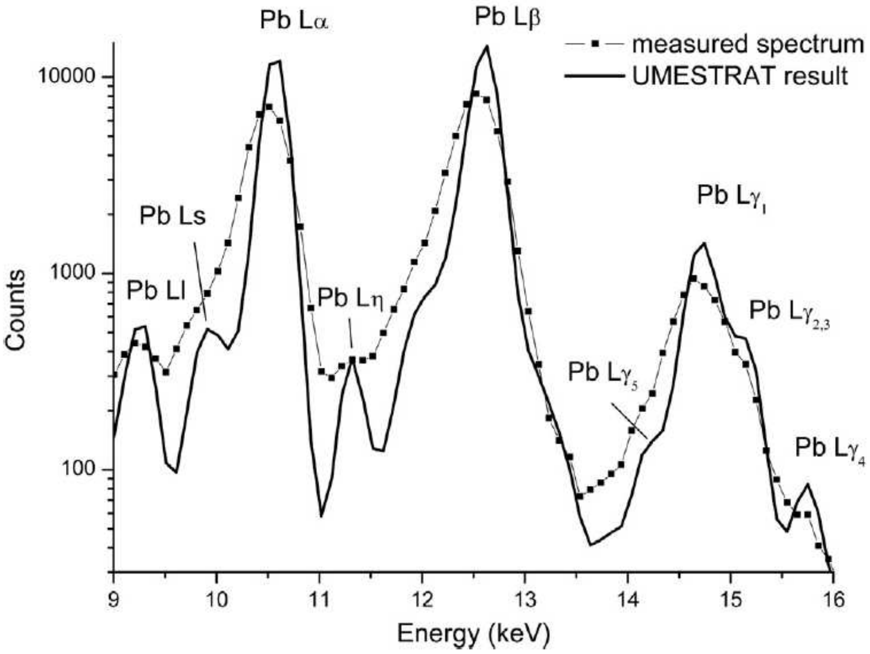

Figure 2.16: Unfolding of a Pb spectrum collected with a XR-100T Amptek CdTe detector. It is apparent that the resolution is improved: for the Pb-Lα peak, the FWHM goes from 430 eV in the measurement to 244 eV after the unfolding with UMESTRAT

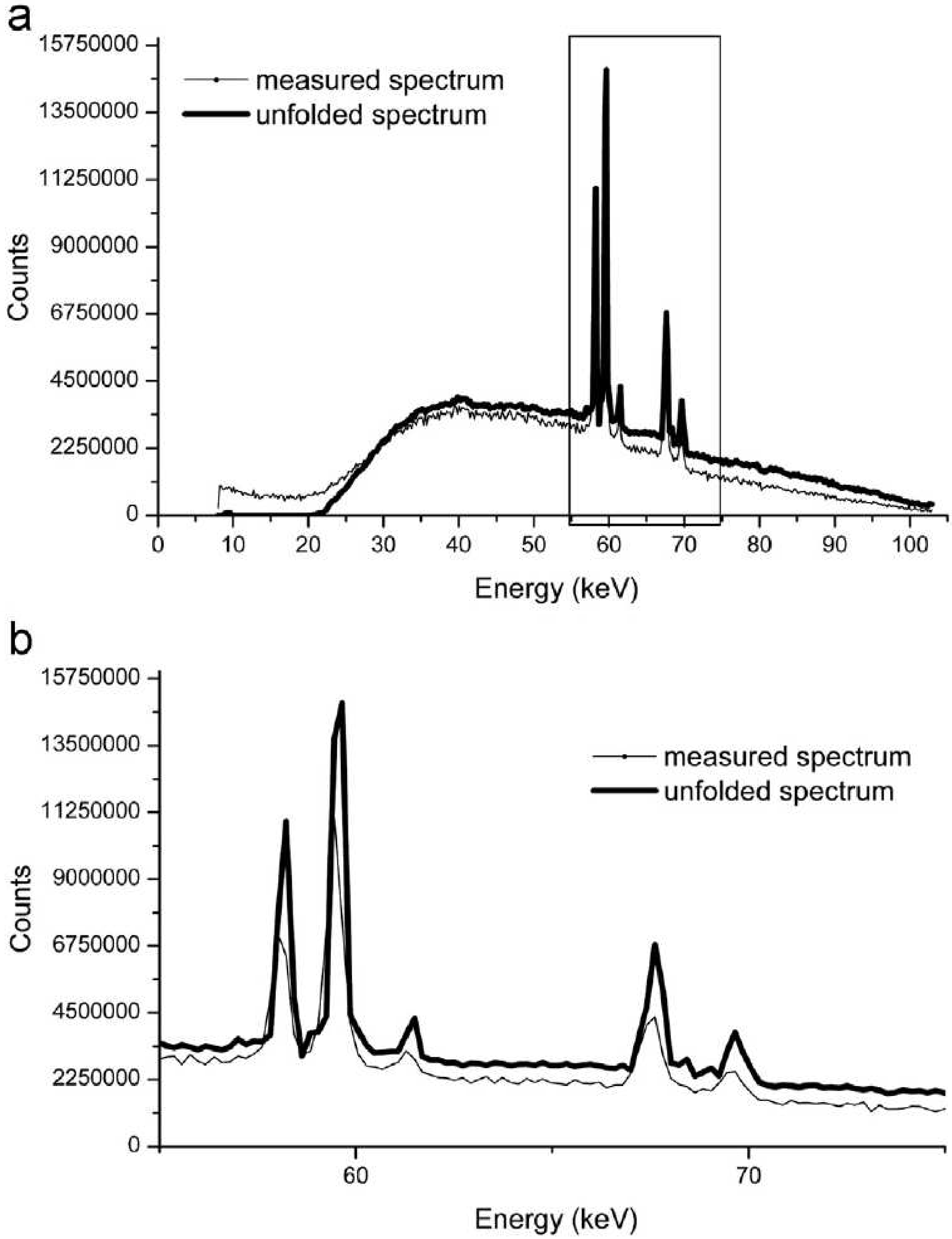

Figure 2.17: Unfolding of a direct measurement of a W X-ray tube spectrum, operating at 110 keV. The lower part of the measured spectrum (below 20 keV)is not physical but represents a detector artefact due to the continuous part of the detector response function(Compton continuum and shelf).It is removed in the unfolded spectrum. (b)The peak region shows the improvement in resolution: the FWHM goes from 470 eV in the measurement to 306 eV in the unfolded spectrum.

Conclusions

Quantitative information on the photoeffect is required for practical applications (*e.g.*, x-ray fluorescence, x-ray photoelectron spectroscopy), as well as for Monte Carlo simulation of photon transport. Numerical tables of subshell cross sections (for ionization and for excitation to bound levels) and atomic cross sections are included in the Evaluated Photon Data Library (EPDL) [14]. There is also the XCOM program [15] which gives atomic cross sections for photoionization essentially equivalent to those in the EPDL. Both the EPDL and XCOM databases are based on calculations performed by Scofield [7] using the independent-electron model with the self-consistent Dirac-Hartree-Fock-Slater (DHFS) potential. They are considered to be the most reliable source of general information available to date; indeed, practically all modern Monte Carlo codes for photon transport utilize the EPDL. However Scofield's Calculations were performed without the modern computational possibility using sometimes a too wide energy grid.

Regarding the angular distribution of photoelectrons is needed in x-ray photoelectron spectroscopy, using either x rays or synchrotron radiation [23, 24, 25], as well as in radiation transport calculations [26, 27]. However information on the angular distribution of photoelectrons, consistent with the subshell cross sections, is quite limited, or unavailable (see, *e.g.*, Ref. [28] and references therein). As a matter of fact, most Monte Carlo photon transport codes still rely on the Sauter formula [29], which gives the differential cross section for the ground state of hydrogenic ions obtained from the plane-wave Born approximation.

In this thesis it was presented a detailed formulation of the theory of the photoeffect, within the one-active-electron approximation, in a form that is suitable for implementation in a computer program, complemented with extrapolation schemes to cover the full energy range of interest.

Because of the robustness of the numerical methods (exact vector-coupling coefficients, highly accurate and densely tabulated radial functions), the program PHOTACS provides reliable results for any atomic (or ionic) target and for any photon energy below the practical cut-offs. It allows generating cross section tables of subshell cross sections for the elements with unprecedented detail, including excitation to bound levels and angular distributions of photoelectrons for arbitrary photon polarizations. Although in the present calculations it is adopted the DHFS self-consistent potential, the program can also work with other screened potential models, *e.g.*, to study the influence of the electron vacancy left after photoabsorption.

The post-processing program PHOTACS-PP uses elaborate extrapolation models to determine subshell cross sections for highly-excited discrete levels and for photons with energies above the calculation cut-offs. It can also account for the effect of the finite width of atomic levels, which yields the cross section as a continuous function of the photon energy.

These programs have been used to generate a complete database of photoionization cross sections for the inner subshells (up to the N7 subshell) of the ground state configurations of the elements $Z = 1$ to 99, for photon energies from the ionization threshold up to 1 GeV. The provided cross-section tables were built from the numerical cross sections calculated by PHOTACS (with the DHFS potential), which were extrapolated to energies higher than the calculation cut-off by means of Pratt's extrapolation formula, shifted in energy to have the absorption edges coinciding with the experimental subshell ionization energies given by Carlson [66], and renormalized using MCDF/DHFS density ratios. This database has already been adopted in the Monte Carlo code PENELOPE [27].

In order to correct measured spectra from PPU effect a nonlinear integral balance equation is derived from first principles considering the measured spectra in a continuous energy range (before the action of the MCA). The presented model takes into account only second order PPU and can be applied on both paralyzable and non paralyzable detectors assuming a rectangular pulse shape. The obtained balance equation is solved with an iterative formula whose convergence is demonstrated by analyzing the solution of the balance equation in the Laplace transform domain. The iterative calculation is then adapted to be applied to a discretized energy interval and then solved by using the SOR method. This deterministic correction of the PPU effect requires a minimum amount of information (live time, dead time and the experimental measure to correct).

In order to solve more general pulse pile-up problem also a Monte Carlo strategy was implemented with the code MCPPU. MCPPU is a computational tool which performs post- processing pile-up correction on spectra obtained with different detectors. It takes into account every order of PPU, peak or tail. MCPPU corrects pile-up distortions for spectra collected with or without electronic reduction circuitry. The resulting spectrum after the correction recovers the proper number of counts recorded at the correct energy channels. MCPPU implements an iterative Monte Carlo algorithm based in the one introduced by Guo et al. [83] [84] to compute automatically the PPU correction.

It uses a digitized pulse shape matching the measured pulse. The digitized pulse shape is easily introduced by means of an external text file. This unique feature makes the tool suitable to be used with any detectoramplifier combination. To make possible the comparison with previous works, MCPPU allows also the selection of the pulse shape from a library of rectangular and semi-Gaussian shapes described in literature [76] [80]. MCPPU contains also an automatic procedure to evaluate the dead time to use in the pile-up recovery which needs only a high counting rate and a low counting rate measurement of the same spectrum. Once determined, the same dead time can be used for all the measurements performed with the same acquisition conditions. The comparison of corrected high counting rate spectra with experimental low counting rate spectra, demonstrates that MCPPU can efficiently remove pile-up distortions.

The method was tested successfully with Si SSD obtaining the same results obtained with the deterministic strategy. The presence in the results of both MCPPU and deterministic strategies of the same numerical artifacts shows that they are not influenced by the Monte Carlo statistics and they are due to the statistical fluctuation with the combined influence of the detector energy calibration and the MCA discretization in energy, and cannot be avoided. The proposed deterministic approach is then to be preferred to the most elaborated method (at least for Si SSD) because it is simpler to be used and faster. The convergent solution of the deterministic balance equation is obtained after only five iterations with a total computational time of few seconds.

Regarding the detector response function it was developed a new tool for inserting the effects of the energy resolution and incomplete charge collection in the computed response function. Energy resolution is a characteristic of the DRF that depends on different aspects (statistical spread in the number of charge carriers, charge collection phenomena, electronic noise, etc.) and changes with operating conditions, counts rates, and pulse shape. For these reasons, it is not, or is only partially, considered in Monte Carlo or deterministic models of the detector response. However, its effect plays an important role in X-ray spectrometry, in both qualitative and quantitative analyses of X-ray spectra. The tool RESOLUTION developed to simply and fast add the effect of the energy resolution to the DRF computed with deterministic or Monte Carlo codes has been potentiated with an adaptation of the general HYPERMET function [87]. In the adopted procedure, the Gaussian distribution, the exponential tail, and the shelf are kept separated and are added in successive steps: the full energy peak is firstly modified by the exponential tail and the shelf distribution and then convoluted with the Gaussian spread. The expression of the FWHM is implemented by using the models found in literature [76] [93] for the three detector types: SSD, scintillators, and gas proportional counters. For SSD, the effects due to the charge collection mechanism are introduced by using the models presented by Phillips et al.[87] and Campbell et al. [88]. The presence of a hole tailing is particularly evident for CdTe operating above 50 keV. RESOLUTION proved to be able to describe this effect in the case of the main peaks of Co-57.

Regarding the detector unfolding the new version of UMESTRAT applies a new strategy to optimally solve the inverse problem in a semi-automatic mode by using the maximum entropy principle through a combination of the codes GRAVEL [104] and MAXED [105]. This work presented an improvement of the code UMESTRAT with the introduction of the constraint on the integral of the original spectrum which allows finding quantitative results. Now UMESTRAT can be used as a post processing correction of revealed spectra, to improve the detector resolution, with, as a consequence, the capability to resolve overlapped peaks in the measurement. UMESTRAT has been tested with different solid state detectors. For a Si detector, for the CuKα peak, the spectrum after the unfolding has FWHM of about 200 eV, which is half of the original resolution due to the detector. For the CdTe detector,for the PbLα peak, the FWHM goes from 430 eV in the measurement to 244 eV after the application of UMESTRAT. In the unfolding of a direct measurement of a X-ray tube collected with a HPGe detector, the energy discretization of the measure(bin width of 200 eV)allows only a coarse description of the peaks.In this example, the unfolding removes the lower energy side of the collected spectrum, which is due to the detector response function and the Tungsten Kα FWHM goes from 470 eV in the measurement to 306 eV in the unfolded spectrum. All the examples prove that UMESTRAT can handle a dense detector response matrix, containing the complex effects of charge collection, demonstrating the capability of the algorithm to successfully solve heavy ill conditioned problems.

Summary of the activities done during the PhD course

Developed codes:

1. PHOTACS: code written in FORTRAN77 for the calculation of photoeffect subshell cross sections for arbitrary atomic potentials.

2. MCPPU: a Monte Carlo code written in Fortran90 (comprising graphical interface built with Winteracter), for correcting radiation measures from the pulse pile-up effect.

3. RESOLUTION: graphical tool written in Fortran90 (comprising graphical interface built with Winteracter) for introducing energy resolution and incomplete charge collection effects in the detector response function.

4. UMESTRAT: code written in Fortran90 (comprising graphical interface built with Winteracter) for the unfolding of radiation measures from the detector response function.

Participation to conferences:

1. IRRMA9 (9th International Topical Meeting on Industrial Radiation and Radioisotope Measurement Applications) in Valencia from 6 to 11 July 2014.

2. Member of the Local Organizing Committee of the EXRS-2014 (European Conference on X-Ray Spectrometry) in Bologna from 15 to 20 June 2014.

Participation to applications compatible with the doctorate:

1. Part-time work at NIER Ingegneria for verification and validation of mechanical systems from October to December 2015.

2. Winner of the Marco Polo grant used for developing research activity at the department of physics of the University of Barcelona under the supervision of Prof. Francesc Salvat from 6 October 2014 to 1 March 2015.

Courses attended:

1. Numerical modelling with COMSOL Multiphysics (University of Bologna, Prof. Stefano Lazzari, 8 hours course).

2. Kinetic equations and statistical foundations of transport theory (University of Bologna, Prof. Domiziano Mostacci, 8 hours course).

3. Numerical techniques for solving the neutron transport equation (University of Bologna, Prof. Marco Sumini, 8 hours course).

4. Elements of Microfluidics (University of Bologna, Prof. Gian Luca Morini, 8 hours course).

5. Inverse problems in heat conduction (University of Bologna, Prof. Marco Lorenzini, 8 hours course).

6. Availability functions and thermodynamic efficiency (University of Bologna, Prof. Enzo Zanchini, 8 hours course).

7. Testing the stability of a fluid system (University of Bologna, Prof. Leonardo Santos de Brito Alves, 8 hours course).

8. Use of a symbolical mathematical code for convection-diffusion problems (University of Bologna, Prof. Leandro Alcoforado Sphaier, 8 hours course).

9. Control and Optimization methods (University of Bologna, Prof. Sandro Manservisi, 8 hours course).

10. X-ray physics and synchrotron radiation (University of Bologna, Prof. Federico Boscherini, 60 hours course).

11. Electronic measures and laboratory T-1 (University of Bologna, Prof. Pier Andrea Traverso, 90 hours course).

12. Fortran90 introduction(CINECA, BOLOGNA, Dot. Elda Rossi, 24 hours course).

13. Radiobiology of charged particles and radiotherapy implications (University of Bologna, Prof. Roberto Cherubini, 1 day course).

14. Liquid scintillators (University of Bologna, Prof. Ulrich Scherer, 1 day course).

15. Nuclear fuel management (University of Bologna, Prof. Jean Pierre Leveque, 1 day course).

Workshop:

1. Workshop on Accelerated High-Performance Computing in Computational Sciences (ICTP, International centre for theoretical physics, Trieste from 25/05/2015 to 05/06/2015)

Publications:

1. L. Sabbatucci, J.E. Fernandez: First principles Pulse Pile-Up balance equation and fast deterministic solution, submitted to Radiat. Phys. Chem. (2016)

2. L. Sabbatucci, F. Salvat: Theory and calculation of the atomic photoeffect Radiat. Phys. Chem. 121 (2016) 122-140

3. J. E. Fernndez, V. Scot, E. Di Giulio, L. Sabbatucci: Improvement of the detector resolution in X-ray spectrometry by using the maximum entropy method. Radiat. Phys. Chem. 116 (2015) 194-198.

4. J. E. Fernndez, V. Scot, L. Sabbatucci: A modeling tool for detector resolution and incomplete charge collection, X-ray Spectrom. 44 (2015)177-182.

5. L. Sabbatucci, V. Scot, J. E. Fernandez: Multi-shape pulse pile-up correction: the MCPPU code. Radiat. Phys. Chem. 104 (2014) 372375.

Presentations :

1. Improvement of the detector resolution in X-ray spectrometry by using the maximum entropy method: presented at IRRMA9 (9th International Topical Meeting on Industrial Radiation and Radioisotope Measurement Applications) in Valencia from 6 to 11 July 2014

2. Multi-shape pulse pile-up correction: the MCPPU code: presented by prof. J.E. Fernandez at ICDA-1 (1st International Conference on Dosimetry and its Applications) in Prague from 23 to 28 June 2013

Posters :

1 : A Modelling tool for detector resolution and incomplete charge collection: Poster presented at the EXRS-2014 (European Conference on X-Ray Spectrometry) in Bologna from 15 to 20 June 2014.

2 : First principles Pulse Pile-Up balance equation and fast deterministic solution: Poster presented by Prof. J.E. Fernandez at the ISRP-13 (13th International Symposium on Radiation Physics) in Pechino from 7 to 12 September 2015.

Acknowledgements

I would like to express my gratitude to Prof. J.E. Fernandez for the continuous support of my PhD study and related research, for his patience, motivation, and knowledge. Prof. Fernandez has supervised the works reported in the second chapter of this thesis. I am thankful to Prof. Fernandez for having introduced me in the field of radiation engineering and for having allowed me to participate in international conferences and to the Marco Polo project. I am thankful to Prof. Fernandez and to the Department of Industrial Engineering of Alma Mater Studiorum University of Bologna for financial support through the Marco Polo Grant programme. Thanks to Marco Polo project I have performed research activity at the University of Barcelona under the supervision of Prof. F. Salvat. The work done during my stay in Barcelona (supervised by Prof. Salvat) is reported in the first chapter of this thesis. I would like to express my gratitude to Prof. Salvat for his guidance which helped me in all the time of my stay in Barcelona. I am thankful to Prof. Salvat, to the Spanish Ministerio de Economía y Competitividad and ERDF (project no. FPA2013-44549-P) and to the Generalitat de Catalunya (grant 2014 SGR 846) for financial support in the last month of my stay in Barcelona. Thanks to Prof. Salvat I have done a full immersion in quantum-relativistic physics which opened to me new way of thinking and approaching reality. I also would like to thank Prof. Salvat for the Catalan culture classes, the philosophy of ”difficulties” instead of ”Problems” and for the ”Adeu-siau” greatly appreciated by the Catalan people. Last but not least I would like to express my immense gratitude to Ing. Viviana Scot, for her gargantuan knowledge and the indefatigable, patient and psychological support.

Bibliography

[1] L. Sabbatucci and F. Salvat. Theory and calculation of the atomic photoeffect. *Radiat. Phys. Chem.*, 121:122–140, 2016.

[2] L. Sabbatucci and J. E. Fernandez. First principles pulse pile-up balance equation and fast deterministic solution. *Submitted to Radiat. Phys. Chem.*, 2016.

[3] L. Sabbatucci, V. Scot, and J. E. Fernandez. Multi-shape pulse pile-up correction: the code mcppu. *Radiat. Phys. Chem.*, 104:372–375, 2014.

[4] J. E. Fernandez, V. Scot, and L. Sabbatucci. A modelling tool for detector resolution and incomplete charge collection. *X-Ray Spectrom.*, 44(3):177–182, 2015.

[5] J. E. Fernandez, V. Scot, E. Di Giulio, and L. Sabbatucci. Improvement of the detector resolution in x-ray spectrometry by using the maximum entropy method. *Radiat. Phys. Chem.*, 116:194–198, 2015.

[6] R. H. Pratt, A. Ron, and H. K. Tseng. Atomic photoelectric effect above 10 keV. *Rev. Mod. Phys.*, 45:273–325, 1973.

[7] J. H. Scofield. Theoretical photoionization cross sections from 1 to 1500 keV. Technical Report UCRL-51326, Lawrence Livermore Laboratory, Livermore, California, 1973.

[8] W. R. Johnson and C. D. Lin. Multichannel relativistic random-phase approximation for the photoionization of atoms. *Phys. Rev. A*, 20:964–977, 1979.

[9] T. N. Chang and U. Fano. Many-body theory of atomic transitions. *Phys. Rev. A*, 12:263–281, 1976.

[10] P. G. Burke and K. T. Taylor. R-matrix theory of photoionization. Application to neon and argon. *J. Phys. B: Atom. Mol. Phys.*, 8:2620–2639, 1975.

[11] A. Zangwill and P. Soven. Density-functional approach to local-field effects in finite systems: Photoabsorption in the rare gases. *Phys. Rev. A*, 21:1561–1572, 1980.

[12] F. A. Parpia and W. R. Johnson. Application of the time-dependent local density approximation to the photoionisation of mercury. *J. Phys. B: Atom. Mol. Phys.*, 16:L375–L379, 1983.

[13] D. Liberman and A. Zangwill. A relativistic program for optical response in atoms using a time-dependent local density approximation. *Comp. Phys. Commun.*, 32:75–82, 1984.

[14] D. E. Cullen, J. H. Hubbell, and L. Kissel. EPDL97 The Evaluated Data Library, ′97 Version. Technical Report UCRL-50400, Lawrence Livermore National Laboratory, Livermore, California, 1997.

[15] M. J. Berger, J. H. Hubbell, S. M. Seltzer, J. Chang, J. S. Coursey, R. Sukumar, and D. S. Zucker. XCOM: Photon Cross Sections Database. Technical report, Institute of Standards and Technology, Gaithersburg, MD, 2005. Available from `http://physics.nist.gov/PhysRefData/Xcom/Text/XCOM.html`.

[16] E. B. Saloman, J. H. Hubbell, and J. H. Scofield. X-ray attenuation cross sections for energies 100 eV to 100 keV and elements $Z = 1$ to $Z = 92$. *At. Data Nucl. Data Tables*, 38:1–197, 1988.

[17] P. A. Lee, P. H. Citrin, P. Eisenberger, and B. M. Kincaid. Extended x-ray absorption fine-structure - its strengths and limitations as a structural tool. *Rev. Mod. Phys.*, 53:769–806, 1981.

[18] R. H. Pratt. Atomic photoelectric effect at high energies. *Phys. Rev.*, 117:1017–1028, 1960.

[19] R. D. Schmickley and R. H. Pratt. X-, L-, and M-shell atomic photoeffect for screened-potential models. *Phys. Rev.*, 164:104–116, 1967.

[20] R. H. Pratt and H. K. Tseng. Behavior of electron wave functions near the atomic nucleus and normalization screening theory in the atomic photoeffect. *Phys. Rev. A*, 5:1063–1072, 1972.

[21] J. P. Desclaux. A multiconfiguration relativistic Dirac-Fock program. *Comput. Phys. Commun.*, 9:31–45, 1975.

[22] J. P. Desclaux. Erratum notice. *Comput. Phys. Commun.*, 13:71, 1977.

[23] O. Hemmers, R. Guillemin, and D. W. Lindle. Nondipole effects in soft x-ray photoemission. *Rad. Phys. Chem.*, 70:123–147, 2004.

[24] T. Fujikawa, R. Suzuki, H. Arai, H. Shinotsuka, and L. Kövér. Nondipole effects in photoemission angular distribution excited by high-energy x-rays. *J. Elect. Spect. Relat. Phenom.*, 159:14–23, 2007.

[25] L. Kövér. X-ray photoelectron spectroscopy using hard x-rays. *J. Elect. Spect. Relat. Phenom.*, 178–179:241–257, 2010.

[26] J. E. Fernández, J. H. Hubbell, A. L. Hanson, and L. V. Spencer. Polarization effects on multiple scattering gamma transport. *Radiat. Phys. Chem.*, 41:579–630, 1993.

[27] F. Salvat. PENELOPE-*2014: A code System for Monte Carlo Simulation of Electron and Photon Transport.* OECD/NEA Data Bank, NEA/NSC/DOC(2015)3, Issy-les-Moulineaux, France, 2015. Available from `http://www.nea.fr/lists/penelope.html`.

[28] M. B. Trzhaskovskaya, V.K. Nikulin, V. I. Nefedov, and V. G. Yarzhemsky. Nondipole second order parameters of the photoelectron angular distribution for elements $Z = 1$–100 in the photoelectron energy range 110 keV. *At. Data and Nucl. Data Tables*, 92:245–304, 2006.

[29] F. Sauter. Über den atomaren Photoeffekt in der K-Schale nach der relativistischen Wellenmechanik Diracs. *Ann. Phys.*, 11:454–488, 1931.

[30] M. B. Trzhaskovskaya, V. I. Nefedov, and V. G. Yarzhemsky. Photoelectron angular distribution parameters for elements $Z = 1$ to $Z = 54$ in the photoelectron energy range 100-5000 eV. *At. Data and Nucl. Data Tables*, 77:97–159, 2001.

[31] M. B. Trzhaskovskaya, V. I. Nefedov, and V. G. Yarzhemsky. Photoelectron angular distribution parameters for elements $Z = 55$ to $Z = 100$ in the photoelectron energy range 100-5000 eV. *At. Data and Nucl. Data Tables*, 82:257–311, 2002.

[32] J. W. Cooper. Multipole corrections to the angular distribution of photoelectrons at low energies. *Phys. Rev. A*, 42:6942–6945, 1990. Erratum, *Phys. Rev. A*, **45** (1992) 3362.

[33] J. W. Cooper. Photoelectron-angular-distribution parameters for rare-gas subshells. *Phys. Rev. A*, 47:1841–1851, 1993.

[34] A. Derevianko, O. Hemmers, S. Oblad, P. Glans, H. Wang, S. B. Whitfield, R. Wehlitz, I. A. Sellin, W. R. Johnson, and D. W. Lindle. Electric-octupole and pure-electric-quadrupole effects in soft-x-ray photoemission. *Phys. Rev. Lett.*, 84:2116–2119, 2000.

[35] M. Ya. Amusia, A. S. Baltenkov, L. V. Chernysheva, Z. Felfli, and A. Z. Msezane. Nondipole parameters in angular distributions of electrons in photoionization of noble-gas atoms. *Phys. Rev. A*, 63:052506, 2001.

[36] M. E. Rose. *Relativistic Electron Theory.* John Wiley and Sons, New York, 1961.

[37] I. P. Grant. Relativistic self-consistent fields. *Proc. Phys. Soc. A*, 86:523–527, 1965.

[38] M. E. Rose. *Elementary Theory of Angular Momentum.* Dover, New York, 1995.

[39] D. A. Varshalovich, A. N. Moskalev, and V. K. Khersonskii. *Quantum Theory of Angular Momentum.* World Scientific, Singapore, 1988.

[40] A. I. Akhiezer and V. B. Berestetskii. *Quantum Electrodynamics.* Interscience, New York, 1965.

[41] A. R. Edmonds. *Angular Momentum in Quantum Mechanics.* Princeton University Press, Princeton, NJ, 1960.

[42] I. P. Grant. Relativistic self-consistent fields. *Proc. Roy. Soc. A*, 262:555–576, 1961.

[43] D. A. Liberman, D. T. Cromer, and J. T. Waber. Self–Consistent–field Dirac wave functions for atoms and ions. I. Comparison with previous calculations. *Phys. Rev.*, 137:A27–A34, 1965.

[44] D. Liberman, D. T. Cromer, and J. T. Waber. Relativistic self-consistent field program for atoms and ions. *Comp. Phys. Commun.*, 2:107–113, 1971.

[45] B. Hahn, D. G. Ravenhall, and R. Hofstadter. High-energy electron scattering. *Phys. Rev.*, 101:1131–1142, 1956.

[46] J. C. Slater. A simplification of the Hartree-Fock method. *Phys. Rev.*, 81:385–390, 1951.

[47] R. Latter. Atomic energy levels for the Thomas–Fermi and Thomas–Fermi–Dirac potential. *Phys. Rev.*, 99:510–519, 1955.

[48] M. Born and E. Wolf. *Principles of Optics.* Cambridge University Press, Cambridge, 7th (expanded) edition, 2002.

[49] D. L. Falkoff and J. E. MacDonald. On the Stokes parameters for polarized radiation. *J. Opt. Soc. Am.*, 41:861–862, 1951.

[50] U. Fano. A Stokes-parameter technique for the treatment of polarization in quantum mechanics. *Phys. Rev.*, 93:121–123, 1954.

[51] U. Fano. Description of states in quantum meachanics by density matrix and operator techniques. *Rev. Mod. Phys.*, 29:74–93, 1957.

[52] W. H. McMaster. Polarization and the Stokes parameters. *A. J. Phys.*, 22:351–362, 1954.

[53] J. D. Bjorken and S. D. Drell. *Relativistic Quantum Mechanics.* McGraw Hill Book Co., New York, 1964.

[54] J. B. Mann and W. R. Johnson. Breit interaction in multielectron atoms. *Phys. Rev. A*, 4:41–51, 1971.

[55] J. H. Scofield. Radiative transitions. In B. Crasemann, editor, *Atomic Inner-Shell Ionization*, volume 1, Ionization and Transition Probabilities, pages 265–289. Academic Press, New York, 1975.

[56] J. H. Scofield. K- and L-shell ionization of atoms by relativistic electrons. *Phys. Rev. A*, 18:963–970, 1978.

[57] T. Watanabe. Measurement of the L absorption spectra of xenon. *Phys. Rev.*, 137:A1380–A1382, 1965.

[58] U. Fano and J. W. Cooper. Spectral distributions of atomic oscillator strengths. *Rev. Mod. Phys.*, 40:441–507, 1968.

[59] M. Gavrila. Relativistic K-shell photoeffect. *Phys. Rev.*, 113:514–526, 1959.

[60] J. H. Hubbell, H. A. Gimm, and I. Øverbø. Pair, triplet, and total cross sections (and mass attenuation coefficients) for 1 MeV–100 GeV photons in elements $Z =$ 1 to 100. *J. Phys. Chem. Ref. Data*, 9:1023–1147, 1980.

[61] J. J. Sakurai. *Advanced Quantum Mechanics.* Addison and Wesley, New York, 1967.

[62] F. K. Richtmyer, S. W Barnes, and E. Ramberg. The widths of the L-series lines and of the energy levels of Au(79). *Phys. Rev.*, 15:843–860, 1934.

[63] S. T. Perkins, D. E. Cullen, M. H. Chen, J. H. Hubbell, J. Rathkopf, and J. Scofield. Tables and graphs of atomic subshell and relaxation data derived from the LLNL evaluated atomic data library (EADL), Z = 1–100. Technical Report UCRL-ID-50400, Lawrence Livermore National Laboratory, Livermore, California, 1991.

[64] J. L. Campbell and T. Papp. Widths of the atomic K–N7 levels. *At. Data Nucl. Data Tables*, 77:1–56, 2001.

[65] F. Salvat and J. M. Fernández-Varea. Overview of physical interaction models for photon and electron transport used in Monte Carlo codes. *Metrologia*, 46:S112–S138, 2009.

[66] T. A. Carlson. *Photoelectron and Auger Spectroscopy.* Plenum Press, New York, 1975.

[67] G. P. Williams. Electron binding energies of the elements. In W. M. Haynes and D. R. Lide, editors, *CRC Handbook of Chemistry and Physics*, pages 221–226. CRC, Boca Raton, 91st edition, 2011.

[68] R. H. Pratt. Photoeffect from the L shell. *Phys. Rev.*, 119:1619–1626, 1960.

[69] J. H. Scofield. Angular and polarization correlations in photoionization and radiative recombination. *Phys. Rev. A*, 40:3054–3060, 1989.

[70] H. A. Bethe and E. E. Salpeter. *Quantum Mechanics of One- and Two-Electron Atoms.* Springer-Verlag, Berlin, 1957.

[71] D. Bote and F. Salvat. Calculations of inner-shell ionization by electron impact with the distorted-wave and plane-wave Born approximations. *Phys. Rev. A*, 77:042701, 2008.

[72] F. Salvat and D. Bote. Inelastic collisions of fast charged particles with atoms. Relativistic plane-wave Born approximation. Technical report, Universitat de Barcelona, Spain, 2011.

[73] F. Salvat, J. M. Fernández-Varea, and W. Williamson. Accurate numerical solution of the radial Schrödinger and Dirac wave equations. *Comput. Phys. Commun.*, 90:151–168, 1995.

[74] F. Salvat, D. Bote, and J. M. Fernández-Varea. RADIAL: a Fortran subroutine package for the solution of the radial Schrödinger and Dirac wave equations. *Comput. Phys. Commun.*, 2012. to be published.

[75] L. Büermann, B. Grosswendt, H.-M. Kramer, H.-J. Selbach, M. Gerlach, M. Hoffmann, and M. Krumrey. Measurement of the x-ray mass energy-absorption coefficient of air using 3 keV to 10 keV synchrotron radiation. *Phys. Med. Biol.*, 51:167–175, 2006.

[76] J. Knoll. *Radiation detection and measurement.* John Wiley and Sons,Inc., 2000.

[77] L. Wielopolski and R.P. Gardner. Prediction of the pulse-height spectral distortion caused by the peak pile-up effect. *Nucl. Instrum. Meth.*, 133:303, 1976.

[78] K. Taguchi, E. C. Frey, X. Wang, J. S. Iwanczyk, and W. C. Barber. An analytical model of the effects of pulse pileup on the energy spectrum recoded by energy resolved photn counting x-ray detectors. *Med. Phys.*, 37(8), 2010.

[79] Q. Bristow and R. G. Harrison. Theoretical and experimental investigations of the distortion in radiation spectra caused by pulse pileup. *Nucl. Geophys.*, 5 (1/2):141, 1991.

[80] S. L. Molodtsov and A. F. Gurbich. Simulation of pulse pile-up effect on the pulse-height spectrum. *Nucl. Instrum. Meth. in Phys. Res. B*, 267:3484–3487, 2009.

[81] S. Bochner and K. M. Chandrasekharan. *Fourier Transforms.* Princeton University Press, 1949.

[82] R. P. Gardner and S. H. Lee. Monte carlo simulation of pulse pile up. *JCPDS International centre for diffraction*, 1999.

[83] W. Guo, S.H. Lee, and R.P. Gardner. The monte carlo approach mcput for correcting pile-up distorted pulse-height spectra. *Nucl. Instrum. Meth. in Phys. Res. A*, 531:520–529, 2004.

[84] W. Guo, R.P. Gardner, and F. Li. A monte carlo code for simulation of pulse pile-up spectral distortion in pulse-height measurement. *Adv. X-Ray Anal.*, 48:246–252, 2005.

[85] P. C. Johns and M. J. Yaffe. Correction of pulse-height spectra for peak pileup effects using periodic and random pulse generators. *Nucl. Instrum. Meth. A*, 255:559, 1987.

[86] J. E. Fernandez and V. Scot. Simulation of the detector response function with the code mcshape. *Radiat. Phys. Chem.*, 78:882–887, 2009.

[87] G. W. Phillips and K. W. Marlowe. Automatic analysis of gamma-ray spectra from germanium detectors. *Nucl. Instrum. Meth.*, 137:525, 1976.

[88] J. L. Campbell, B. M. Millman, J. A. Maxwell, A. Perujo, and W. J. Teesdale. Analytic fitting of monoenergetic peaks from si (li) x-ray spectrometers. *Nucl. Instrum. Meth. Phys. Res. Sect. B*, 9:71, 1985.

[89] J. L. Campbell, L. McDonald, T. Hopman, and T. Papp. Simulations of si (li) x-ray detector response. *X-ray Spectrom.*, 30:230, 2001.

[90] T. Papp. On the response function of solid state detectors, based on energetic electron transport processes. *X-ray Spectrom.*, 32:458, 2003.

[91] F. Scholze and M. Procop. Modelling the response function of energy dispersive x-ray spectrometers with silicon detectors. *X-ray Spectrom.*, 38:312, 2009.

[92] M. Van Gysel, P. Lemberge, and P. Van Espen. Implementation of a spectrum fitting procedure using a robust peak model. *X-ray Spectrom.*, 32:434, 2003.

[93] M. Seltzer. Calculated response function of intrinsic germanium detectors to narrow beams of photons with energies up to 300 kev. *Nucl. Instrum. Meth. Phys. Res.*, 188:133–151, 1981.

[94] U. Fano. Ionization yield of radiations. ii. the fluctuations of the number of ions. *Phys. Rev.*, 72:26, 1947.

[95] R. Devanathan, L. R. Correls, F. Gao, and W. J. Weber. Signal variance in gamma-ray detectors?a review. *Nucl. Instrum. Meth. A*, 565:637, 2006.

[96] A. Owens. Semiconductor materials and radiation detection. *J. Synchrotron Radiat.*, 13:143, 2006.

[97] T. Papp, M. C. Lepy, J. Plagnard, G. Kalinka, and E. Papp-Szabo. A new approach to the determination of the fano factor for semiconductor detectors. *X-ray Spectrom*, 34:106, 2005.

[98] K. J. McCarthy A. Owens, G. W. Fraser. On the experimental determination of the fano factor in si at soft x-ray wavelengths. *Nucl. Instrum. Methods Phys. Res. Sect. A*, 491:437, 2002.

[99] R. H. Redus, J. A. Pantazis, T. J. Pantazis, A. C. Huber, and B. J. Cross. Characterization of cdte detectors for quantitative x-ray spectroscopy. *IEEE Trans. Nucl. Sci.*, 56(4):2524, 2009.

[100] M. Matzke. Unfolding procedures. *Nucl. Instrum. Meth. Phys. Res. A*, 2002.

[101] Hussein E. M. A. *Computed Radiation Imaging: Physics and Mathematics of forward and Inverse Problem.* Elsevier, Amsterdam, 2011.

[102] T. Inouye, T. Harper, and N. C. Rasmussen. Application of fourier transforms to the analysis of spectral data. *Nucl. Instrum. Meth.*, 67:125–132, 1969.

[103] W. Wätzig and W. Westmeier. Determination of the average fwhm in background free spectra. *Nucl. Instrum. Meth.*, 159:547–551, 1979.

[104] M. Matzke. Unfolding of pulse height spectra: The hepro program system. *ReportPTB-N-19*, 1994.

[105] M. Reginatto and P. Godhagen. Maxed a computer code for maximum entropy deconvolution of multi sphere neutron spectrometer data. *Health Phys.*, 1999.

[106] M. Reginatto. The multi channel unfolding programs in the umg package mxd mc33 grv mc33 and iqu mc33 and umg package version 3.3. *Physikalisch Technische Bundesanstalt(PTB)*, 2003.

[107] J. E. Fernandez, V. Scot, and E. Di Giulio. Spectrum unfolding in x ray spectrometry using the maximum entropy method. *Radiat. Phys. Chem.*, 95:154–157, 2014.